POWDER BED FUSION – LASER BEAM OF TI-6AL-4V LATTICE STRUCTURES FOR BIOMEDICAL APPLICATIONS

by

XUE CAO

A thesis submitted to the
University of Birmingham
for the degree of
DOCTOR OF PHILOSOPHY

School of Chemical Engineering
College of Engineering and Physical Sciences
The University of Birmingham

September 2024

Abstract

Powder bed fusion – laser beam (PBF-LB) as a technology of additive manufacturing, has provided great potential for the fabrication of porous lattice structures applied in orthopaedic devices to achieve anatomic and customised functions. However, the mechanical properties and surface characterisation involved in the osseointegration process remain challenges, causing patients risk in revision surgeries. The physiochemical properties of implants are governed by various behaviour of lattice structures and is subject to the nature of PBF-LB. To address this, the PBF-LB process need to be optimised to ensure the fabrication quality and stability of lattice structures. Fundamental understanding of lattice structures is required to satisfy wider designable possibility and improvement of mechanical and biological behaviours of skeletal devices.

First, the processing window and scanning strategy of manufacturing lattice structures with ultrafine struts thickness below 350 μm was investigated. Compared to the contour plus hatching scanning strategy, a single contour strategy was developed and optimized to ensure a more homogenous energy input for improving the geometric accuracy and internal defects reduction in lattice structures.

Secondly, performances of lattice struts with varying built angles and process parameters were studied. Both the mechanical and *in-vitro* biological response demonstrated the distinct impact of lattice struts angle. Results showed that under the optimised processing parameters, internal porosity can be reduced to 99.8% regardless of the geometric differences.

Considering wider feasibility of contour strategy for lattice manufacturing, multi-contour was explored to accommodate the PBF-LB fabrication of lattice structures composed with various geometries and dimensions design. Surface roughness, compressive test, and microstructures were conducted, illustrating that the ductility, surface condition and geometric accuracy and can be improved via multi-contour strategy.

At last, to further verify the potential of PBF-LB lattice structures via tailoring the struts angle, rotation strategy study was conducted and evaluated through compressive, high-cycle fatigue, and mammalian cell test. The specimen with both struts angle and unit cell orientated presents an improved fatigue strength and biological response. Overall, this thesis contributes to the development of PBF-LB lattice structures applied for biomedical implants.

ACKNOWLEDGEMENTS

First and foremost, I would like to express my deepest gratitude to my supervisors, Dr. Sophie Cox, Dr. Luke Carter and Prof. Moataz Attallah, for their invaluable guidance, continuous support, and patience throughout my Ph.D. journey. Dr. Sophie Cox has cultivated me in aspects covering not only for academic achievements but also life guidance. Dr. Luke Carter has provided me with the most precious knowledge and experience he has in this cutting-edge field. Their insightful feedback and constructive criticism have been instrumental in shaping this thesis. Without their encouragement and advice, this work would not have been possible.

I am sincerely thankful to my colleagues and friends across the University of Birmingham, who have provided me immense and expertise support and help to assist me accomplishing the PhD. Acknowledgements to: Dr. Victor Villapun for wide support and patience in both mammalian cell work and MATLAB programming; Dr. Kenny Man for genuine assistance in mammalian cell work; Dr. Sophie Louth for kind help in nTopology; Lucie Giangiorgi for support in programming; Yulong Wang for sharing experience in finite element simulation; Dr. Alexander Evans and Daisy Rabbitt for their precious time and knowledge in residual stress testing; Dr. Ludwig Schneider and Thomas Collins for help in electron microscope work; great thanks to Daniel Wilmot for expertise training and keeping the lab running. I have cherished every moment of our discussions, and their support has been invaluable in keeping me motivated throughout this journey.

Also, special thanks to the help and support my friends: Hebin Jiang and Haixia Yin for their competent assistance in mechanical testing; Dr. Kun Sun and Dina Fouad for expertise operation in EBSD; Ao Tong for training on coding.

I would like to extend my heartfelt gratitude to my parents, whose unwavering support in both financially and mentally, love, and encouragement have been my constant source of strength throughout this journey. Their belief in me, even during the most challenging times, has provided me with the confidence and motivation to persevere. I am forever grateful for the sacrifices they have made to help me achieve my dreams. This accomplishment is as much theirs as it is mine.

At the end, I would like to say great thanks to my partner Bohong Wang, who has been the source of strength, confidence, and positive energy. I am truly grateful for everything Bohong has done to help me reach this milestone – thank you for your accompany, caring, happiness and the most tasty food whenever I needed.

CONTENTS

LIST OF FIGURES

LIST OF TABLES

LIST OF ACRONYMS AND ABBREVIATIONS

AM additive manufacturing

ALP alkaline phosphate

AMPM additive manufacturing process monitoring

BCC body-centred cubic

CAD computer-aided design

CIS crack initiation site

EBSD electron-backscatter diffraction

ED energy density

FCC face-centred cubic

FEA finite element analysis

HCF high cycle fatigue

HCP hexagonal close-packed

HIP hot isostatic pressure

LED laser energy density

LoF lack of fusion

MC multi-contour

CT micro-computed tomography

MFS maximum flexural strength

MPR melting pool response

MRI magnetic resonance imaging

NIR national joint registry

P laser power

PBF-LB powder bed fusion – laser beam

PBS phosphate buffered saline

PEO plasma electrolytic oxidation

R_a average roughness

Ti64 Ti-6Al-4V

SC single contour

SC + F single contour + filling

SEM scanning electron microscopy

SO strut orientation/angle

SOUO strut orientation/angle and unit cell orientation

TPMS triply periodic minimal surface

UFS ultimate flexural strength

UO unit cell orientation

v scanning speed

VED volumetric energy density

Chapter 1 INTRODUCTION

This chapter introduces the background of Powder Bed Fusion – Laser Beam (PBF-LB), specifically applied for the manufacturing of Ti-6Al-4V (Ti64) lattice structures. Aligning the application in orthopaedic devices, the importance and challenge of PBF-LB lattice structures will be briefly highlighted in the aspect of process and design. Bringing questions, aims and objectives were listed to summarise main focus of this work. At the end, an overview of the thesis structure is introduced.

1.1 PBF-LB lattice structures for biomedical implants

The world is experiencing an increase in both number and proportion of older people aged 60 and over in the population, where the aging population is expected to reach 2.1 billion by 2050 [1]. This highlights the importance of healthcare development, especially the growing demanding of biomedical implants to tackle the health conditions associated with older people. As national joint registry (NIR) reported, the hip replacement surgery has exceeded 1 million cases in the UK by 2023 due to osteoarthritis, where the median age of patients is 69 years [2]. Considering long-term and load-bearing requirements, aseptic loosening takes account into 32,616 (33%), which is the majority among the reasons for knee-revision surgery [2]. Main factor attributing to the aseptic loosening is the mismatch of mechanical properties between implants and host bone. The stress-

shielding effect of the metal biomedical products would lead to bone resorption and failure of implantation for patients as illustrated in fig. 1.1. Implant loosening is a symptom of implant failure attributing to implant movement or migration in the bone. Loosening of the stem accounts for 79% of the revision surgery, which is due to the stress-shielding caused bone loss [3]. Given the risk of revision operation can be extremely high considering its complications elderly patients have, such as cardiac issue, pulmonary, and mortality, possibility of revision should be minimised.

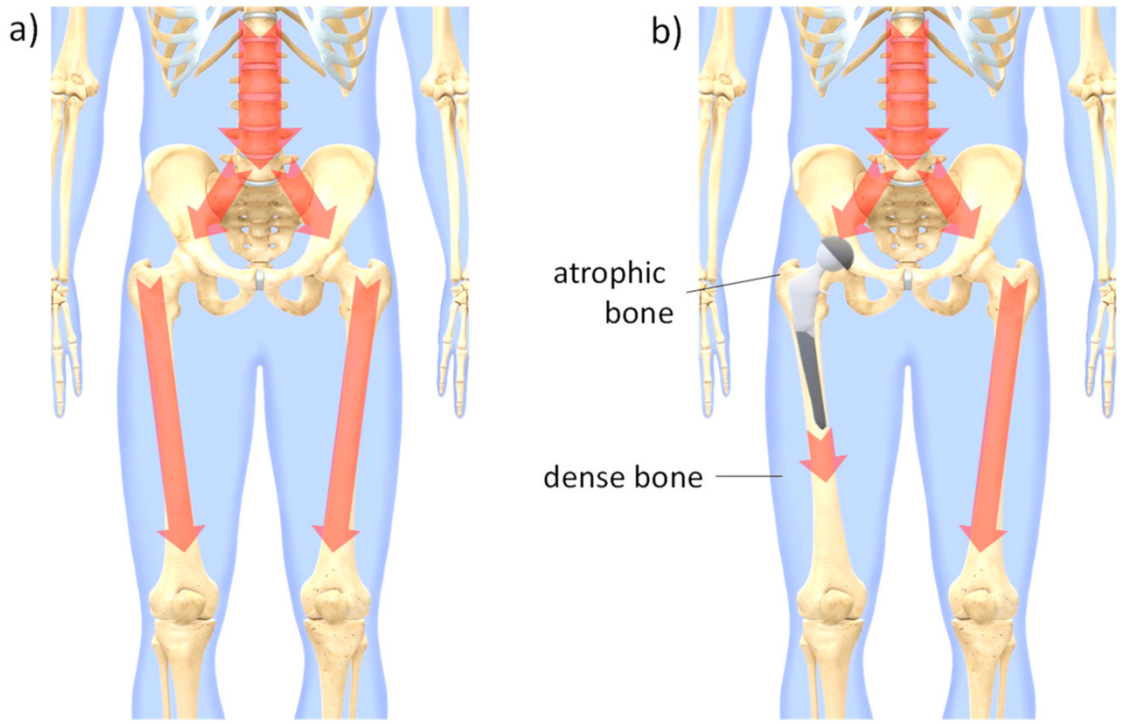

Figure 1.1 (a) Normal physiological distribution of the load; (b) load re-distribution due to implanted hip replacement. Adapted from figure produced for Savio et al, Processes, 2022.

Lattice structures consisted of connecting thin wall or struts can facilitate the bone in-growth to improve the osseointegration. The diversity and variability of lattices lead to different permeability and mechanical properties relating to osseointegration between metal implants and bone. For example, after years of innovation and development,

intelligent spinal fusion cage implant has been developed and integrated with lattice structures to monitor the bone healing process [4].

Benefitting from the impressive mechanical strength, corrosion resistance, and biocompatibility; titanium and its alloys, especially Ti64 has been applied for biomedical, aerospace, energy and electronic fields. For the biomedical use, Ti64 and other titanium-based implants perform better bonding with the bone than other metallic implants for their less likely encapsulation by a fibrous tissue. Biological processes generate hydrogen peroxide, which interacts with the surface oxide leading to the formation of titanium-peroxy gel on the implant surface. This would be possibly explain the bioactivity of titanium [5].

Novel biomedical bone implants integrated with lattice structures, also known as meta-biomaterials, which are topologically ordered with repeating micro-scale unit cells to achieve targeted functions at the macro-scale [6]. Ti64 meta-biomaterials is enabled by the additive manufacturing (AM) provide comparable mechanical properties to that of human bone due to their suitable stiffness. In PBF-LB technology, belonging to AM, powders will be melted and fused together via laser beam energy. It achieves complexity-free of part geometry via a layer-by-layer depositing process. In regardless of numbers of advantages of PBF-LB, some aspects relating with lattices in biomedical application need to be further considered:

- Defects including internal porosity and balling that affect mechanical properties and fatigue performance.

- As-fabricated surface roughness relating with biological response and fatigue performance of lattices.
- Microstructure inherited by the rapid heating and cooling process of PBF-LB influences mechanical properties.
- Residual stress remained in lattices potentially impacting the fatigue life as load-bearing application .

PBF-LB process parameters have significant effect on the products. Laser power and scanning speed have been widely studied to optimise the quality of Ti64 products. However, their effect on lattices with much finer structures and changing geometry can vary significantly compared to the solid bulk materials due to different heat transfer, which requires to seek and address the challenges of PBF-LB brings to the lattice structures.

Different types of lattice structures including regular, irregular, stochastic and non-stochastic structures have been developed and focused on their effects on mechanical performances as biomedical implants. It has been shown that the mechanical strength is strongly related to the relative density of the lattices, the elastic modulus of which can varies with the topological design despite the same porosity level. Given the mechanical properties of lattices depend on their representative unit cells, tailoring and optimising the microstructural design of lattices can achieve turnability of the fatigue and quasi-static mechanical performances, even surface area, mass transport and other features satisfying the application requirements and performance needs [7].

Despite the advantages of the additively manufactured lattice structures provide, numerous challenges involving the manufacturing process, the topology design and the integration of the implants, remain to engineers, clinicians and AM users to tackle. Firstly, compared to solid parts, porous lattices are more prone to experience fatigue failure, influencing the lifetime and increasing risk of re-surgery for patients. However, there are limited studies on the fatigue performances on lattice structures for biomedical application. Secondly, there is a compromise between the stiffness (and/or strength) and the designed porosity, indicating the importance to balance the osseointegration and pore size. Additionally, the predictive model is needed to save the costs and improve the efficiency of fabricating the lattices and lattice-associated products, while the predictability of the related properties is limited by the intricate process parameters of PBF-LB complexed with the various geometries of lattices. Moreover, it is necessary to optimise the design of lattices to satisfy multi-purpose of biomedical applications.

1.2 Aims and thesis structure

PBF-LB processed Ti64 lattice structures are studied to enhance understandings for further improvement biomedical devices. The aim of this thesis is to improve the predictability of PBF-LB manufactured lattices via optimising the process as well as tailoring structure design. Both the mechanical and biological performances are examined to establish feasible ways to achieve customisation of orthopaedic implants. To further apply and evaluate the effect of structural differences, rotation strategies were proposed, which showcasing an increasing in both mechanical and biological response.

Chapter 2 reviewed the literatures firstly on the bone structure and properties to understand the fundamental and clinical requirements of biomedical devices. Metal lattice structures were then introduced and discussed to highlight the effects of topological design, distinctive mechanical performances, and the limitation of current studies on the fundamental side. Following lattices, PBF-LB and the effects of the process on lattice structures was presented, in terms of how the PBF-LB parameters associate with the lattices quality and why it is important. The effects linking with the manufacturing accuracy, manufacturability, defects (undesired pores), microstructure, residual stress, mechanical properties, fatigue and biological response were covered, to provide a relative full scope for the current gaps existed.

With the aim to improve the predictability of PBF-LB for manufacturing lattices, a processing window was developed, and single contour (SC) scanning strategy was proposed and assessed in **Chapter 3**. The manufacturing accuracy of lattice structures was lowered to 0.1% for the optimised PBF-LB parameters, as well as showing the manufacturability of manufacturing lattice with struts thickness of 150 m through applying SC.

On the other hand, considering the complex and variety of lattice geometries is basically the changing of the struts angle and the way of their distribution, the **Chapter 4** aims to address the challenges from focusing on the effects of struts angle and the process parameters in either individual or combined manner. Moreover, a novel image analysis tool was proposed to examine the whole-profile roughness of struts. Three-point bending

test and *in vitro* assessment were conducted to explore the effects of geometry and PBF-LB parameters. Finally, a map was developed to assist the selection of lattice structures.

Based on the map developed as aforementioned, multi-contour (MC) scanning strategy was studied in **Chapter 5** to accommodate the fabrication of irregular, various and changing geometry of lattices. Surface quality, geometrical accuracy, compressive properties and microstructure were compared between the MC and single contour with filling (SC+F) strategy.

Moreover, to further explore the potential while altering the rotation of lattices according to the lattice design map developed in **Chapter 4**, lattices with three different rotation strategies were explored in **Chapter 6**. Compression, fatigue, and biological response were evaluated to illustrate the influence of rotation strategy on lattice physiochemical properties. This showcases the potential of simply tailoring the lattice structures through rotation for application of biomedical devices.

At the end, the conclusions of this work were illustrated in **Chapter 7**. Future work was also described regarding to the limitation of this thesis, including residual stress, microstructure, and *in vivo* biological work.

Chapter 2 LITERATURE REVIEW

2.1 Introduction

Bones have a diverse range of functions including mechanical, biological, and chemical, providing structural support and movement, organ protection, mineral storage and release [8]. At the macro-scale (Fig. 2.1 (a)), bone tissue can be distinguished into cortical bone with a dense and low porosity of 5 - 15%, and cancellous bone, also known as sponge or trabecular bone, which consists of trabecula with a porosity of 40 - 95% [9]. Load-bearing capability also relies on the cortical bone, withstanding significant mechanical stress and weight as a crucial part for long bones of limbs, such as the femur and tibia. Cortical bone is important for mineral storage, particularly calcium and phosphorus, whilst the cancellous bone is composed of trabecular struts and porous space that is filled with bone marrow [10]. Cancellous bone found throughout the body, including in the ends of long bones, the interior of vertebrae, as well as that of short and flat bones. It houses red marrow that is responsible for blood cell production. The structure of cancellous bone reduces the overall weight while maintaining strength and support. With a light-weight structure as shown in fig. 2.1 (b), porous cancellous bone distributes the stress more efficiently to avoid direct mechanical impact to cortical bone [11].

Mechanical behaviours of natural hydrated bone follows a regular load-deformation mode to that of metals (Fig. 2.1 (c)) [11]. There is an elastic region, where the stress rises linearly with the increasing deformation before reaching the yield point. Then the curve plateau is at a high stress level until final fracture. Once the fracture occurs, osteoblasts will be released through periosteum to generate new bone after the inflammation stage.

Then it remodels the bone to grow hard tissue at the fracture gap [12]. To promote the bone healing, orthopaedic implantation is applied to restore the anatomical function of injured bone [13].

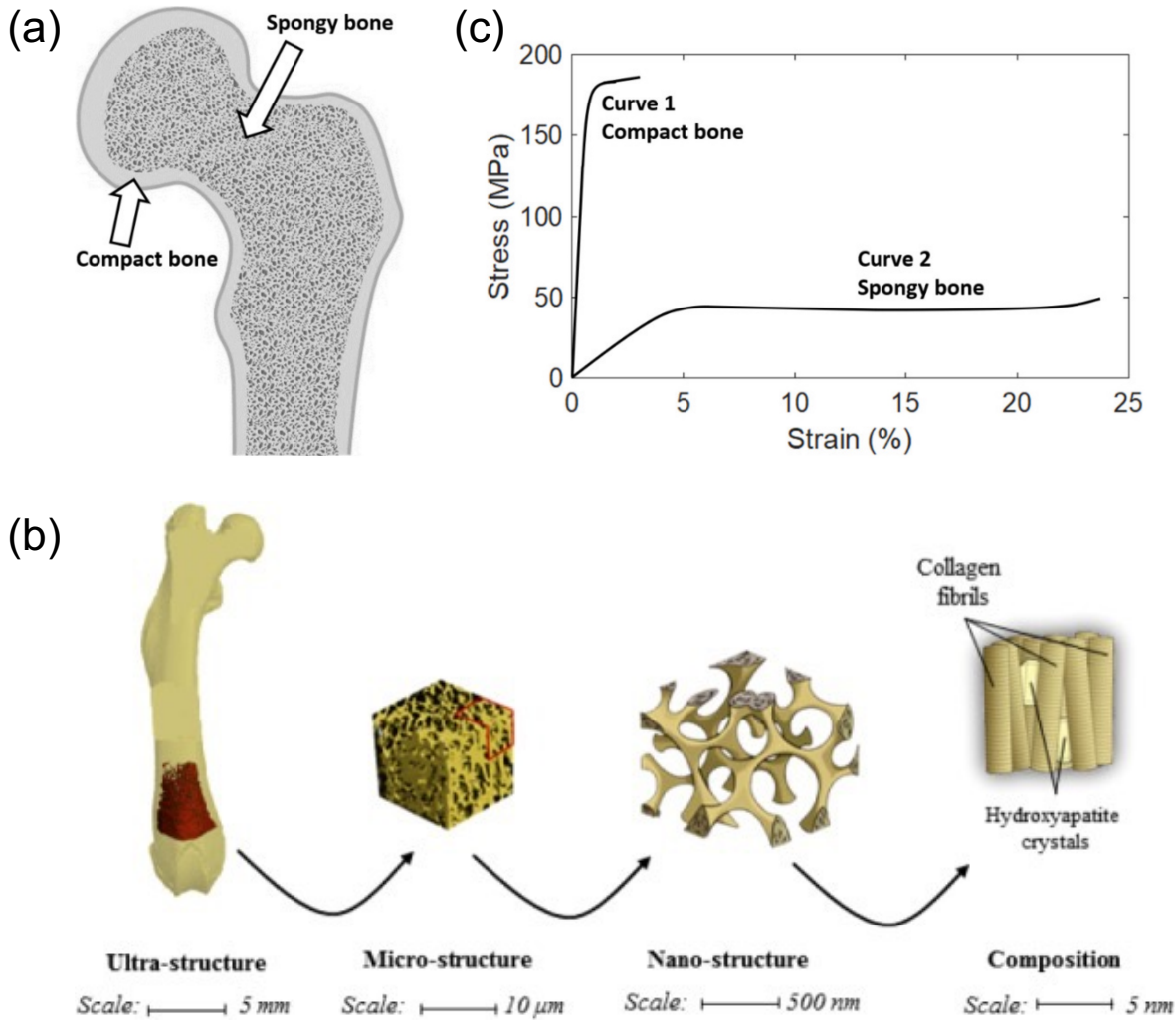

Figure 2.1 (a) Two different bone tissue includes dense compact bone and porous spongy-like cancellous bone; (b) trabecular bone scale from macro to nano; (c) stress-strain curve of compact bone and cancellous bone. Adapted from figure produced for Murat, Nova Science: Hauppauge, 2012, and Oftadeh et al, Journal of Biomechanical Engineering, 2015.

One of the highest risks for orthopaedic implants is the stress-shielding effect, inducing implantation failure caused by bone loss that leads to instability [14]. Stress shielding occurs when the stiffness of implants is higher than the native bone, since this limits

mechanical stimulation of the surrounding tissue leading to a reduction in density (Fig. 2.2) [15]. Maintaining shape and density of normal and healthy bones is a dynamic remodelling process according to the Wolff's law, indicating the normal bone remodelling is evaluated by the ratio of osteoclasts to osteoblasts [16]. It reflects the healthy behaviour of bone cells to sense mechanical loading and to continuously repair micro-fractures. Skeletal devices generated from material largely stiffer than the local bone tend to sustain the load and even the patients' weight, resulting in an uneven redistribution of force transmission, and blocking the surrounding bone from the mechanical stimulus for remodelling. This would lead the host skeleton to resorb and reduce the mass and density of the affected bone, potentially leading to implant loosening and/or failure [17-19]. Revision surgery due to the resorptive process of stress shielding has become a common challenge in hip [20], knee [21, 22], shoulder [23], spine [24], and craniofacial implants [25]. In 9% of patients a significant reduction in cortical thickness was detected due to stress shielding for an averaged 5.3 years' follow-up radiograph [23]. Although the timeframe leading to the clinical failure due to bone resorption has not been determined, considering the long-term stability and future revision, the impact of bone loss should not be underestimated. The significant bone loss near the metal implants could be a severe problem in later years, which is even more relevant to younger and more active patients, for whom the preservation of bone storage is as important as restoring function [21].

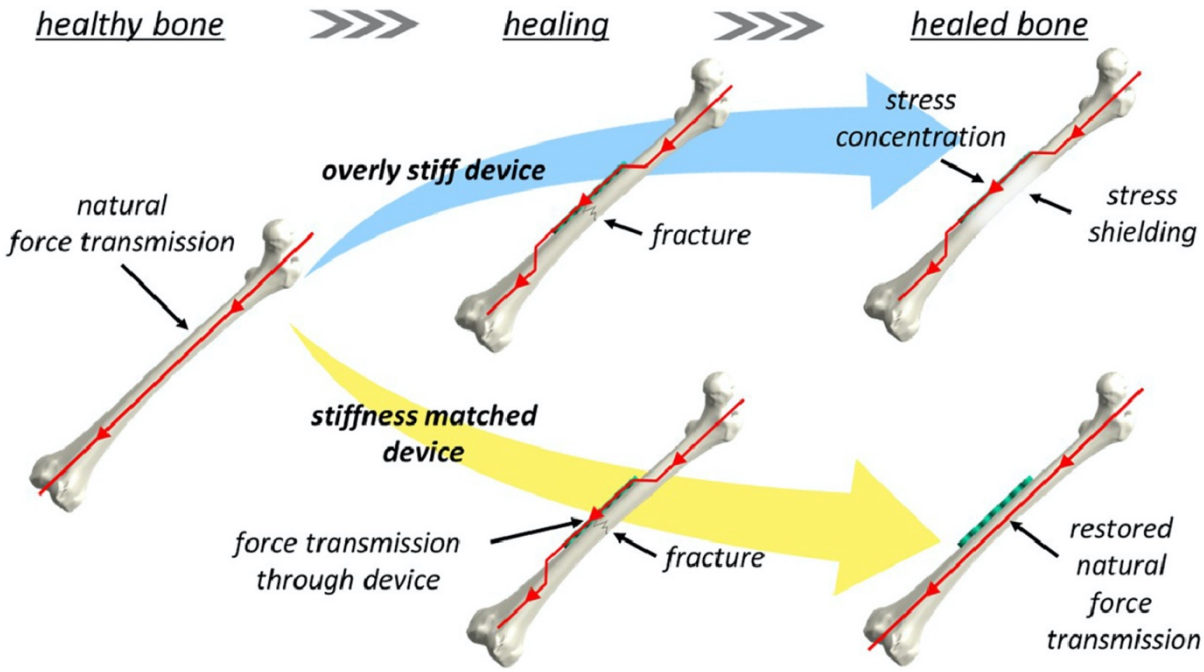

Figure 2.2 Stress-shielding effect and bone healing under force transmission for an overly stiff device and one with matched mechanical stiffness. Adapted from figure produced for Chmielewska et al, Acta Biomaterialia, 2024.

In 2022, the global orthopaedic devices market was valued at USD 50.4 billion, and is anticipated to register a compound annual growth rate of 4.2% from 2024, until 2030 reaching a value of USD 78.71 billion [26]. As the global population ages and traumatic injuries increase more than 20 million people globally undergo orthopaedic procedures [27]. There are a number of metallic biomaterials used in these surgeries to restore or replace diseased or damaged bones. Metallic biomaterials are a good choice for these devices since they generally exhibit mechanical properties beyond bone tissue, corrosion resistance and biocompatibility. In the early 1950s, Branemark observed the attachment of human bone cells to titanium-based teeth prostheses implanted in the jaw, leading to the definition of osseointegration [28]. 316L stainless steel is also another widely used biomaterial due to its low cost and high elastic modulus for stable fixation. However, it is less widely used compared with Ti-based and cobalt chromium alloys since it is

incompatibility with magnetic resonance imaging and highly infective [29]. In terms of the non-metallic materials, hydroxyapatite and bioglass 45S5 as bioceramics are the most commonly applied for skeletal implants. Despite exhibiting osseointegration, the inherent brittleness of bioglass 45S5 has limited application to low load bearing applications [30, 31]. Polyetheretherketone has gained attention and has been used in skeletal devices for its antiallergic, elastic modulus comparable to bone, and aesthetic attributes, however, polyetheretherketone is high cost, low surface energy causing less cell adhesion, and difficult to manufacture [32].

Titanium (Ti)-based alloys compared to the aforementioned biomaterials possess improved yield strength, and the main categories of which exhibit the required biocompatibility and corrosion. These made Ti-alloys a pioneer especially for dental application, and an attractive biomaterial for skeletal implants [33, 34]. Ti64 composited of + phase, and commercially pure titanium take over more than 95% of all titanium-based alloys for biomedical devices [35]. Especially Ti64 (compressive yield strength of 860 MPa, elastic modulus of 114 GPa) due to its good fabricability and high yield strength for load-bearing implants. Meanwhile, considering both avoiding short-term infection and/or rejection and long-term biocompatibility, development of alloys without toxic elements is ongoing [36].

While there is the pursuit of new titanium alloy compositions to address some current drawbacks, activities are emerging remarkably to advance skeletal device performance through new geometries to tackle the stress-shielding effect. Especially considering the long-term clinical success of implants requiring matched elastic modulus, compressive

and fatigue strength, metallic porous structures could provide proper mechanical properties and osseointegration. As the demanding of fabricating highly complex porous structures with desired quality is gradually increasing, additive manufacturing (AM) has been developed. AM allows to customise metallic, ceramic and polymer components without molds or tools of subtractive process like milling and turning, as well as more geometric freedom and material flexibility to enable more creativity and novel products [37]. Powder bed fusion-laser beam process that can build solid structural parts with nearly no geometric limits. Multiple functions, including mechanical, biological, electric, acoustic, thermal and magnetic may be tailored through PBF-LB metamaterials, is also known as lattice structures [38]. These properties can be adjusted and enhanced via parametric control of PBF-LB and topological design of lattices, finding utilisation in biomedical, aerospace and other engineering areas [33]. This literature review focuses on the use of lattices produced via PBF-LB for use in biomedical engineering, including bone replacement, arthroplasty, craniofacial, maxillofacial and dental devices, as well as surgical instruments [39]. To establish a close relationship for the PBF-LB parameters, topology and properties, this chapter will cover the review of bone, lattice structures, and PBF-LB process to give a comprehensive understanding of applying lattice structures for biomedical applications.

2.2 PBF-LB process

As presented in fig. 2.3 , PBF-LB process involves a layer of metallic powder (20-60 μm thickness) distributed on the substrate by a recoater blade [40]. After the powder is deposited on the building substrate, the laser source is directed on the powder bed, and selectively melts the powder according to the geometry of computer-aided design (CAD)

to generate a liquid pool, known as melting pool, which then solidifies and cools down rapidly. After completing one layer, the platform is lowered by the pre-defined layer thickness and a new layer of powder is spread, fused, consolidated and lowered repeatably until the whole part finishes [41]. An inert argon atmosphere is needed for the process to avoid high reactivity of the alloy.

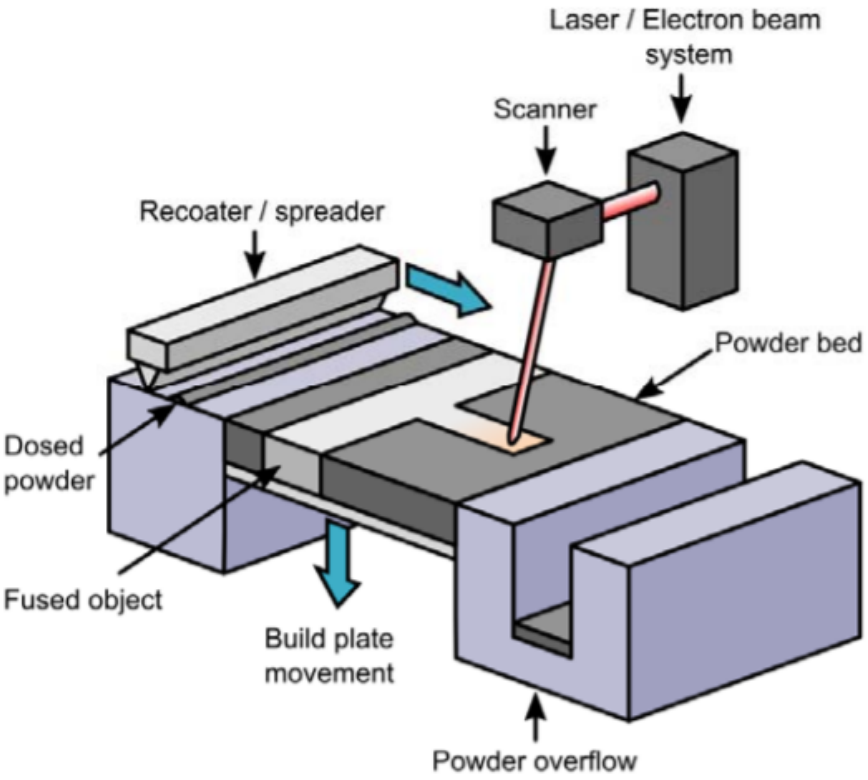

Figure 2.3 Schematic illustrating the principle of PBF and fundamental elements of the build chamber. Powder is dosed at the back of chamber and distributed to the substrate by a recoater. Laser/electron beam then move and interact with the powder bed to melt and fuse the material according to the design. After one layer finished, the plate moves down regarding to the set-up layer. Adapted from figure produced for Lowther et al, Additive Manufacturing, 2019.

Despite the advantages of PBF-LB offered, numerous disadvantages including microstructural and defects, such as internal porosity and geometric inaccuracy, inherited from the manufacturing process are commonly seen in PBF-LB products, affecting the mechanical performance relating with biomedical implants. Given the intricate geometric

features of lattices differentiate, these inherent processing difficulties tend to be amplified compared to bulk components with larger heat affected zone.

2.3 Lattice structures

To mimic the human bone structure and achieve anatomical function, porous devices are a growing area within orthopaedic implantology [33]. A typical lattice structure is consisted of spatially arranged unit cells connected by struts and nodes. Gibson defined porous structures as interconnected networks composed of struts or plates [42]. However, although lattice structures have been developed for more than 40 years, there is no unified definition of them. Through adjusting the porosity and relative density, lattices can be fabricated to an appropriate level to accommodate the human bone requirements in both the mechanical properties and tissue adhesion. As shown in fig. 2.4, there are basically three ways to classify the lattice structures according to mechanical response, morphology, and geometrical distribution. Pan et al. categorised lattice structures into uniform and non-uniform types [43]. Uniform lattice structures are consisted of repeating unit cells with consistent geometrical features, while non-uniform structures are arranged with unit cells in changing geometries or topologies. Whilst lattices can also be divided into strut-based and triply periodic minimal surface (TPMS)-based regarding to a broader range of unit cells. For strut-based lattices, they can be further classified based on the mechanical properties governed by the topology, i.e. stretching- and bending-dominated structures [44].

As Zadpoor defined, in terms of the continuous solid materials, the mechanical properties represent the intrinsic materials, while the mechanical properties in lattices would

converge to specific values when the number of unit cells reached a high level, representing the apparent macroscopic properties of structures [6]. This is important for exploring and comparing the governing factors of lattices mechanical properties, which is different to that of traditional bulk materials. Lattices structures can be tailored to achieve improved or novel mechanical characteristics, including auxetic geometries with negative Poisson's ratio [45], negative stiffness [46], negative compressibility [47], negative thermal expansion coefficient [48], or higher stiffness to mass ratios [49], while these exceptional functions may be limited when using traditional bulk materials [50].

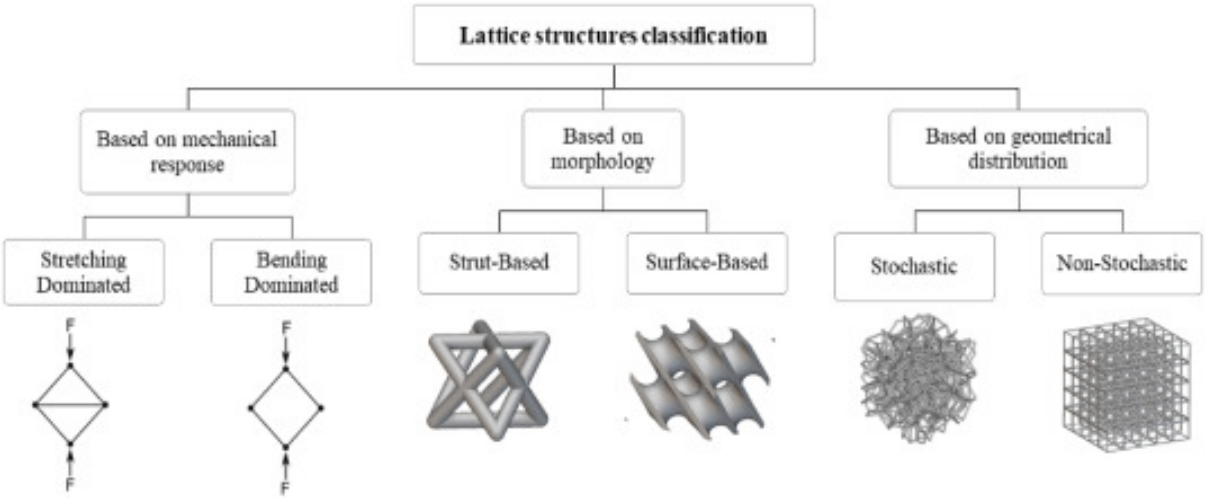

Figure 2.4 Categories of lattice structures according to mechanical response, morphology, and geometrical distribution. Adapted from figure produced for Tyagi et al, Bioprinting, 2023.

Regarding the load-bearing requirement and proper functioning, mechanical properties for lattices as meta-biomaterials are primarily paid attention to. Both the design topology and the relative density (defined as the ratio of the apparent density of lattices and the density of the parent materials) influence lattice mechanical properties [51]. In addition, factors of lattice design, including the strut size, surface condition, orientation and pore size are essential to bone in-growth. The most common and primary strut-based lattices

investigated are body-centred cubic (BCC) [52-56], face-centred cubic (FCC) [57-59], diamond [56, 60], simple cubic [57], and octahedron [61], and variation of these, such as BCCZ and FCCZ with vertical z-struts connected. Shivakumar et al. reviewed the mechanical properties of strut-based lattices, and concluded that the Ti64 lattices designed with BCC should be the first choice for its higher yield strength of 435 MPa with a relative density of 67%, followed by FCC, diamond and simple cubic [62]. Zhang et al. fabricated Ti64 diamond lattices via PBF-LB, found that increasing the strut thickness from 200 to 400 μm increased the ultimate compressive strength from 36.45 MPa to 140.26 MPa, as well as the elastic modulus from 1.21 GPa to 5.15 GPa [63]. Further results in vivo test in Beagle dogs show that the damaged load-bearing bones implanted with lattice of 66.1% porosity were well reconstructed for an osteonecrosis model, of which the size is . While Deng et al. studied the pore shape effect on bone regeneration keeping the porosity consistent [64]. Their results demonstrated that the scaffold of diamond unit cell performs the optimal bone growth compared to the other three topological lattices of Circular cubic, single cubic, and Tetrakaidecahedron cubic. To simulate the fluid condition in the body, they conducted computational fluid dynamics, illustrating that the trajectory of fluid flow inside the diamond lattice is the longest, which could promote blood vessel growth, nutrition transport and bone regeneration. Research by Wang et al. demonstrated the proliferation of macrophages and osteogenic gene-related expression of bone marrow mesenchymal stem cells was maximised with a pore size of 600 m [65]. This was ascribed to the balance of the elastic modulus, strength, contact angle, and capability of nutrient transfer that synergistically facilitate the proliferation of macrophages when the lattice fabricated with 600 μm pore size. Furthermore, Chen et al. revealed that the contact angle decreases as the pore size

increases, attributing to the surface characterisation associated with different pore sizes of lattices ranging from 500 to 700 μm [66]. They suggested scaffolds with pore size of 500 μm and 60% porosity are the optimal according to the biological response including cell proliferation, osteogenic differentiation and bone ingrowth. Instead of changing porosity, Traxel et al. integrated BCC and hexagonal closed packed (HCP) unit cells in a lattice by different arrangements [67]. The lattice structure integrated with BCC and HCP in a column-layered layout shows the highest stiffness (76.5 ± 20.5 GPa) and yield strength (511.1 ± 125.5 MPa) compared to other designs, resulting from the high crack deflection and toughening of the lattice under compressive loading.

With the aim of trying to mimic native cancellous bone structure, lattices with gradient and stochastic designs have been proposed. Yao et al. [68] found that radially graded lattices presents higher yield strength of 292.16-299.14 MPa than homogenous lattice yielding at 271.65 MPa. The results reflect that more materials distributed at the outer radii of lattices more robustly resist the external load, which is akin to the arrangement of cortical bone. With a compliance to the mechanical strength requirements of cortical bone (elastic modulus 3-20 GPa and yield strength 33-193 MPa), the graded lattice structure reported that achieves the objectives of both maintaining the strength and avoiding stress shielding. In terms of stochastic lattices, Araya et al. assessed the compressive and tensile properties of uniform TPMS gyroid and stochastic Ti64 lattices [69]. Results unveiled that the stiffness of gyroid lattices (13.33-19.95 GPa) outperformed the stochastic (11.88-16.34 GPa) across all relative densities with a predictable stretch-dominated behaviour. While the stochastic structure shows a top-to-bottom collapse with

bending-dominated and less predictable behaviour, possibly attributing to the random nature caused uneven stress distribution.

Researchers have also explored other functional benefits of lattices structures for healthcare applications. For example, the PBF-LB porous implants with a 3.75 times larger surface area than solid Ti64 were embedded with silver nanoparticles through plasma electrolytic oxidation (PEO). Proved that biofunctionalized Ti64 porous structure enables prevention and killing of biofilm formation of *Staphylococcus aureus*, with a four times higher amount of released Ag ions leading to a x2 larger area of bacterial inhibition, and a magnitude reduction in the number of colony forming unit for antimicrobial test compared to solid PEO+Ag [70]. Additionally, two case studies of spinal fusion surgery reported that lattice structures integrated into customised implants were easy to put in place, efficiently shortened procedure time, and avoided complex reconstruction [71]. The 12-months radiological follow-up displayed robust mature fusion without failure of fixation and subsidence.

2.4 Process parameters of PBF-LB

PBF-LB is a complex process, where numerous parameters influence the final part quality. Yadroitsev and Rehme defined 130 and 157 process parameters, respectively by and categorised them as pre-process, in-process and post-process [72, 73]. Among these, the quality of PBF-LB parts mainly depends on laser power and spot size, scan speed, scan strategy, and hatch spacing [74].

Energy density (ED) is a common parameter applied to indicate the combined effect of PBF-LB parameters that significantly associates with the quality and properties of the manufactured part. There are two primary types of energy density to consider: linear energy density (LED) and volumetric energy density (VED). LED refers to the amount of laser energy delivered per unit length of the scan path. It focuses on how the energy is distributed along the path of the laser, as formulated in Eq. 2.1. While VED highlights the laser energy input per volume of materials (Eq. 2.2).

$$LED = \frac{P}{v} \text{ J/mm} \tag{2.1}$$

$$VED = \frac{P}{vht} \text{ J/mm}^3 \tag{2.2}$$

Where:

P is the laser power, W;

v is the scanning speed, mm/s;

h is the hatching space, mm;

t is the layer thickness, mm.

Given the multiple factors involved in the PBF-LB process, energy density does not consider the influence of other parameters, such as the direction of gas flow, scanning pattern, or laser spot size and its offset. Although ED has been popularly used for the optimisation of PBF-LB parameters, it leaves uncertainty to represent the actual energy input to the powder bed [75]. For example, Prashanth et al studied tensile behaviour of PBF-LB part fabricated with (1) consistent VED but varied laser power and scanning speed; (2) consistent scanning speed but changed laser power [75]. For both conditions as the laser power was reduced tensile strength of the parts decreased due to increased defects. This indicates that laser power is one of the most important and effective

parameters to be considered, while the ED can be regarded as a rule of thumb to evaluate the energy input to the powder bed. Nevertheless, ED could be used as a threshold to define the boundary for achieving a fully consolidated structure, which helps to save time for exploring the feasible processing window [76]. However, the more complex relationship between cracking and ED suggests the limitation of using this composited parameter to explain the difference of cracking density due to the complicated laser-material interaction, as well as excluding the energy absorbed by subsequent layers [77].

It is well accepted that the size, shape, temperature and dynamic of the melt pool in PBF-LB plays a fundamental role because it influences the solidification of fused powder and the consolidation of layers. In turn this determines the quality, performance, and reliability of PBF-LB parts [40]. Optimisation of these melt pool characteristics could directly minimize defects, adjust microstructure, enhance mechanical properties and maintain geometric precision. Laser power and scanning speed are the most prominent influencers of melt pool behaviour. Thijs et al. illustrated low scanning speed of 200 mm/s leads to poor stability of the melt pool and coarser microstructure [78]. This instability may contribute to material evaporation from the melt pool, leading to fluctuations and resulting in a keyhole-like effect, which is more prominent under lower scanning speed. On the other hand, high scanning speeds may lead to insufficient melting of metal powders due to short interaction time. An appropriate scanning speed would allow powder particles to absorb sufficient energy for melting, contributing to stable wetting and spreading [79]. Increasing laser power has been evidenced to impact the melt pool dimensions and maximum temperature [80].

The effect of process parameters have been paid further attention to the manufacturing of Ti64 lattice structures by Salem et al. [81]. Laser power range from 100-400 W, and scan speeds from 800-4000 mm/s were assessed to study their effect on the dimensional accuracy of strut thickness and internal defects. The work found that lattices manufactured using a laser power of 100 W and scanning speed of 1600 mm/s could be accurately manufactured with minimal internal pore defects.

The complexity of PBF-LB is pushed to the limits when manufacturing lattices consisting of ultrafine features approaching melting pool size at about 200 μm, as a result, the materials properties start to change [82]. Process parameters adapted to manufacture solid materials need to be adjusted and develop specific processing windows for the fabrication of lattice structures.

2.5 Scanning strategy

Scanning strategy in PBF-LB refers to the pattern and sequence in which the laser beam moves across the powder bed to selectively melt and fuse the material [83]. Different scanning strategies can significantly influence the thermal history of parts thereby impacting resultant properties [41]. Residual stress, internal defects, microstructure, and surface quality can be adjusted and improved through optimising scanning direction, sequence, vector rotation angle, vector length, time and hatch spacing [84]. The most common scanning strategies are uni-direction and bi-direction, which have long scanning vector lengths (Fig. 2.5 (a) and (b)). These two strategies have uniform scan length, the difference between uni- and bi-direction is the changing of scanning direction.

Island strategy has been reported that with a suitable island size of 2.4 mm is capable of reducing residual stress and warping compared to the size below or above this dimension, where the appropriate re-scanning and pre-heating from the previous island release the stress located at the island borders of overlap regions [85].

In fig. 2.5, the scanning sequence is changing between different tracks, which is an alternative method to adjust the temperature distribution in PBF-LB. Helix scanning strategy can also vary the scanning vector length, the laser of which follows a spiral pattern from the centre outward or vice versa. This approach has been shown to reduce warping deformation [86]. Most practical scanning strategies have a contour scan surrounding the bulk volume filled by hatch scanning [87].

Laser re-scanning strategies are typically applied to refine the microstructure of parts with higher mechanical demands. Re-scanning presents as double track with varied or unified scanning vector rotation (Fig. 2.5 (h-m)), this rotation can be adjusted both inter-layer and within the same layer. Point exposure strategy is different from the above continuous scanning, where the laser point is selected rather than continuous, including beam current, beam residence time and point distance as key factors [88].

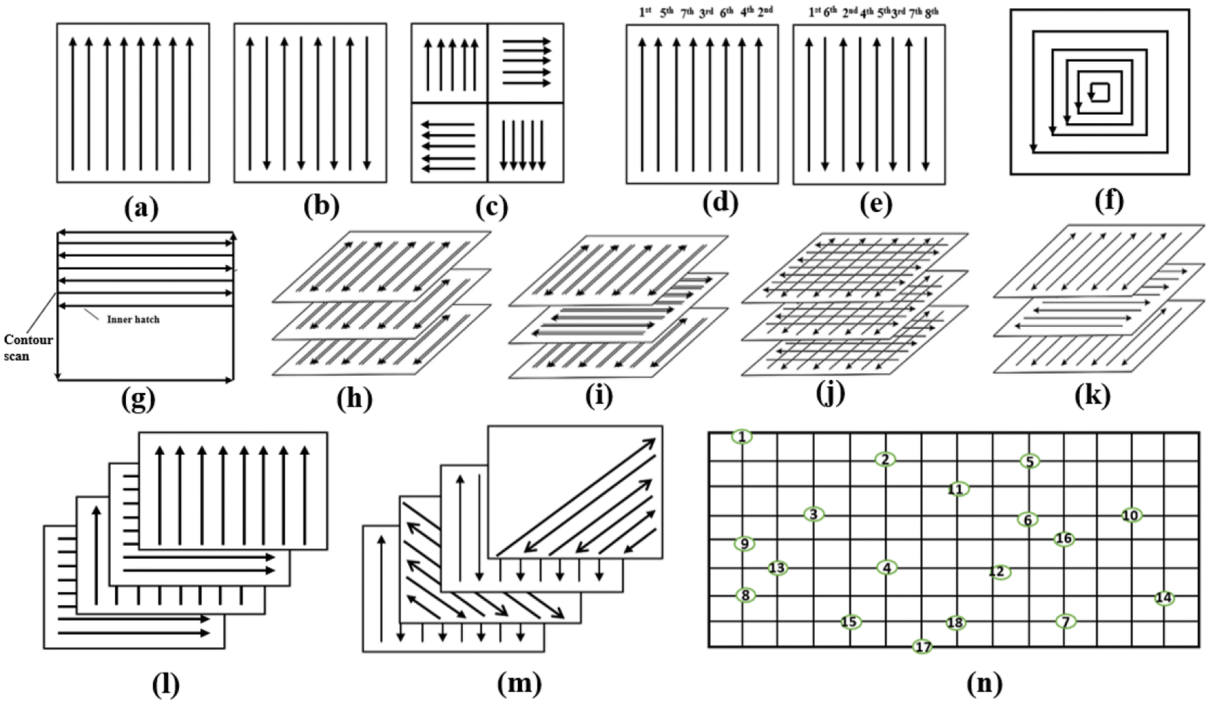

Figure 2.5 Different types of scanning strategies: (a) uni-direction; (b) bi-direction; (c) island; sequence changing of scan for (d) single direction and (e) bi-direction; (f) helix; (g) single contour with hatching (filling); (h) double scan for bi-direction; (i) 90 rotated scan vector with double scan for bi-direction; (j) cross scan; (k) 90 rotated scan between layers for single bi-direction; (l) 90 rotated scan between layers for single scan; (m) 45 rotated scan vector; (n) point melting. Adapted from figure produced for Jia et al, The International Journal of Advanced Manufacturing Technology, 2021.

It was concluded by Jia et al. that the main difference of scanning strategies depends on their re-melting degree, resulting in changes to cooling rates and local heat treatment [83]. Laser re-melting can reduce internal defects, roughness, and improve densification [89]. Internal porosity may also be reduced, which has been attributed to re-melting that in turn may also improve surface finish overall enhancing the reliability of AM parts [90].

Notably most of the studies concerning optimisation of scanning strategies are focused on bulk materials. In the context of this research, it is important to recognise the different regimes required for production of intricate lattice structures. Ultrathin struts have a much larger surface area exposed to the raw material, and more complicated internal topology

suggesting that different thermal behaviour would occur even applying the same strategies as optimised for bulk components [91]. Barba et al. studied different sizes of Ti64 samples fabricated via PBF-LB, indicating that the common fill scanning for larger volumetric material section leads to the microstructure with highly textured columnar structure and grain elongation [92]. While the border contour region results in a fine, randomised and more equiaxed microstructure. There is a lack of comprehensive understanding on the effect of scanning strategy on lattices generally but specifically in terms of geometric reproducibility, mechanical performance, and cellular attachment. As such there is a clear knowledge gap that this research aims to fill in terms of optimising specific scanning strategies for biomedical lattice structures.

2.6 Build orientation

Stair-stepping effect relies on build orientation (as well as layer thickness), which is an inherent surface feature of AM parts [93]. The effect more or less appears in AM as the process is additive deposition and layer-based fabrication. Considering tricky build orientation, overhang features or floating objects, support structures acting as anchors for melt pool heat dissipation, and thermal warping prevention are commonly used [94]. Different spatial direction of parts would cause the difference of overhang area towards the build substrate, some region of the part would need support to be fabricated. Supports influence manufacturability, surface quality and even microstructure of PBF-LB parts, through relating the heat activity between part, powder bed and substrate. Gan et al. found that well designed supports, including the layout, distance and angle allows for more uniform heat dissipation.

As aforementioned, the topology design, struts features relating with build direction would strongly influence the defects characterisation and microstructure. For example, it has been found that the columnar grain grows directionally along the build direction as a result of thermal gradient from bottom to the top of the melt pool [95]. For instance, Xin et al. found that the β phase content and the ultimate tensile strength (UTS) change with build orientation, where the highest content of β phase was observed at 45° (2.8%) where the UTS is lowest (1161 MPa) [96].

Although it has been concluded that the PBF-LB process conditions control the cooling rate during solidification, influencing the microstructure and other as-built quality of PBF-LB parts, the effect of build orientation on the performances of lattice structures requires more attention, and need specific exploration regarding to their complicated geometry [97].

2.7 Manufacturability of PBF-LB lattices

Despite the existence of stiffness-matched lattices have been studied and manufactured, manufacturability of metallic lattices with bone-mimicking properties, such as bone trabeculae thickness (below 400 μm), and gradient porosity (1-100 μm) are challenged by the limitation of PBF-LB [98]. Laser spot size plays a key role for manufacturing limitation, where most of the spot size is set above 50 μm. Yildiz et al. manufactured 316L stainlesss steel by a laser spot size of 50 μm, showing that the potential to manufactured the lattice with fine designs [99].

While AM offers enhanced geometrical freedoms compared to subtractive methods there still exists constrains for PBF. For instance, the overhang surface has a minimum inclined angle, serious distortion would occur in lattices, manifesting as a shape factor deviation from the CAD model that exhibits a circular cross-section to an ellipse. However, this limit of the strut angle depends on the process parameters and materials type [100].

In terms of the dimensional constrain, there is a manufacturing limit of feature size for PBF-LB. This minimum feature size is influenced by process parameter optimisation. For example, Noronha et al. managed to fabricate hollow lattices with 0.2 mm strut thickness by using a double scanning path [101]. However, the laser spot size challenges the minimal feature size of lattice struts or walls to achieve the thickness below 100 μm [91].

2.8 Dimensional accuracy of PBF-LB lattices

The inherent limitation of PBF-LB technology could cause the mismatch of geometry between the as-designed and as-built lattice structures. It can be attributed to the inappropriate selection of process parameters that leads to the under-build or over-build (Fig. 2.6) of lattice structures showcasing a deviation of strut thickness from the design, influencing the relative density and mechanical properties [102]. Qiu et al. also reported that strut thickness increases monotonically with laser power, while scanning speed was observed to increase the strut thickness at slow rates. The strut thickness increased from the nominal 300 μm to as-built 550 μm is associated with a larger melt pool resulting from a higher energy input of 400 W to the powder bed. Moreover, geometric defects such as shrinkage after melting, attached partially melted powders, waviness and roughness of struts influence the dimensional accuracy [103, 104]. Moreover, Mullen et

al. found that the decreasing of unit cell size would increase the strut size, resulting from the diffusion heating of adjacent struts [105]. Specifically, the surrounding powder will heat up for thermal diffusion when the laser interacts with a region. In turn, this diffusion heat tends to increase the size of the melt pool near the solidified struts, leading to thicker struts.

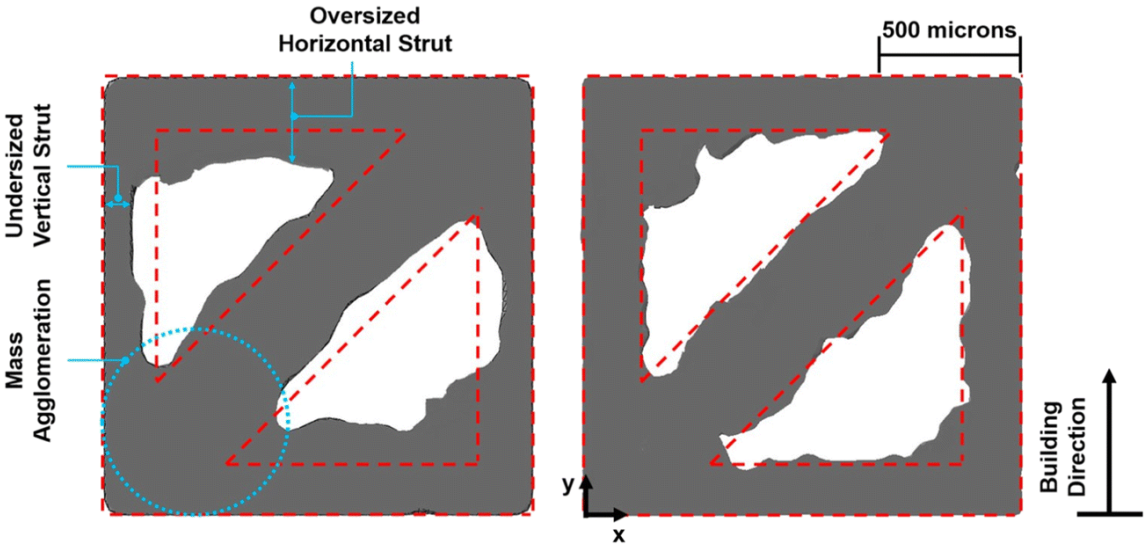

Figure 2.6 CT images of as-built unit cell (left), and the optimised unit cell(right) to offset the under- or over-sizing effect. Red-dashed lines show the designed unit cell form. Adapted from figure produced for Bagheri et al, Journal of the Mechanical Behaviour of Biomedical Materials, 2016.

2.9 Surface characterisation of lattice structures

Surface roughness of lattices has been a main concern for mechanical properties, while maintain certain level of roughness is essential for biointegration. Surface quality is particularly important for fatigue performance, where surface micro-features may become a crack initiation site (CIS) and significantly impact performance [106]. The inherent nature of powder bed processes makes partially melted powder particles attached to the surface unavoidable. As Pegues et al. concluded, this phenomenon is somehow specific to powder bed AM whilst outside the realm of traditional approaches [107]. In

another word, the surface roughness is substantially impacted by geometry and orientation, process parameters such as laser power, scanning speed, scanning strategy and hatch spacing [108]. It is therefore important to comprehensively understand how the process parameters and geometric design affects the surface quality.

The stability, size and behaviour of the melt pool significantly influence the surface roughness in PBF-LB, as Koutiri et al. reported [109]. Under a constant ED, the discrepancy of surface quality is attributed to the scanning speed, where slower speeds tend to promote turbulent melt pool behaviour, leading to degradation of the surface finish due to an increasing likelihood of aggregated spatter particles adhering. A linear model was proposed to illustrate the relationship between laser power and surface roughness [110]. At a constant scanning speed of 250 mm/s and hatch spacing of 78 μm, the average roughness (R_a) decreased from 21 to 9 μm when increasing laser power from 35 to 50 W. Both the top and side surface roughness were reduced since a higher laser power induces large recoil pressure (metal vapor pressure), from which the melt pool is flattened and smoother top surface. Moreover, the increased ED due to laser power improves the wettability of the melt pool, lowering the surface tension between the previous solidified part and present recoated powder layer. Balling effect is thus reduced, and a less rough side surface is formed. Scanning speed shows effect on lower surface roughness via laser infiltration effect reported by Han et al. [111]. They concluded that the lower scanning speed allows longer residence time in melting pool and temperature increasing for good wettability and flowability. The liquid materials infiltrate to the powder gaps and fused with powders leading to lower roughness.

The angle of lattice struts to the build substrate is an important factor that significantly influences surface roughness [112]. As-built PBF-LB specimens show a distinct surface quality when fabricated at a low inclined angle especially at 0. The lower surface (down-facing) manifests higher roughness than the upper surface (up-facing). Briefly, there is fewer part volume beneath the melting area. As these surfaces are actually built on spread powder, whose thermal conductivity is about an order of magnitude lower than the solidified region, more particles are partially melted to the lower surface resulting in higher roughness than the upper [113]. Additionally, melt pool is affected by gravity on unsupported area, leading the wet melting pool sag into the powder particles and rougher surface compared to the upper surface.

2.10 Internal defects of PBF-LB lattices

Before the discussion of internal defects specific to PBF-LB lattices, common defects associated with PBF-LB are introduced. A number of physical phenomena exist in the PBF-LB melt pool system during energy transfer between the laser and powder, which contain laser reaction force, Rayleigh instability, Bernoulli effect, and Marangoni effect [114]. Under the influence of gas-liquid interfacial tension, the disrupted sections of the melting pool tend to roll up into spherical shapes, leading the molten bead to adopt an irregular shape or break apart, known as Rayleigh instability and resulting in the balling effect [115]. The laser reaction force, also referred to recoil pressure impact exerted by the eruption of metal vapor on the melt pool and surrounding powder, which contributes to the occurrence of spatter behaviour. The Marangoni effect, resulting from the mass shift due to the surface tension gradient between two liquids at different temperatures, occurs in the melt pool due to its temperature gradient [116]. As shown in Fig. 2.7, these

physical phenomena contribute to balling, spatter, and keyhole effects, which in turn cause lack of fusion (LoF) and pore defects. In lattice structures, the most common defects are LoF and gas pores both of which are influenced by PBF-LB parameters.

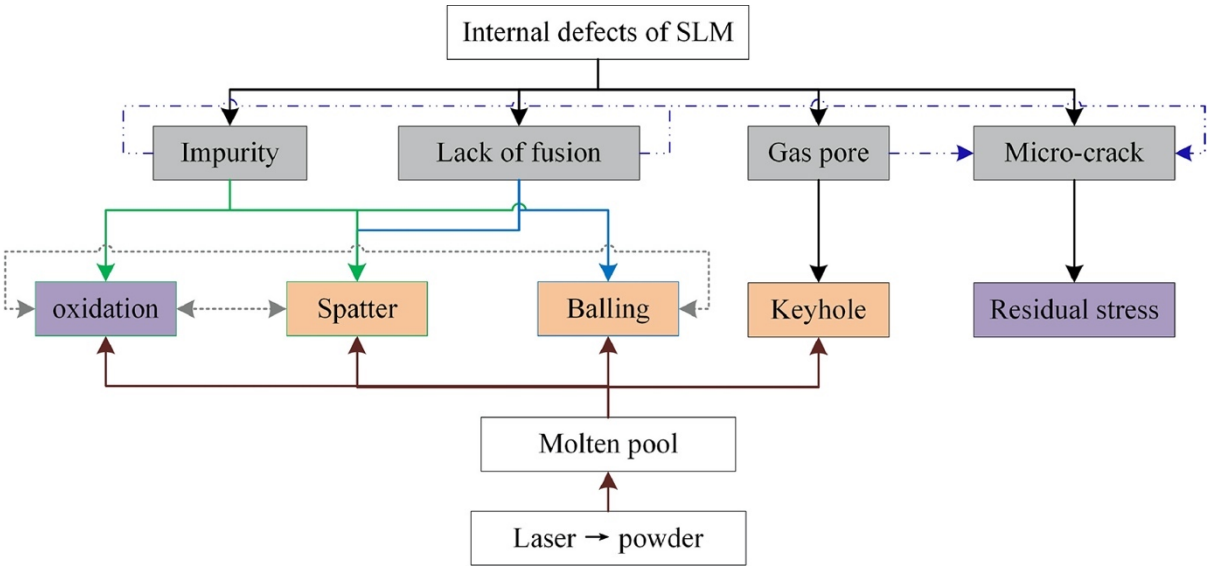

Figure 2.7 Schematic relationship between powder bed fusion melt pool and internal defects. Adapted from figure produced for Yang et al, Chinese Journal of Mechanical Engineering: Additive Manufacturing Frontiers, 2022.

LoF defect is the insufficient melting of metal powders, which could contain and entrap unmelted powders. Zhang et al. categorised LoF into two type: (i) unmelted metal powder defects; (ii) poor bonding defects during solidification [117]. For lattice structures, Salem et al. reported that Ti64 lattices built with a relative high scanning speed of 3200 mm/s and 4000 mm/s were entrapped by unmelted particles inside the LoF gap [81]. This can result from the spatter formed due to high scanning speed. These ejected molten droplets may further agglomerate, which may introduce other internal defects by disturbing the stability and uniformity of layer thickness for deposited powders. LoF defects can trigger a serious problem both on the surface and sub-surface, acting as stress concentration point

and/or crack initiation sites, which further influence both quasi-static and dynamic mechanical properties.

The formation mechanism of these defects were explained by Leung et al. through in situ and high-speed synchrotron X-ray imaging [118]. They reported that increasing scanning speed will increase the surface tension of the melt pool due to the decreasing of laser energy transferred to the powder and the following decreased peak temperature. This will hinder the wettability process and the fusion of the consolidated melting beads into main melting track, leading to a non-continuous final track. Furthermore, it is possible at high scan speeds that the laser beam is moving faster than the melt pool growth rate, if this occurs the liquid metal tends to curl up into a sphere to minimise its surface energy.

In terms of the spherical gas pores, during the rapid printing process, the complicated thermal history involves repetitive high energy melting and rapid solidification. High energy input can lead to pores with spherical shape due to gas entrapment. For the occurrence both of two defects, the density of lattices will decrease.

Keyhole is another internal defect formed during PBF-LB under high laser power and low scanning speed. Compared to gas pores, keyhole has a high depth-to-width ratio with a deviation from circularity [119]. Keyhole formation is attributed to the intense vaporization of the liquidised metal surface, which appears when the melting temperature reaches the material boiling point. The vapor metal may be entrapped inside the conically shaped molten part depressed by accompanied recoil pressure. Moreover, the deep penetration of laser beam inside the generated keyhole continuously being absorbed and

reflected, causing more input energy absorption by the materials resulting in a deeper melt pool.

In terms of defects in lattices, it was observed by Yan et al. that the porosity (enclosed voids beneath the part's surface) increased 10% when increasing the gyroid unit cell size from 2 mm to 8 mm under constant process parameters. They assumed that the longer scanning tracks for larger unit cell creates longer time for pores to generate in between the adjacent scanning paths [120]. Besides, porosity was found increasing at the nodes area of lattices, which can be attributed to the scanning strategy [121].

Build orientation was found by Dong et al. to impact the number of pore defects in PBF-LB lattices [122]. The porosity decreased from 1.95 to 0.11% when the orientation angle of lattice struts was increase from 35.5° to 90°. The pores were observed to be more concentrated in the lower surface region than the upper surface. These results were attributed to cooling mechanisms, as the lower angle struts experience lower cooling rates due to a greater contact area with support powder, leading to higher temperatures remaining and the following pore formation. This difference in defects further influence the ultimate tensile strength, where a 22% higher strength was obtained for lattice struts built at 90° compared with 35.5°.

2.11 Microstructure of PBF-LB Ti64 lattices

Despite numerous advantages of PBF-LB, one of the greatest challenges is the effect of the rapid and directional solidification process on Ti64 microstructure [107]. Like other alloys, the mechanical performance of Ti64 is governed by its underlying microstructure.

To increase the as-built density of the products, energy input accompanied with a high cooling rate is required to avoid pore defects as aforementioned, high temperature gradient would further result in the formation of HCP acicular α′ martensite microstructure of Ti64 [78, 123-125]. It is well known that this ultrafine microstructure could lead to relative high strength but poor ductility. The phase contents and microstructure features of AM Ti64 part depends on the thermal history they experience, including initial cooling, and the following in-process re-heating/cooling. Phase transformation changes from martensite, fine Widmanstätten, coarse Widmanstätten, to fully lamellar with the decreasing of cooling rate, namely, from the HCP acicular α′(α′′) to α + β (Fig. 2.8) [107].

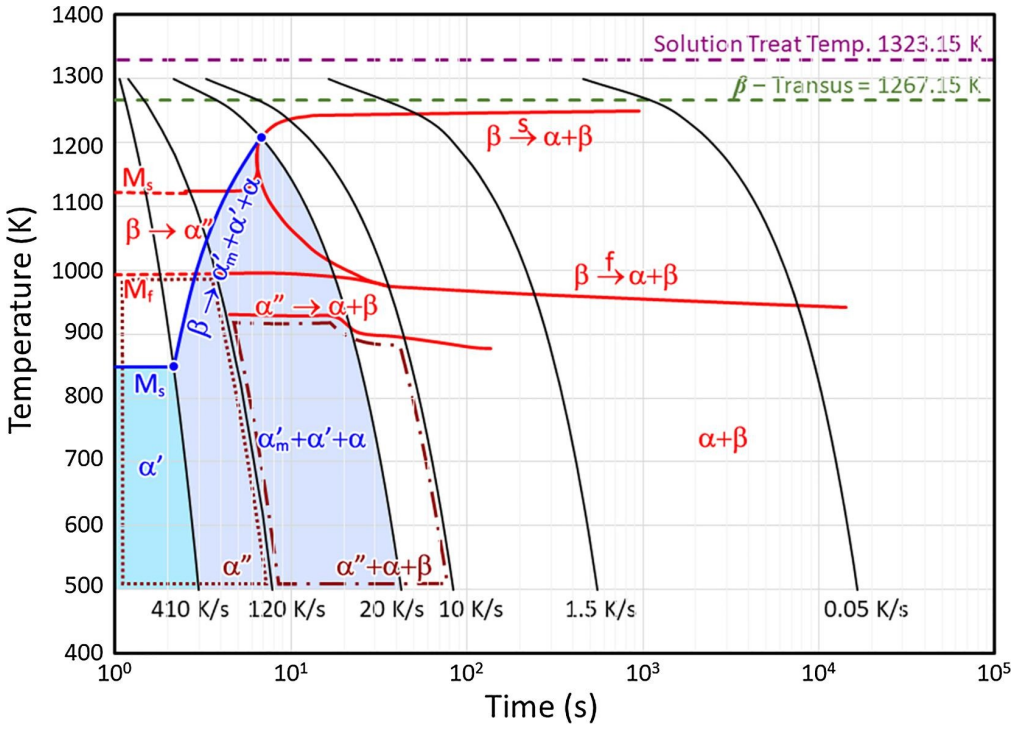

Figure 2.8 Diagram showing the continuous cooling transformation for Ti64 covering above β-transus temperature to 500K, and the α' is showed in blue zone while α'' in cyan. Adapted from figure produced for Pegues et al, International Journal of Fatigue, 2020.

β grain characterisation depends on cooling rate and thermal gradient, which relates with PBF-LB laser power, scanning speed during solidification [126]. In this thermal-based process, the solidification happens via the existed β grain growth from the previously deposited layers. The previous deposited layers partially melted during the repetitive melting and solidification process lead to the epitaxial solidification, which improves the mechanical strength but lowers ductility of the whole lattice structure [127]. Besides, the directed rapid solidification can result in refined grains to avoid dislocation movement and thus, higher resistance to deformation. Under as-built state, there are numerous defects that exist in the acicular α′ / α martensite matrix. These defects with limited slip distance could be easily blocked inside a single α′ / α grain, even under continuous compressive loading. Moreover, the grain boundary of α′ / α acts as a strong barrier to inhibit the dislocation glide effectively, deteriorating the compressive ductility.

Amounts of factors have been found associating with the cooling rate during PBF-LB. For example, the cooling rate may vary depending on the local geometry within the same part. More specifically, when the laser interact with the powder bed, the heat conducts inside powder materials could be much less than the solidified region. Xu et al. has concluded that the higher cooling rate could be increased when the melting location is thicker or above effective heat sinks, vice versa [125]. Batch size could also influence the cooling rate through the inter-layer time (dwelling time) which relates with the part cooling down between each deposited layers, where larger batch size leads to higher cooling rate and finer α plates or martensitic transformation [128].

Heat-treatment is necessary for PBF-LB parts to relief the residual stress and/or modify the microstructure to allow the products to acquire desirable mechanical properties, fatigue performance in particular. As stated, due to the high cooling rate of PBF-LB, the acicular α′ martensite dominates the as-built parts, the ductility of which is limited by the ultrafine HCP and the tendency towards the intergranular failure along the prior grain boundaries. Two main heat treatment approaches are to maintain the maximum soak temperature below β-transus temperature [107], or exceed the β-transus. The former would acquire globular primary α whilst the part obtaining both high strength and high ductility. While the latter would transfer the microstructure to fully lamellar or basketweave, performing a lower ductility but higher fracture toughness due to the lamellar grains functioning as crack deflectors [107].The high temperature and pressure of hot isostatic pressing (HIP) can also be a possible solution of post treatment for PBF-LB Ti64 components. It has been observed that the high cycle fatigue (HCF) performance improved after HIP, which was attributed to reduced defect size that can initiate fatigue cracks, and the changing of microstructure surrounding defects [129, 130]. On the other and, the HIP treatment might be counteracted, due to the Argon existed inside internal pores that failed to diffuse causing tensile residual stress. Hence, this highlights the importance of exploring and customising the treatment process for AM products. However, the ultimate goal of applying AM is to produce the parts at an as-fabricated stage comparable and improved properties than the post-processed state [131].

2.12 Mechanical performance of PBF-LB lattices

Typically, the topological layout of struts in the macro level, with the elastic-plastic deformation of base materials together decide the mechanical properties of lattice

structures [132]. The materials mainly influence the plateau stress and energy absorption, while the topology layout governs the elastic modulus and yield strength. Moreover, given the lattice structures for orthopaedic devices experiencing cyclic loading, fatigue fracture is considered as the main failure mode, resulting from stress concentration, defects, and residual stress. Hence, understanding the fatigue mechanism of Ti64 lattice structures is a premise for pursuing potential lattice structures with desirable fatigue performance [44].

2.12.1 Quasi-static compressive properties

As aforementioned, the stiffness of PBF-LB lattice structures should match as closely as possible to the host bone due to the detrimental impact of stress shielding [15]. Both the elastic modulus and the yield strength are crucial to lattices as biomedical devices, and it is also important to distinguish the two properties.

There are mainly three stages (Fig. 2.9) of the deformation behaviour for lattice structures under quasi-static compressive loading: linear elastic stage, plastic deformation stage after yielding, and the fracture followed by densification [50]. It is common that the struts of lattices gradually deform and then collapse due to the compressive loading, following initial yielding, buckling, and final fracture. At the initial elastic deformation stage, the stress-strain curve is linear, as well as the deformation of lattice in this stage is reversible without permanent distortion. The behaviour of individual struts within the lattice determines the overall elastic response [133].

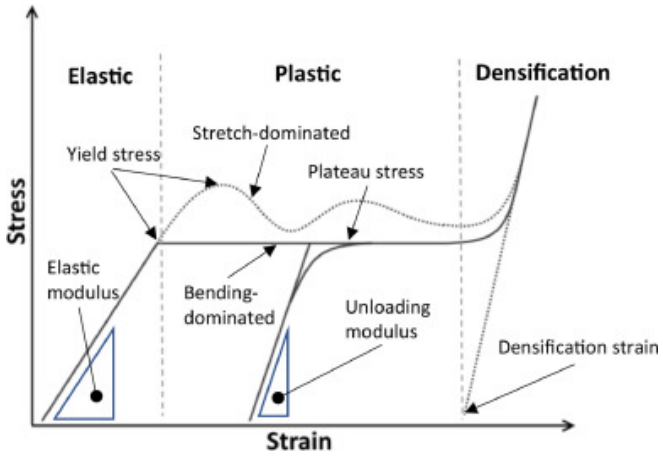

Figure 2.9 Different mechanical behaviour for bending- and stretch-dominated lattices. Adapted from figure produced for Maconachie et al, Materials & Design, 2019.

After the elastic deformation ends, the lattices would reach the yield point, the stress of which is yield strength. Two different deformation behaviour would occur in the plastic stage according to the type of lattice structures after yielding. Unit cells start to irreversibly deform, where a flat plateau could be observed for the bending-dominated lattices, whereas the stretch-dominated lattices exhibit increasing or oscillating behaviour due to the sequential collapse of weak compressive struts and strong tensile struts [134]. The two distinctive deformation of behaviour result from the different arrangement of struts determining the transferring mode and the distribution of loading. The Maxwell number, M, of a lattice can be calculated in Eq. 2.3 to define if the design is bending-dominated ($M < 0$) or stretch-dominated ($M \geq 0$) by,

$$M = s - 3n + 6 \tag{2.3}$$

where s is the number of struts, and n is the connecting nodes.

There are different failure modes observed during the compressive test, including continuous unit cell collapse, crack propagation in lattice structures, and diagonal shear

(Fig. 2.10) [135]. Diagonal shear is characterized by a distinct shearing angle, typically around 45˚ to the applied load [136]. In the research of He et al., they use finite-element analysis (FEA) to simulate the deformation mode under compressive load [137]. The results showcase that at the early stage, the stress was primarily accumulated at vertical struts and then transferred to the intersecting diagonal struts when the load gradually increased, leading to the bending and fractures at the vertical struts and nodes along with the 45˚ shear band. For the glass sponge structure they developed, the stress initially accumulated at the vertical struts along the loading direction in the circle-like unit cell and fractured. Then the stress transferred to the adjacent unit cell. Hence, it shows a cell-by-cell and layer-by-layer fracture mechanism. In contrast, the diagonal struts of diamond lattice exhibited bending behaviour and fractured at the connecting nodes at the top layer due to the lack of connecting struts, occurring as crack propagation in lattices.

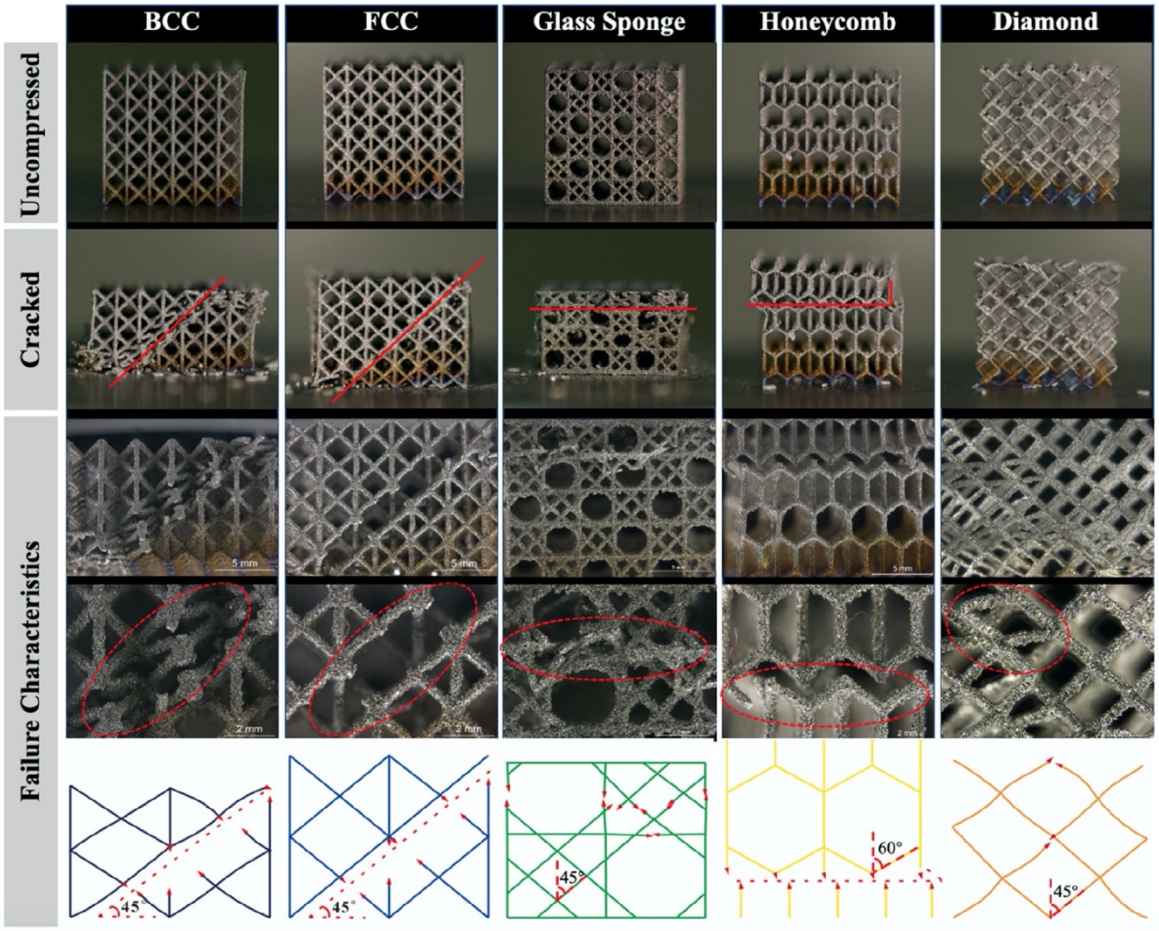

Figure 2.10 Optical microscopic images showing uncompressed, cracked, and failure of five different lattices including BCC, FCC, Glass sponge, honeycomb, and diamond. Plus the schematic diagram displaying their fracture characterisations. Adapted from figure produced for He et al, Materials & Design, 2022.

Noticeably, while the BCC and FCC present a bending-dominated mechanical behaviour, their variations with added vertical z-struts, known as BCCZ and FCCZ behave a stretch-dominated deformation. These stiffer and more robust variations of BCC and FCC with realignment of struts are not complying with the Maxwell criterion. Moreover, lattices typically comply with the Gibson and Ashby model, by which a range of mechanical, electrical and thermal properties of porous structures can be predicted based on the relative density of the structure and calculated as fractions of the parent material's property [51]. However, these models might not work for some unusual lattices

topologies [62]. It was thus suggested that the BCC should be the first choice among Ti64 and strut-based lattices, as the BCC and variations of BCC exhibit the highest yield strength compared to FCC, diamond and simple cubic structures, where the BCC-based lattices with a larger struts thickness of 0.575 mm observed the highest yield strength of 435 MPa, the second highest yield strength of 349 MPa was exhibited by the node-reinforced Ti64 BCC [138, 139].

2.12.2 Fatigue behaviour of PBF-LB lattice structures

Biomedical implants, such as orthopaedic devices of hip and knee replacement, and dental implants, are subjected to repetitive loads during walking, standing, running and chewing over extended periods [140, 141]. The capability of implants to withstand cyclic loading without failure is essential for the longevity and reliability of the device. Fatigue failure could lead to implant breakage or loosening, necessitating revision surgery. Fatigue performance of lattices thus plays a key role for skeletal implants and the mechanism of lattice fatigue need to be continuously investigated and optimised.

Lattices experience three stages under fatigue loading, the initial strain increasing drastically due to the adjustment of structure under cyclic loading [142]. Microstructural changes and early damage mechanism, such as crack initiation starts to appear. It involves cyclic ratcheting defined as a progressive accumulation of plastic strain with each load cycle [143]. This accumulation is influenced by the local geometry and topology of the lattice structures. Microstructural defects like dislocations and microcracks may form or propagate, but they are generally not significant enough to cause immediate failure. During this intermediate stage, the cumulative strain remains approximately constant over

a large number of cycles, typically ranging from 10^4 to 10^6 cycles. The rate of crack propagation slows down, and the material enters a steady-state phase where existed cracks grow slowly and new cracks form at a reduced rate [144]. This stage represents the endurance limit of the material, where it can withstand cyclic loading for a significant number of cycles without substantial additional damage. In the final stage, cumulative strain increases exponentially. This is often due to the coalescence of microcracks into larger cracks, leading to significant reductions in the cross-sectional area. The structure eventually experiences rapid failure as critical cracks propagate through the lattice, causing the final failure characterized by a dramatic drop in the load-bearing capacity.

Based on the literatures, there are numerous factors affecting fatigue performance, which can be generally distinguished as external and internal [44]. It was concluded by Liu et al. that external factors include the topological design, fabrication process, and manufactured quality of lattice structures. For the internals, there are factors of residual stress, chemical composition and microstructure of the material on fatigue. To decide the most dominant factor, Ahmadi et al. evaluated the effects of Ti64 and Co-Cr as material factor, truncated cuboctahedron, rhombic dodecahedron, and diamond with varied relative densities as topological design factor on lattice fatigue properties [132]. They concluded that the effect of materials type tends to be more substantial than the topological design. The results in fig. 2.11 show that the normalized S-N curves of lattices with same unit cell type but two materials are in different level, while the fatigue strength of different unit cells but same materials tend to overlap. This phenomenon can be attributed to the rougher surface of Ti64 (R_a = 48.46 μm) than Co-Cr (R_a = 25.85 μm) acting as CIS, as well as the difference in grain morphology for two different materials.

As aforementioned, for Ti64 lattice structures, the rapid cooling rate of PBF-LB results in the formation of acicular martensite microstructure, from which the cracks grow along the grains and weaker resistance for crack growth than Co-Cr. While for using consistent material, the connection, distribution, and build angle of struts between nodes, i.e. the topology feature, plus the defects inherited from PBF-LB are the key for mechanical response.

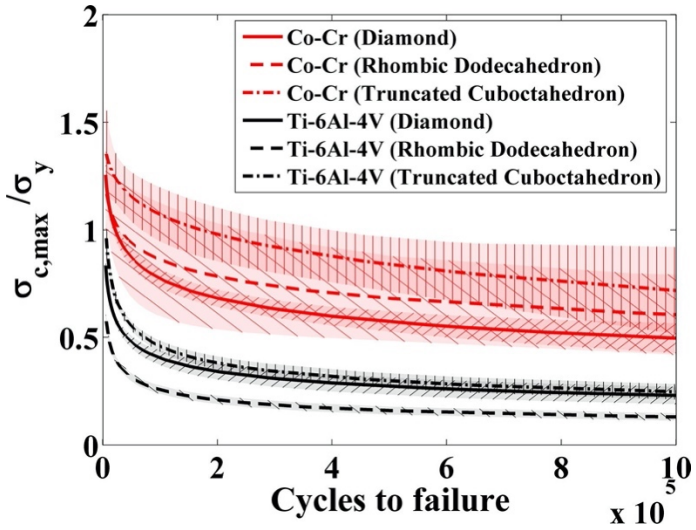

Figure 2.11 The comparison of normalised S-N curve based on different materials of Co-Cr and Ti64, and three topological structures of diamond, Rhombic Dodecahedron and Truncated Cuboctahedron. Adapted from figure produced for Dutta et al, 3D Printing in Biomedical Engineering, 2020.

Higher relative density generally increases the fatigue life due to greater load distribution and lower stress concentrations (fig. 2.12(a)). The increasing of relative density on fatigue was observed to improve not only the fatigue life (fig. 2.12(b)), but also a linear increase in stiffness and strength under quasi-static compression test [145]. The geometric arrangement of the lattice cells affects how stress is distributed and how damage propagates. For example, certain topologically optimised BCC with fillets has been shown to offer better fatigue strength of 0.323 MPa benefitting from the stress

concertation relief at the round corners, compared to 0.269 MPa of the regular BCC lattices [146]. In addition, the truncated cuboctahedron unit cell performs a longer fatigue life than that of diamond topology when the same normalised stress level was applied [147]. More basically, the shape, size, and distribution of struts within the lattice influence the local stress concentrations and overall fatigue resistance. Meanwhile, the fatigue performance of AM lattice structures are largely influenced by the microstructure, manufacturing defects, surface quality and residual stress, which in turn significantly relies on the process parameters and post treatment [148]. Mahmoud et al. explored lattices with same topology but varied struts thickness and the thinner struts exhibited higher fatigue life due to lower amounts of internal defects [149].

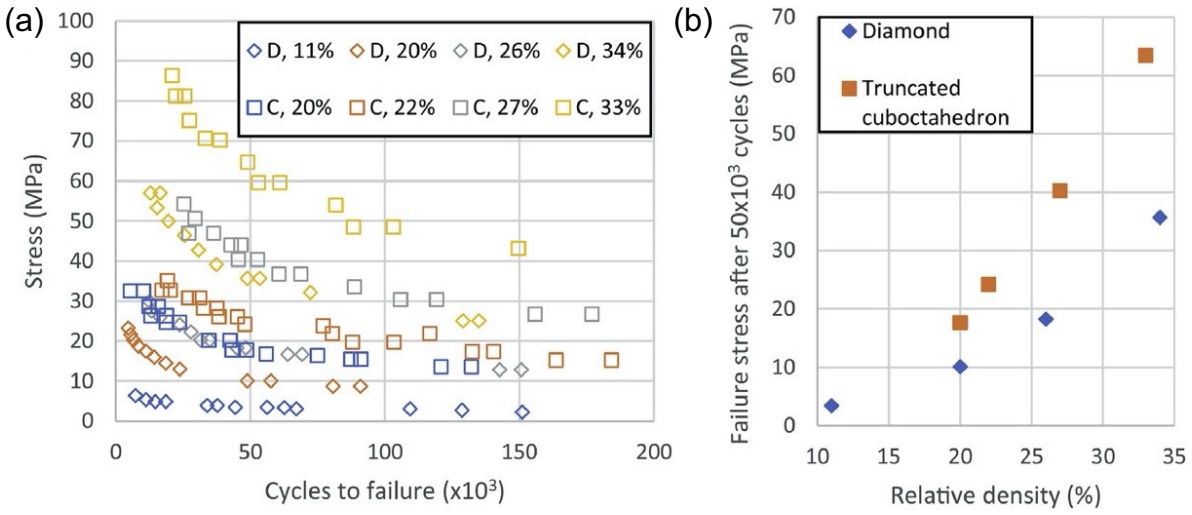

Figure 2.12 (a) Fatigue behaviour changing with relative density of lattices; (b) influence of unit cell type and relative density on fatigue. Adapted from figure produced for Yavari et al. Journal of the Mechanical Behaviour of Biomedical Materials, 2015, and Maconachie et al, Materials & Design, 2019.

For lattice structures, especially during the HCF test, stress concentrated at and close to the defects would be detrimental and aggravate the localised plastic deformation, although the mechanical response appears to be reversible elastic [150]. The status of the

plastic deformation adjacent defects relates with the size, location and morphology of the defects and the characteristics of the surrounding microstructure including grain size, crystal orientation, and phase composition, compare to the latter, the features of defects are a more crucial role in the initial crack growth. Among the defects, the LoF during PBF process is the most harmful to fatigue properties. Hence, optimisation of PBF-LB process parameters is extremely important to improve the fatigue performance for lattice structures and further extend the lifespan of biomedical devices for patients. It is obvious that the PBF-LB process, topology and fundamental strut features are key factors to the fatigue behaviour, which require a more comprehensive understanding of the driving mechanism to enable the root cause to be addressed.

2.12.3 Computational predictive models for lattice structures

Various selections of topology decide different mechanical properties of lattices. Therefore efficient models are essential to improve the predictability of mechanical behaviour and failure response of skeletal devices, as well as ensuring that the design requirements are met [151]. FEA is mainly discussed in this work, as the FE model with high-fidelity could predict the mechanical properties considering various lattice topology and sturt imperfections [152]. Two main factors determine the accuracy of FE model for biomedical lattices, one is the type of element applied, and the other is the actual geometry or fidelity of the lattice structures.

X-ray micro-computed tomography (CT) is applied to identify the defects and geometrical imperfections of lattice structures [153]. Then by using extraction technique, the entire lattice structure is modelled and segmented to gather the data of strut, which

may be potentially used for FEA. Another research quantified the population of defects in lattice structures and a conformal FEA model was created to simulate the compressive response [121].

2.13 Residual stress

Residual stress remained inside the Ti64 structures is another challenge attributed to the high cooling rate and temperature gradient during the manufacturing process. Residual stress is almost unavoidable during the layer-wise scanning. The existence of residual stress has been found largely impact the crack propagation behaviour, which is detrimental to the biomedical devices requiring load-bearing property and long-term lifespan. Fig. 2.12 (a) and (b) shows the stress formed in a new layer through fast heating and cooling [154]. This repetitive heating and cooling will lead to the formation of compressive and/or tensile stress for the neighbouring layers. Pre-heating is considered to be an effective way to control residual stress of the as-built PBF-LB products, Vora et al. found that the preheating process of powder was managed to reduce residual stress for AlSi12Mg parts [155].

It is well-known that the scanning strategy can influence the accumulation of residual stress during PBF-LB. It was concluded that the length of scanning vector has the most significant effect on residual stress [156]. Therefore, controlling the length of scanning vector can reduce the interval time of deposition between two neighbouring scanning tracks. In this case, the heat will be maintained to some extent on the previous track, the current track can be deposited on warm materials to decrease the thermal gradient. Scanning strategy has been reported to significantly influence the residual stress within

as-fabricated Ti64 parts. However, the determination of residual stresses becomes more complicated with increasing complexity of the structures investigated. The effect of this on the residual stress of lattice structures are rarely studied.

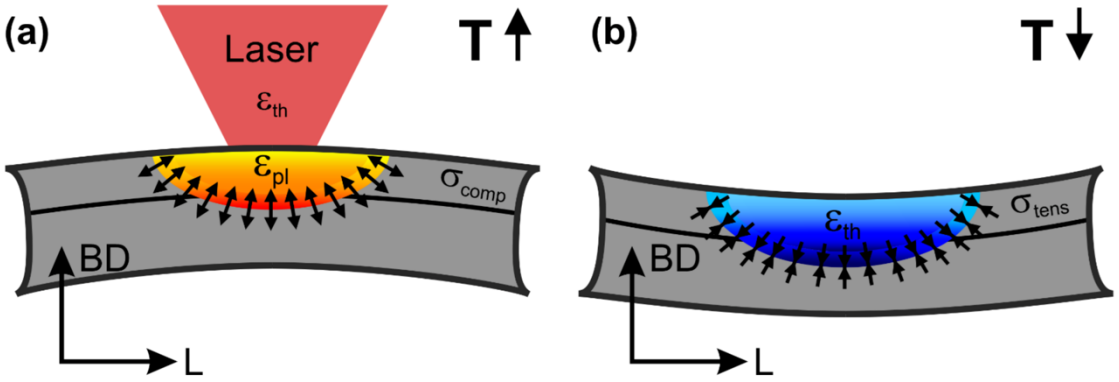

Figure 2.13 Schematic showing residual stress existed in PBF-LB parts during (a) heating and (b) cooling process. Adapted from figure produced for Schroder et al, metals, 2021.

2.14 Biological response of PBF-LB lattices

Different geometry features including designed porosity and unit cell type directly associate with the interaction between implants and the host tissue. For instance, the oxygen and nutrients transfer can be obstructed by the small pore size, resulting in the decreasing of cell proliferation and maturation, as well as inappropriate bone-implants integration. Thus, it has been suggested that the minimum pore size should be limited at 100 μm to ensure suitable cell attachment and proliferation [157]. Cheng et al. concluded that the increasing of porosity can raise the surface area to volume ratio, facilitating more cell interaction to the increased surface area [158]. Besides, the rough curved surface area accompanied with higher porosity enables more mechanical force to be transferred to the cell, which may help to drive osteogenic differentiation. However, large porosity could

decrease the mechanical strength due to the decreasing relative density of lattice structures. In addition to porosity, Deng et al. studied the effects of unit cell type on bone regeneration, indicating that by the same porosity and *in vivo* experiments, diamond lattice is the optimal one to promote bone growth compared to the other three common porous structures [64].

As Yan et al. reported a rough surface can facilitate the adhesion of osteoblasts and the function of bone regeneration [61]. Firstly, the rougher surface can increase the surface area for cell adhesion, improve the surface energy of lattice structures, which enhancing the attachment of macromolecules and cells. Secondly, rougher surfaces are compatible in terms of curvature to the bone cell, promoting the physical and/or chemical combination for the macromolecular or cell. Moreover, the friction coefficient of rough surface for the PBF-LB lattices is higher than traditional implants materials, which strengthens the primary fixation and fusion between the implants and human tissue. Hence, it is reasonable to accept that a rougher surface is beneficial to the biocompatibility of bone implants. Meanwhile, the attached large particles to the PBF-LB surface can hinder the attachment of cell, as well as the risk of shedding could be detrimental to patients' health. Considering the antibacterial aspects, Villapún et al. developed a tool to selectively improve the cell attachment as well as reducing bacterial adhesion [131]. Taken together it is clear that appropriate surface roughness can facilitate mammalian cell response on the meta-biomaterials. As an example of this, it has been shown that strut angle (parts inclined angle) can be efficiently controlled to adjust the surface roughness of implants, achieving the function of promoting the pre-osteoblast response whilst restricting the formation of bacterial biofilm [112, 131].

2.15 Concluding remarks

PBF-LB metal lattice structures are a popular topic since their tailorable mechanical performance make them an effective tool in tackling unmet clinical challenges within the orthopaedics sector. PBF-LB parameters, geometry design, and their effects on the final lattice products still limit the fully development of potential in PBF-LB lattices.

As Pegues et al. reported that the specimen diameter and build angle can influence the thermal history, and further the residual stress, microstructure and the characteristics of defects, relating with the mechanical performances [97, 106]. It was reported that the as-built parts fabricated in different direction show significant anisotropy in fatigue performances, where the vertically built part has lower fatigue life compared to the horizontally built part through PBF-LB. This can be attributed to the larger LoF defect projection area normal to the loading axis than other directions. Although during the PBF-LB, the directed prior- grain influencing the mechanical properties, the research show that the anisotropy of HCF mainly depends on the features and existence of LoF defects influencing the initiation and propagation of fatigue cracks rather than the microstructure characteristics. LoF defect was found at the CIS by Edward and Ramulu from the fractography images, associating with the build orientation. On the other hand, spherical defects were found in build orientations of vertical, diagonal and horizontal, of which the projection area are consistent in all directions, there is no obvious anisotropy found for the mechanical properties.

These issues can be potentially reduced or addressed through optimising process parameters and the geometric design. Considering the load-bearing requirement of biomedical devices, predictive tools are needed and should be developed to further improving and predicting the properties of lattice structures.

Through the literature reviewing, the knowledge gaps and the undertaken investigation work to potentially address the challenges within this thesis are shown as follow:

- There is a need to develop bespoke processing windows for lattices, especially when trying to reproducibly achieve ultrafine structures
    - Processing window consisted of laser power and scanning speed has been evaluated and developed to accommodate specific requirements of lattice manufacturing with improved accuracy and porosity.
- There is limited existing literature focused on evaluating the influence of scanning strategy on the performance of ultrafine lattice structures
    - This thesis has developed a single and multi-contour study to optimise scanning strategy for lattice structures, and evaluated the effects on key characteristic properties
- The lack of fundamental understanding of lattice elements – struts.
    - A map was developed according to the study of struts angle and process parameters, indicating properties variation of lattices struts via design.
- The lack of research on applying rotation strategy on fatigue and biological response on lattices.
    - The effects of different rotation strategies on lattices were studied and presented.

Chapter 3 OPTIMISATION OF SINGLE CONTOUR STRATEGY IN PBF-LB OF TI-6AL-4V LATTICES

Abstract

PBF-LB is increasingly used to manufacture bone implants from titanium alloys with particular interest in porous lattice structures. These complex constructs have been shown to be capable of matching native bone mechanical behaviour leading to improved osseointegration while providing numerous clinical advantages, encouraging their broad use in medical devices. However, producing lattices with a strut diameter similar in scale to a typical PBF-LB melt pool or using the same process parameters and scan strategies intended for bulk solid components may lead to geometric inaccuracies.

Herein, we explore the potential of an unfilled single contour (SC) scanning strategy to improve the reproducibility of porous lattices when compared with a standard contour and fill approach (SC+F). For this purpose, two parametric analysis were carried out on Ti-6Al-4V diamond unit cell lattices with different strut sizes and scan strategies. Porosity and accuracy measurements were correlated with processing parameters and printing strategy to provide the optimal processing window for lattice manufacturing.

SC is shown to be a viable strategy for production of Ti64 lattices with a strut diameter below 350 μm. Parametric analysis highlights the limits of this method in producing fully dense struts with energy density presented as a useful practical tool to guide some aspects

of parameter selection (Design strut diameter achieved at ~ 0.1 J/mm in this study). Finally, a process map combining data from both parametric studies is provided to guide, predict and control lattice strut geometry and porosity obtained using the SC strategy.

These results explore the use of non-standard single contour (SC) scanning strategy as a viable method for producing strut-based lattice structures and compare against the traditional contour and fill approach (SC+F).

ACKNOWLEDGEMENT OF CONTRIBUTING MATERIAL AND AUTHORS

Content within this chapter has been published in the following journal paper(s):

- X. Cao, L.N. Carter, V.M. Villapún, F. Cantaboni, G. De Sio, M. Lowther, S.E.T. Louth, L. Grover, P. Ginestra, S.C. Cox, Optimisation of single contour strategy in selective laser melting of Ti-6Al-4V lattices, Rapid Prototyping J (2022).

As primary author, X. Cao produced all written work within this publication and performed primary experimental work. The contributions of co-authors are as follows:

- Dr. L.N. Carter: Conceptualization, Supervision, Editing
- Dr. V.M. Villapún: Matlab coding, visualisation
- F. Cantaboni, G. De Sio, Dr. M Lowther, and S.E.T. Louth: Experiments, software
- Prof. L. Grover, Dr. P. Ginestra, and Dr. S.C. Cox: Editing and Supervision

3.1 Introduction

Demand for orthopaedic implant surgery is predicted to exceed 5 million worldwide by 2021 with up to $65 billion in revenues estimated by 2025 [159]. The freedom in design inherent to metal Additive Manufacturing (AM) and the expected rise in demand is stimulating research to add further functional properties to implantable devices boosting their application in medicine. In load-bearing implants, latticed structures have the potential to mimic the mechanical response of bone, reducing the stress shielding effect and limiting implant loosening [160]. These porous structures also have the potential to improve cell adhesion and osseointegration, thus strengthening the mechanical bond between patient and implant [161, 162]. Consequently, when applied correctly to bone and tissue scaffolds, titanium AM lattice structures have the potential to meet their fundamental requirements, namely: biocompatibility; surfaces suitable for cell attachment; interconnected porosity enabling cell ingrowth, transport of nutrients, and release of waste; and mechanical properties matching surrounding tissue [163]. It has been demonstrated that unit cell design and pore size influence cell proliferation during in-vivo studies [164, 165] with research by Van Bael et al. concluding that graded pore sizes in tissue scaffolds may promote initial cell attachment within fine pores developing in to tissue growth without occlusion as pore size coarsens [166]. Significant interest in this topic has prompted comprehensive reviews [163, 167] and the creation of design libraries to aid unit cell selection in tissue scaffolds [168]. Finally, potential novel applications include the use of lattices as reservoirs to deliver antibiotics, growth factors, or other treatments directly to the implant site and Magnetic Resonance Imaging (MRI) artefact mitigation [169, 170]. Nevertheless, in order to exploit these benefits, accuracy, predictability, and consistency of lattice production must be ensured.

PBF-LB is an AM technology whereby fully dense components are produced via layer-by-layer laser melting of metallic powder [171-173]. With a relatively high resolution and without traditional machining constraints, PBF-LB presents a suitable method for production of components with integrated lattices. Part performance depends on the physicochemical properties of the powder feedstock and the PBF-LB processing parameters. Powder quality is typically determined by supplier specification, however, process parameters may be directly assigned by the PBF-LB operator, heavily influencing the final part [174]. Laser power and scan speed represent two key process inputs [175-177] which control both melt pool size and shape further determining dimensional accuracy, microstructure, mechanical properties, and surface quality [178, 179]. Energy density, E (J/mm) as defined in Eq. 3.1, combines these inputs to provide a simplified variable which may be useful in understanding certain behaviours [179, 180]:

$$E = \frac{P}{v} \text{ J/mm} \tag{3.1}$$

Where P is laser power (W) and v represents scan speed (mm/s).

The effect of E, P, and v on surface roughness, porosity, and accuracy have been widely reported and trends linking process parameters to part quality identified [181-183]. Researchers have previously shown that increasing laser energy density and build angle induces greater surface roughness [182, 184, 185], however, special care has been taken to understand the role of these inputs in internal porosity and defect type [186]. Porosity from trapped or evaporated gas in powder feedstock occurred at low scanning speed around 800 mm/s, while keyhole porosity is reportedly dominant at higher energy density conditions corresponding to a deep melt pool. Other reported defects include irregular

and spherical shapes at high scan speed (2400-4000 mm/s) and lower laser power (100-300 W) due to melt track balling and lack of fusion. These results have been further supported by the work of Qiu et al. [187], although discrepancies on the optimal processing window can be found in the literature. This is highlighted by Gu *et al.* who showed internal porosity variations from 0% to 5.4% under a fixed "optimal" energy density (61 J/mm^3) by changing laser power and scan speed, suggesting that whilst energy density may be useful in some cases, the influence of individual parameters should not be overlooked [188].

When processing fine lattice structures, strut thickness has been shown to significantly deviate from the initial CAD design. Yan et al. revealed up to 90 μm discrepancies with lattice strut design diameters between 420 μm and 610 μm [189]. This was confirmed by bulk analysis showing printed lattices being denser (10.66% and 13.12%) than the design (10% and 12%), which would lead to inconsistencies in mechanical properties between design and final part. A similar study found a linear relationship between lattice strut thickness and energy density with limited to no influence caused by scan strategy, build angle, or material, resulting in an increase in Young's modulus [190]. On the other hand, the work of Onal et al. suggests that these discrepancies in design rise with exposure time and laser power that subsequently stabilised for energy inputs above 0.5 J for produced lattices via a single point exposure scan strategy [191].

The reported mismatch between design and manufactured geometry in these intricate structures is further complicated by the pre-processing software logic used to generate the laser path for each strut slice (Fig. 3.1). The typical laser path for 250 μm strut slices

shown in fig. 3.1(b) and (f) illustrates a 12% difference in energy input of neighbouring 'design identical' struts due to infill path planning. Additionally, scan spot placement between 'design identical' struts for both 150 µm and 350 µm show differences (Fig. 3.1(c) and (d)). These inconsistencies between identically designed struts are likely to result in manufacturing inhomogeneities within a uniform lattice design. In contrast, the unfilled scan, fig. 3.1 (a), shows consistent scan spots and path between adjacent struts (Fig. 3.1 (e)) for all diameters presenting a potentially more reliable method for lattice manufacture.

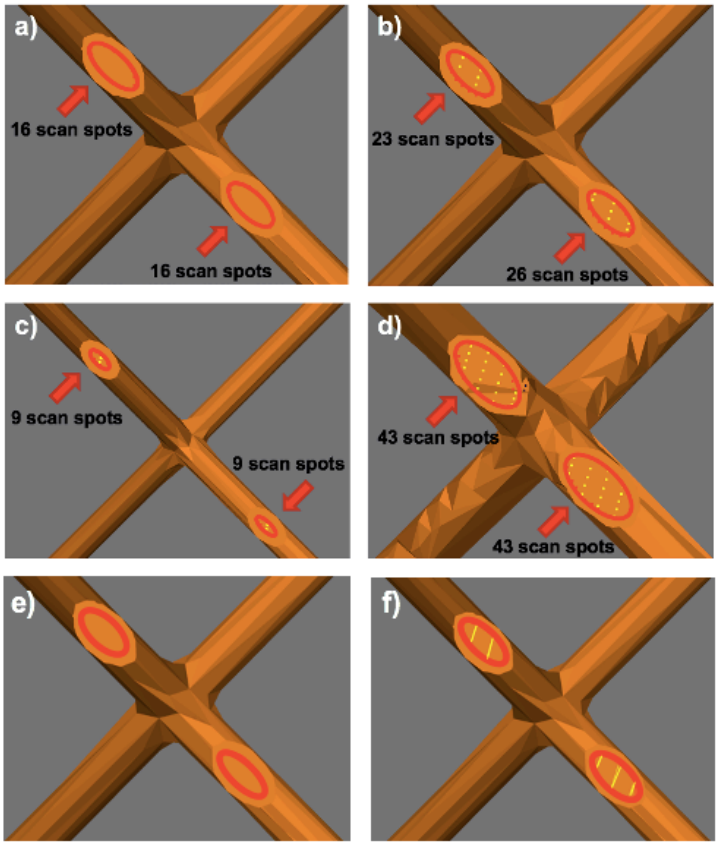

Figure 3.1 Images showing different number of scan spots in (a) SC and (b) SC+F strategies for designed struts size of 250 µm; (c) and (d) number of SC+F scan spots for 150 µm and 350 µm strut sizes; (e) scan path for SC scan; (f) scan path for SC+F. Red ellipsis represent border contours while yellow lines represent hatch (filling) scan.

In this paper, the accuracy of two scanning strategies, Single Contour (SC) (Fig. 3.1 (e)) and Single Contour plus Fill (SC+F) (Fig. 3.1 (f)), to manufacture PBF-LB Ti-6Al-4V metal lattices was compared. during the manufacturing . Critical parameters, laser power and scan speed, were varied and lattice reproducibility, and integrity evaluated to determine an optimal processing window. Herein SC is revealed as a novel processing method with the potential to improve lattice accuracy of AM medical devices.

3.2 Materials and Methods

3.2.1. Materials and Specimen manufacturing

Diamond unit cell lattices were selected for their adaptability in the biomedical field and manufacturability by PBF-LB as shown in multiple studies [165, 192-194]. All cuboidal designs measured 20 x 20 x 20 mm with 1 mm unit cell (Fig. 3.2 (a)). CAD geometry was generated using nTopology Element (nTopology Inc., 1.25.0) design software, and exported as standard tessellation files (*.stl). [195].

All specimens were fabricated using plasma atomised, Grade 23 Ti-6Al-4V powder (15 – 53 μm particle diameter) (LPW Technology Ltd., UK) via a RenAM 500 M (Renishaw, UK) PBF-LB system. The RenAM 500 M utilizes a modulated laser system whereby the laser operates point-wise for a fixed exposure time and point distance. Thus, scanning speed is defined as point distance/exposure time. Point distance was set at a constant 45 μm with scan speed varied using exposure time. All samples were produced under argon atmosphere using a pre-heated substrate at 170℃ and 30 μm layer thickness.

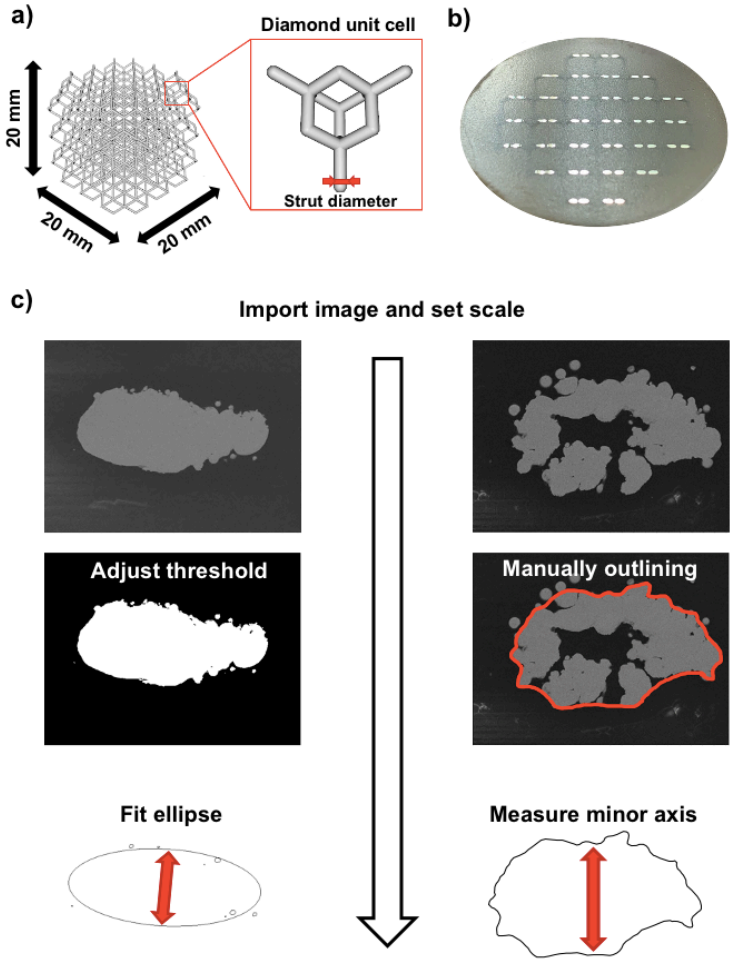

Figure 3.2 Images showing (a) the cuboidal and diamond unit cell design selected, (b) an example of cold-mounted and polished lattice and (c) a flow chart illustrating the contouring strategies used to measure strut diameter.

3.2.2 Design of Experiment

Two studies were performed. Within the first (Table 3.1), SC specimens were produced with varying laser powers (50-150 W), scanning speeds (750-2250 mm/s) and strut diameters (150 µm, 250 µm and 350 µm). SC+F specimens were manufactured for the midpoint conditions, using 100 W and 1125 mm/s.

Table 3.1 DoE for the comparison of SC and SC+F scan strategy.

Laser power (W)	Scan speed (mm/s)	Exposure time (s)	Energy density (J/mm)	Scan strategy
100	1125	40	0.089	SC+F
50	2250	20	0.022	SC
	1125	40	0.044	
	750	60	0.067	
100	2250	20	0.044	SC
	1125	40	0.089	
	750	60	0.133	
150	2250	20	0.067	SC
	1125	40	0.133	
	750	60	0.200	

The result of the first parametric analysis were used to develop a second study to better characterise the occurrence of porosity and dimensional accuracy (Table 3.2). These parameters were selected to improve the resolution of the process window near the boundary between porous/fully dense lattices and successful/failed lattices of 250 μm strut diameter structures.

Table 3.2 Parameters setting to evaluate the parametric effects on internal porosity of 250 μm lattice manufactured by SC.

Laser power (W)	Scan speed (mm/s)	Exposure time (s)	Energy density (J/mm)
50	1250	36	0.040
	1000	45	0.050
	750	60	0.067
70	1750	26	0.040
	1500	30	0.047
	1250	36	0.056
	1000	45	0.070
90	2250	20	0.040
	2100	21	0.043
	1750	26	0.051
	1500	30	0.060
	1250	36	0.072
	1000	45	0.090
100	2250	20	0.044
	1125	40	0.089
105	2250	20	0.047
	2100	21	0.050
	1750	26	0.060
	1500	30	0.070
	1250	36	0.084
115	2250	20	0.051
	2100	21	0.055
	1750	26	0.066
150	2250	20	0.067

3.2.3 Specimen Preparation

Fabricated specimens were cut from the build substrate by wire electrical discharge machining, cleaned in a water bath to remove excess powder, air dried, and cold-mounted

in resin (VersoCit-2 Powder, Struers Aps, Denmark). Samples were ground progressively from 220 to 4000 grit (Struers Aps, Denmark) With a final polishing performed using an activated Op-s suspension (Struers Aps, Denmark). Micrographs of 20 strut cross sections (Fig. 3.2 (b)) for each sample were captured using a Scanning Electronic Microscope (SEM, Hitachi TM3000, Japan) in backscattered mode.

3.2.4 Image Analysis and Process Mapping

Micrographs were analysed with ImageJ (NIH, USA., 1.53a) [196]. As shown in fig. 3.2 (c), strut contour was initially defined by an appropriate global threshold or via manual outline for fragmented sections. For both methods, the boundary included any internal pore areas. Individual struts within the lattice built at an angle of 54 resulting in an elliptical cross-section, thus, strut diameter was determined as the minor axis of a fit ellipse. Internal porosity was calculated as the total hollow area within struts divided by the total cross section area for all 20 struts in each sample. Process contour maps were plotted using MATLAB R2018b 9.5.0.944444 (MathWorks Inc. USA).

3.3 Results and Discussion

3.3.1 SC and SC+F comparison

Fig. 3.3 **(**a**)** compares mean strut thickness between SC and SC+F strategies for identical processing parameters (100 W, 1125 mm/s). SC+F strut diameter are on average 7% greater than those of SC for all sizes. Both SC and SC+F show a fully dense core for 150 μm and 250 μm struts, however greater diameters reveal the inability of the SC strategy to produce fully dense struts (Fig. 3.3 (b)) . This comparison demonstrates the

feasibility of using SC as a method for producing fully dense thin lattice struts below a certain diameter. Nevertheless, the obtained geometric accuracy is relatively low with errors of 3.5%, -12.6% and -7.4% for 150 µm, 250 µm and 350 µm, respectively.

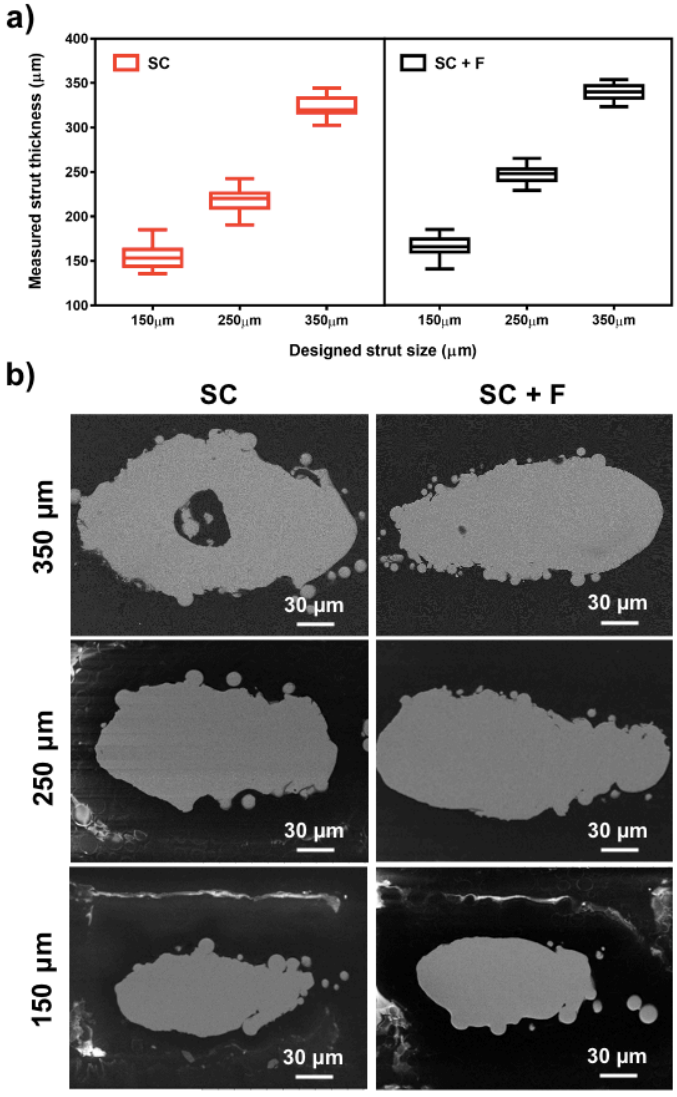

Figure 3.3 Comparison between SC and SC+F scan strategy under same processing parameters (laser power 100 W, scan speed 1125 mm/s): (a) strut thickness range for designed value of 150 µm, 250 µm and 350 µm; (b) SEM images showing different internal morphology under three designed strut thickness.

Previous studies have demonstrated that energy input influences melt pool width, directly relating it to strut thickness regardless of scan strategy used [190, 191]. SC+F produces greater energy input per strut than SC, even showing different energy input for adjacent struts; as illustrated in fig. 3.1 (b), (c), and (d). The relatively limited conductive heat flow afforded by thin lattice struts results in a local thermal build-up during laser exposure whereby surplus energy simply drives up the melt pool width. In this scenario, final strut diameter is disproportionately driven by energy input as illustrated in the 150 μm struts where mean strut thicknesses are 155.2 μm and 165.7 μm for SC and SC+F respectively. Additionally, the previously highlighted differences in energy input between adjacent struts for the SC+F scan strategy are likely to induce further geometric inconsistencies. A similar phenomena was reported by Rashid et al. comparing single and double hatch scan [197] with thicker struts manufactured by double hatch scan due to the increase in energy input on each layer compared to single hatch scan. It should be noted however that the potential advantages of SC lattice production are limited by strut diameter. Above a threshold diameter, energy input and corresponding melt pool width become insufficient to produce a fully dense strut and internal porosity remains following processing as highlighted in the 350 μm SC sample in fig. 3.3 (b). Thus, it is clear that it is necessary to analyse the processing window of this scan strategy.

Processing maps indicating strut condition of lattices produced using SC are shown in Fig. 3.4 (a)-(c). For the 150 μm strut diameter lattices, most parameters produced a fully dense material, nevertheless, manufacturing failed for 50 W, 1125 mm/s and 2250 mm/s due to insufficient energy input to form a stable structure (Fig. 3.4 (a)). Occurrence of internal porosity increased with strut diameter as revealed by the shift in solid core areas

observed in 250 μm samples (Fig. 3.4 (b)) and 350 μm samples (Fig. 3.4 (c)). Corresponding pore fraction by cross-section area also increased with strut diameter from ~1.6% to ~27.3% for 250 μm and 350 μm lattice respectively (Figure 3.4 (b) and 3.4 (c) insets). Likewise, the occurrence of porosity decreases with increasing energy density as demonstrated in the 350 μm specimens (Fig. 3.4 (c)) where the only fully dense struts occurred under greatest energy density (150 W and 750 mm/s – 1125 mm/s). This highlights that internal morphology of SC manufactured lattices is highly dependent on both strut thickness and processing parameters.

A strong linear relationship ($R^2 = 0.97$) between the energy density and resulting lattice strut diameter for each design strut thickness is shown in fig. 3.4 (d). This further confirms that, at these scales, process parameters as much as laser path govern the resulting geometry and careful control is essential for accurate lattice production. Single point exposure investigations have previously yielded positive results for lattice production showing the link between energy input and strut diameter [172, 191, 198]. The SC strategy builds on this combining the control of both laser path and melt pool size via process parameter optimisation but eliminating the inconsistencies brought by hatch-filling.

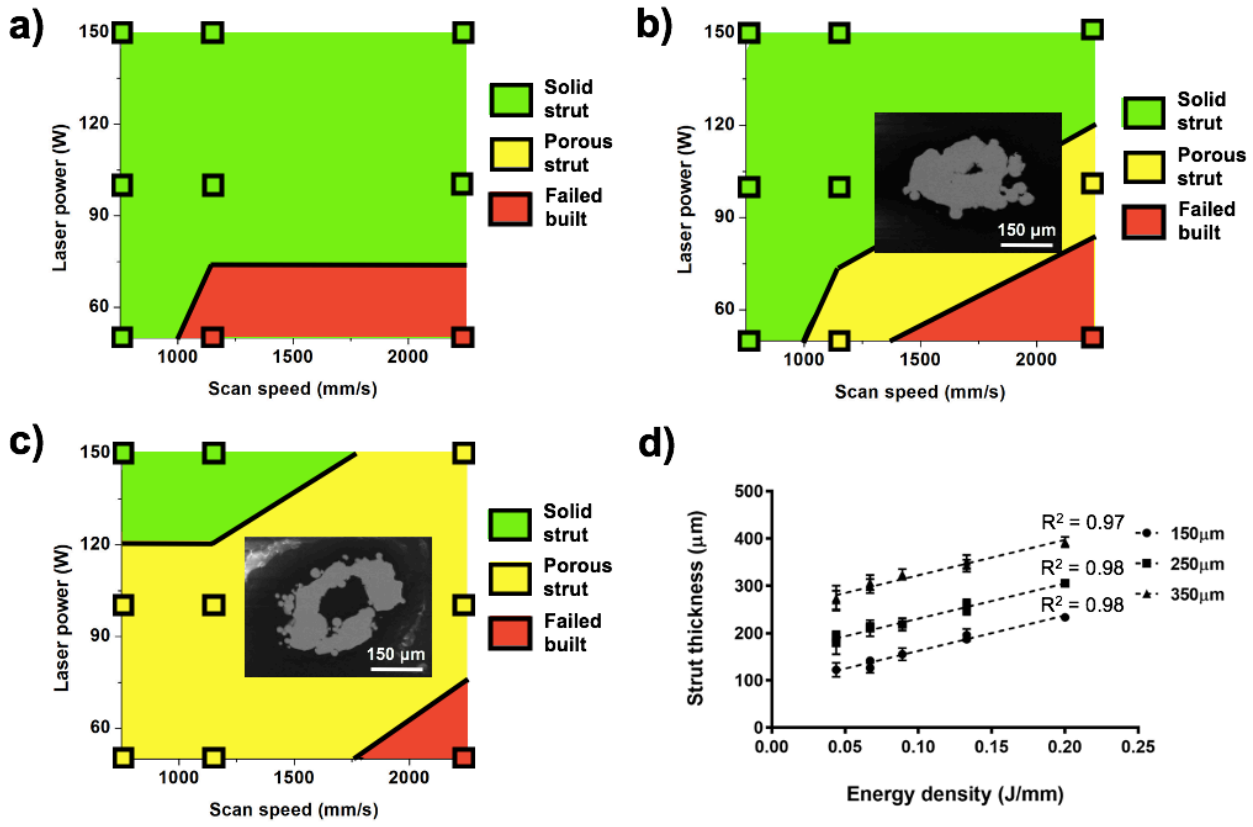

Figure 3.4 Parametric maps for strut thickness of (a) 150 µm, (b) 250 µm and (c) 350 µm, (a)-(c), where green areas represent struts built with solid core, yellow areas struts built with hollow structures and red areas unsuccessful built with SEM details showing the variation of hole area; and (d) correlation between energy density and strut thickness.

Other research has confirmed that increasing ED raises melt pool width [187] which can be used to control the final strut diameter for a given SC laser path. To produce fully dense struts however, the melt pool width, and in turn the ED, should be sufficient to melt the centre of each strut for a given laser path. A simplified geometric interpretation suggests that the smallest melt pool diameter needed to produce a fully dense strut is equal to the diameter of the laser path. This would produce a strut of diameter equal to approximately twice that of the melt pool. This relationship combined with process mapping may allow the input parameters themselves to act as the fine control for predictable geometric accuracy and strut integrity of SC processed lattices.

3.3.2 Processing window of SC manufactured samples

To improve and investigate the accuracy of this process mapping method, a further study was carried out using 250 μm strut diameter SC lattices. Process parameters near the solid/porous boundary were selected to accurately map this interface (Fig. 3.5 (a)). Internal porosity was revealed to be highly dependent on the ED (Fig. 3.5 (b)), with hollow regions occupying 1.18% to 2.51% of the total area for values below 0.056 J/mm. As energy density increased from 0.056 J/mm to 0.089 J/mm, the corresponding porosity decreased, with fully dense struts obtained where energy density was greater than 0.089 J/mm. Significant porosity was observed under low laser powers and high scan speeds (Fig. 3.5 (c)). This results from the limited energy transferred, either due to low input energy overall or the brief laser/bed interaction time, reducing melt pool diameter. Nevertheless, there was no direct correlation between porosity and either laser power or scanning speed, suggesting a combination of both parameters as the main driver of the observed trends (Fig**.** 3.5 (c)).

This expanded study reveals that the relationship between ED and accuracy follows a convex unimodal trend with the minimum located at ~0.1 J/mm, resulting in standard error below 0.1% and fully dense struts (Fig. 3.5 (d)). Furthermore, discrepancy between design and actual strut diameter is minimised at 0.1 J/mm (150 W, 1500 mm/s). It is worth mentioning the fully dense struts were produced up to the maximum energy density, 0.2 J/mm (Fig. 3.4 (b)), indicating that careful selection and control of energy density, via

scan speed and laser power, can be used to effectively manufacture lattices with SC strategy.

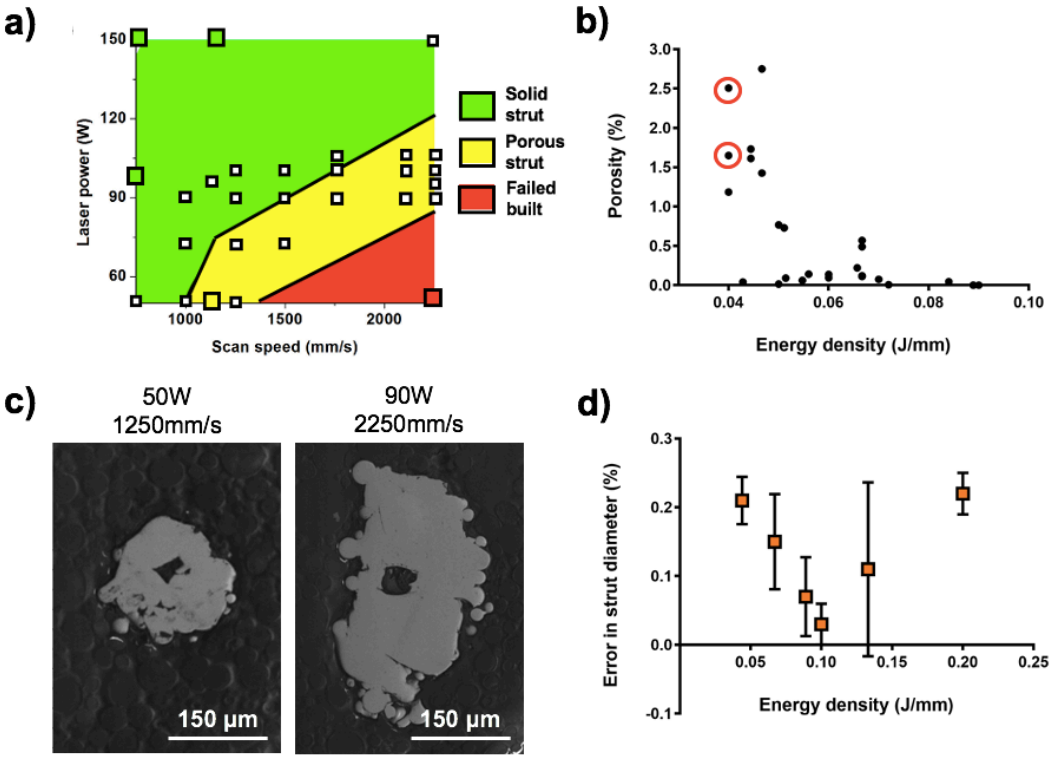

Figure 3.5 Images showing (a) parameters selection (white cubic dots), (b) influence of energy density on internal porosity; (c) SEM micrographs presenting the internal porosity of the two red circled parameters in (a) and (b), respectively and (d) plot demonstrating the strut size error (%) as a result of energy density variations.

Data from both studies can be combined to form a 250 µm process map of both strut diameter and porosity (Fig. 3.6). The relationship between strut diameter and laser power (W) and scan speed (mm/s) can be fitted to a plane (Fig. 3.6 (a)) with a standard error of estimate, σ_{est}, of 13.8 µm (R^2 = 0.77) which is reasonable given the method of measurement and irregularity of strut cross section in some cases. The plane has the equation:

*Strut Diameter (µm) = 0.8423*Power (W) – 0.0326 Speed (mm/s) + 190.4728* (3.2)

Isolines derived from this planar fit are shown super-imposed over the contour plot of porosity in fig. 3.6 (b) to form a process map. Fully dense (yellow) regions can easily be seen alongside the corresponding expected strut diameter for the 250 µm design condition. Maps of this form could be produced to parametrically adjust strut geometry when using the SC strategy.

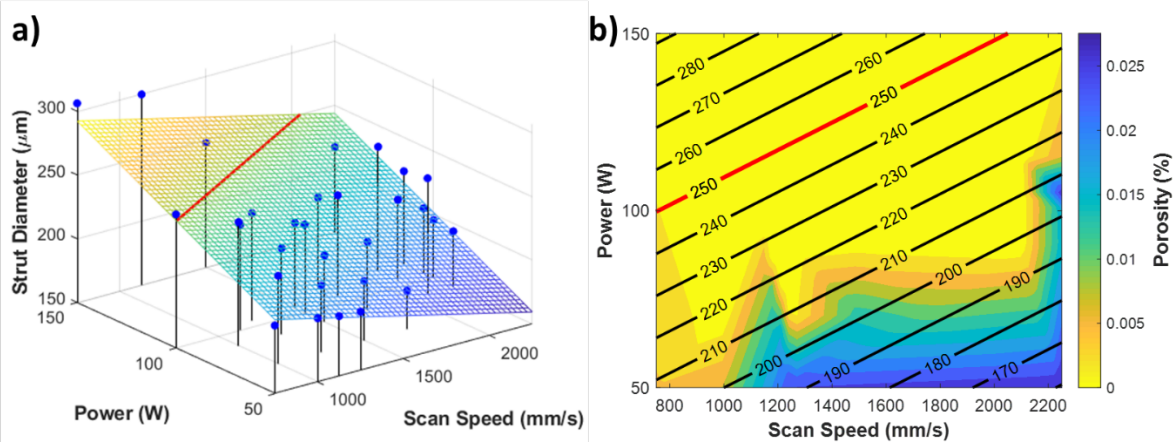

Figure 3.6 Process map for the combined data of both studies. (a) 3D scatter plot showing strut diameter vs laser power (W) and scan speed (mm/s) with target 250 µm condition shown by red line. (b) Process map displaying both strut diameter (labelled contour lines) and porosity (colour map) with laser power (W) and scan speed (mm/s) with target 250 µm strut diameter highlighted in red.

3.3.3 Wider Biomedical Implications

This study has highlighted how process parameters and laser scan strategy combine with the design to form the manufactured geometry for fine lattice structures. Understanding and control of these inputs will be critical in the translation of devices incorporating lattices from research to clinical use. Previous studies have shown how lattice density [199, 200] and strut diameter [201] influence mechanical properties; how pore size influences cell proliferation [164, 165]; and how relative density can govern MRI artefacts [202], or novel drug delivery [169]. All of these novel functionalities rely on

accurate, reproducible, and robust methods of lattice manufacture to ensure the closest possible alignment of design and manufactured geometry.

By constructing process maps similar to those presented, it is possible to gain confidence that lattices will be produced 'first-time-right' when integrated into larger implants. Likewise, the SC scanning strategy aims to reduce uncontrolled variability introduced at the slicing stage. Both of these aspects will be critical, from both a patient welfare and regulatory perspective, to ensure that devices perform as intended when implanted.

3.4 Conclusions

In this work, the capability of SC to manufacture lattice structures with thin struts of diameter less than 350 μm has been demonstrated. Two studies have highlighted relationships between strut density and geometric accuracy showing the potential for fine control of lattice manufacture via parametric adjustment alongside the limit of such approach. Linear energy density is suggested as a practical indicator of the process, from which both the accuracy and internal morphology of lattice struts could be predicted and optimised. The process maps generated may be used in future lattice production as a practical method for structural control. It is hoped that the use of SC processes lattice will improve geometric consistency critical for the full exploitation of AM lattices in medical devices.

Chapter 4 IMPROVING PREDICTABILITY OF LATTICES FOR BIOMEDICAL DEVICES: A PARAMETRIC AND STRUTS ANGLE STUDY

Abstract

The advancement of metal additive manufacturing has recently enabled the integration of porous lattice regions into orthopaedic devices. These open structures have been shown to support osseointegration; however, the intricate struts are challenging to reliably fabricate at full density. Despite the increased utilisation of these metamaterials there remains limited understanding of how to optimise laser process specifically for these geometries. PBF-LB of representative single struts is focused on this study from the perspective of surface properties, mechanical performance, and in-vitro biological response.

Specifically, the influence of laser power (100 – 200 W) and speed (2250 – 900 mm/s) and struts angle 20˚ - 90˚ for a 250 µm strut diameter was explored. Struts built below 45˚ to the substrate using optimal laser parameters (150 W and 1125 mm/s) were found to exhibit a surface topography that facilitated the highest level of cell adhesion (84.3

cells/mm^2) after 24 hrs ($p \leq 0.001$). To support this finding, a novel image analysis method was developed to characterise the average roughness across the complete strut profile. An opposite trend was observed for mechanical strength with struts built at above 45˚ reaching a load of 3510 MPa without failure. Minimal manufacturing defects (<0.04%) were observed for struts built at all angles using a linear energy density of 0.13 J/mm. These findings were brought together in a parameter design map was to guide stakeholders in producing customised biomedical devices, enabling control of key physiochemical properties with the aim of maximising osseointegration.

ACKNOWLEDGEMENT OF CONTRIBUTING MATERIAL AND AUTHORS

Content within this chapter has been published in the following journal paper(s):

- X. Cao, L.N. Carter, K. Man, V.M. Villapún, L. Giangiorgi, S.C. Cox, Improving predictability of additively manufactured Ti-6Al-4 V lattices for orthopaedic devices: A parametric and struts angle study, Materials & Design 243 (2024).

As primary author, X Cao produced all written work within this publication and performed primary experimental work. The contributions of co-authors are as follows:

- Dr. L N Carter: Conceptulisation, Supervision, MATLAB coding
- Dr. K. Man: *In-vitro* experiment, Editing
- Dr. V M Villapun and L Giangiorgi: MATLAB coding
- Dr. Sophie Cox: Editing, supervision

4.1 Introduction

It has been reported that the selection of PBF-LB process parameters affects the final quality of lattices. This is especially important for lattices used in medical devices where geometric accuracy and surface finish directly influence performance [203]. Varying key process parameters, namely, laser power and scanning speed, has been found to influence formation of defects within lattices, including keyhole and gas porosity, lack of fusion defects, and balling behaviour [81]. Process parameters were also shown to strongly influence surface quality of PBF-LB components, particularly in down-facing regions, where greater energy input drove formation of a larger melt pool resulting in a poorer surface due to increased particle adhesion, entrapment, and sintering [108]. Likewise, inappropriate process parameters impact manufacturing accuracy, leading to oversized/undersized and irregular struts [102]. These geometric inaccuracies have been shown to negatively influence mechanical performance including deformation behaviour and failure mode [204]. Wang et al. found that scan speed plays a key role in the transformation of grain shape of Ti64 microstructure due to altered thermal history [205], while Ahmadi et al. concluded that the effect of process parameters is not significant to the grain size and shape of Ti64 lattices [206]. Collectively, properties such as surface finish and manufacturing accuracy varied with process parameters together bring challenges to the predictability of lattice production.

Alongside process parameters, the effect of strut angle on surface finish and manufacturing defects (internal pores), which influences mechanical performance, have

been found [207]. This strut angle refers to the build/inclined angle of lattice struts, which is a key factor of the build preparation or lattice design. Due to the PBF-LB process is a thermal-based technology, the effect of strut angle on AMed component is reflected via the difference of heat conduction between powder material and solidified part. The extent of overlap for adjacent layers is influenced by strut angle, resulting in the varied area of the present layer that is interacted with powder or solidified material. These would influence the lattice quality and properties via influencing manufacturing accuracy, surface finish and porosity content [208]. Therefore, the outcome suggests the importance of exploring the effects of strut angle on the PBF-LB lattice properties to figure out the underlying relationship and correlations, further enhancing the process predictability and lattice geometric design.

Meyer et al. reported a parametric dependency of strut with varied angle for the metal lattice struts with thickness of 300 m, where two parameters set with ED of 2.0 J/mm^2 and 4.2 J/mm^2 present that lattice thin struts could be manufactured with limit angle of 15˚ and 8˚ [209]. Besides the effect of strut angle and process parameters on manufacturability of PBF-LB lattice strut, the effect on geometric accuracy and surface finish could not be ignored. Murchio et al. manufactured Ti64 strut with junction via PBF-LB, it was found that the 90˚ struts (639 ± 11 µm) exhibit lower thickness than the designed size (670 µm), while the thickness of 0˚ (745 ± 19 µm), 15˚ (739 ± 18 µm) and 45˚ (713 ± 7 µm) built struts increased than the nominal value [210]. Suard et al. investigated the effects of build orientation on Ti64 cylindrical parts, no obvious difference of surface finish was observed on vertical struts. However, higher roughness was shown on lower-angle struts due to overheating and larger powder facing area. These

difference in surface quality would further impact the mechanical properties as described below [211].

Changing deformation and failure behaviour between lattices consisted of different strut angles were observed by Mazur et al., with failure occurring mostly in struts built in the diagonal and vertical angle, with bending and buckling behaviour in lattices [212]. Both Murchio et al. and Hossain et al. studied the strut angle effect on tensile properties, the former concluded that build angle of struts has no obvious regularity on tensile properties, the latter found that there is an increasing trend of ultimate tensile strength as a function of struts angle [207, 213]. These imply the importance to analyse, calculate, and control the local stress and strain of lattices. There has also been work demonstrating that the differences in surface topography of surfaces built at different angles may significantly alter osteoblast and bacterial attachment [131]. In summary, limited work brings together the influence of both process parameters and strut angle on key success criteria for utilisation in medical devices, including surface quality, mechanical performance, and biological response. With this in mind, our objective is to understand the effect of process parameters and struts angle on fundamental properties of lattice element that drive these performance criteria. While it may be challenging to balances these criteria for orthopaedic device performance ultimately moving in this direction will improve predictability and quality.

Herein, we have conducted a robust assessment of the effects that PBF-LB process parameters and struts angle on surface roughness, three-point bending properties, and mammalian cell response. To enable these fundamental relationships to be broadly

utilised by the field we have developed a map to guide the design of lattices for tissue regeneration. Overall, the final output enables further control, prediction, and improvement of implantable lattice fabrication within customised biomedical devices applied in bone replacement, maxillofacial, craniofacial, dental implants etc.

4.2 Materials and Methods

4.2.1 Specimen manufacturing

A strut diameter of 250 µm was selected as being representative of lattices used in orthopaedic devices and used throughout this study [214]. 10 mm long single struts at build angles of 20˚, 45˚, 70˚ and 90˚ to the substrate plate were designed in nTopology (version 3.35.2, nTopology Inc., USA) and exported as standard tessellation files (.stl). To avoid damage during the de-build process, specimens were built within a thin protective wall structure (Fig. 4.1 (a)). Plasma atomised Ti-6Al-4V (Grade 23) powder feedstock with a size range of 15-53 µm was used to manufacture all samples with a RenAM 500S (Renishaw, UK). Duplicates (n=10) were prepared for each group with varying laser power and scanning speed (defined as point distance/exposure time for the point-wise scanning of RenAM 500S system) (Table 4.1). Linear energy density (LED) is calculated from laser power divided by scanning speed to indicate the energy input during manufacturing. Point distance of 45 µm, layer thickness of 30 µm and single contour were constant for all manufactured samples. All specimens were built under an argon atmosphere and on a Ti64 substrate pre-heated to 170°C. Following manufacture, parts were manually removed while maintaining a final length for all struts of 7 mm.

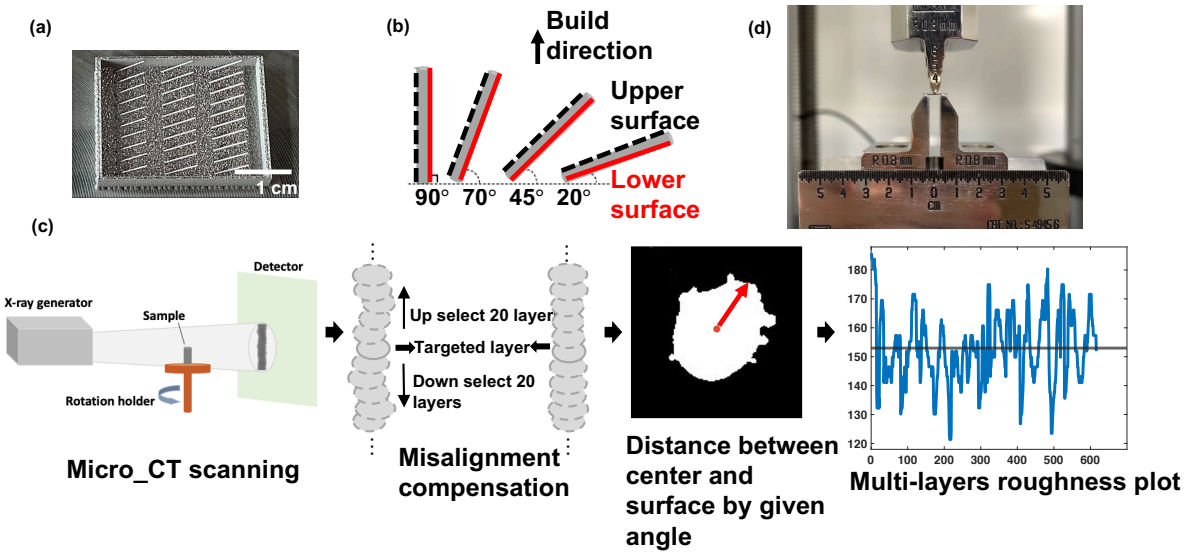

Figure 4.1 (a) Image showing the as-built single struts within the protective wall structure; (b) diagram defining the struts angle, upper surface (black-dash marked) and lower surface (red marked); (c) flow diagram displaying the main steps to calculate average roughness of whole strut profile through micro-computed tomography (CT) and MATLAB image analysis, and (d) image to illustrate the set up and the beginning position of 3-point bending test.

Table 4.1 Design summary of build angles and parameters used in this study.

Strut build angle (˚)	Laser power (W)	Exposure time (s)	Scan speed (mm/s)	LED (J/mm)
20	100	20	2250	0.04
	150	40	1125	0.13
	200	50	900	0.22
45	100	20	2250	0.04
	150	40	1125	0.13
	200	50	900	0.22
70	100	20	2250	0.04
	150	40	1125	0.13
	200	50	900	0.22
90	100	20	2250	0.04
	150	40	1125	0.13
	200	50	900	0.22

4.2.2 Roughness measurement

As-fabricated struts were marked before removing from the plate for roughness measuring of specific interested upper and lower surfaces (Fig. 4.1 (b)). Images were captured vertically to the sample surface using an optical profilometer (Alicona Infinite Focus G5, Austria) with a 20× lens. Three areas from the up- and down-faces of each strut were scanned with average roughness (R_a) obtained with a cut-off wavelength of 2.5 mm as per ISO 4288-1996.

4.2.3 Micro-CT characterisation

A CT system (Skyscan 1172 Bruker, Belgium) was used to investigate the 3D volume of struts. Scans were obtained using a voltage of 80 kV, current of 100 mA, exposure time of 1600 ms, a 0.5 mm aluminium filter, pixel size of 2.44 μm, camera resolution of 2664 × 1120, rotation step of 1.12˚ and a frame averaging of 6. Cross sections were produced after reconstruction in NRecon (version 1.7.1, Bruker), by which the internal defects generated in the PBF-LB process were detected and exhibited in 3D geometries. Strut thickness was measured and averaged by importing the reconstructed images to ImageJ for further calculation of mechanical properties.

An image analysis method in fig. 4.1 (c) was developed to calculate average roughness (R_a) from the complete strut profile captured by CT. A threshold of 70 was firstly determined in ImageJ [215] from the reconstructed images by NRecon (version 1.7.1, Bruker) to highlight the solid material. Binary images were then imported to MATLAB (Version R2021b, U.S.A.) and a global threshold of 70 applied. If the pixel grey value was greater than the threshold value, the pixel would be counted to identify the struts

solid area, after which the centre of each slice would be located individually by calculating the midpoint of coordinates meeting the condition of threshold over 70. A simple moving average function was used to remove the deviation of eccentricity that may be caused by either poor vertical alignment in the scanner, or overall bends or curvature to the strut. Thus, the current layer was aligned by averaging the centre coordinates for 20 slices forward and backward, respectively. Next, the last pixel within threshold range would be located along the chosen MATLAB angle. By multiplying the given pixel size from CT scanning with the number of pixels counted, distance between struts centre and the border were measured and the above steps would be repeated for chosen successive slices to generate the struts profile. At each specific measuring angle, the base line was calculated from the mean value of the measured profile and subtracted to compute the roughness profile, following by R_a calculation as stated in Eq. 4.1. The overall roughness of each single strut contour was attained by varying the MATLAB measuring angle through 0˚ to 350˚ with a 10 interval.

$$R_a = \frac{1}{n}\sum_{i=1}^{n} |y_i| \tag{4.1}$$

Where:

n = number of data points in the sampling length

y_i = absolute value of the difference between the actual height at that point and the mean height of the sampling length

4.2.4 Three-Point bending test

Considering the simplicity and adaptivity of specimen preparation and testing, as well as the interests to complex loading mechanism of compression, tension and shearing in lattices, 3-point bending test was conducted on a universal testing machine (Instron 5848,

USA) at room temperature, using a 2 kN load-cell [216]. Span length was fixed at 4 mm, displacement rate was set at 0.5 mm/min for all measurements compliant with ASTM E290 (Fig. 4.1 (d)). Bending continued until failure or if a maximum deformation of 2 mm was reached with independent tests performed on each condition per triplicate. Elastic modulus and maximum flexural strength (MFS) were calculated based on Eq. 4.2 and Eq. 4.3 [217].

$$E_f = \frac{F}{\delta} \cdot \frac{L_{total}^3}{48I} \tag{4.2}$$

Where:

F = applied external load, N

L_{total} = span length or distance between the supporting pins, mm

δ = deformation, mm

I = polar moment of inertia, calculated from measured diameter, mm^4

$$\sigma_f = \frac{F_{max} L_{total}}{4W} \tag{4.3}$$

Where:

F_{max} = applied external load at failure, N

L_{total} = span length or distance between the supporting pins, mm

W = section modulus, calculated from measured diameter, mm^3

Average strut diameter used in the equation were obtained from the CT reconstructed cross-section area. To acquire a thorough understanding of the failure point, images of the fracture cross-sections were taken with a scanning electron microscope (SEM, Hitachi 3030, Japan).

4.2.5 In-vitro analysis of osteoblast behaviour on single strut samples

4.2.5.1 Cell culture

20˚, 45˚ and 70˚ struts with the LED of 0.13 J/mm were chosen to evaluate the osteoblast cell response. MC3T3 murine pre-osteoblasts were purchased from American Type Culture Collection (ATCC, United Kingdom). Basal culture media consisted of minimal essential medium (α-MEM; Sigma-Aldrich, United Kingdom) supplemented with 10% Foetal Bovine Serum, 1% penicillin/streptomycin (Sigma-Aldrich, United Kingdom) and L-glutamine (Sigma-Aldrich, United Kingdom). Mineralisation medium was prepared by supplementing basal culture media with 10 mM β-glycerophosphate (Sigma-Aldrich, United Kingdom) and 50 μg/mL L-ascorbic acid (Sigma-Aldrich, United Kingdom).

The struts were sterilised in 70% ethanol for 24 hours, then washed three times with sterile phosphate buffered saline (PBS, Lonza, United Kingdom) prior to use. For cell seeding, MC3T3s were initially incubated with the CellTracker^{TM} Green CMFDA (2 μM, Thermo Scientific, United Kingdom) for 30 min in the dark. Following staining, cells were trypsinised and dynamically seeded onto the struts as previously described. Briefly, cell suspension containing 2 x 10^5 cells were transferred into a sterile 2 ml Eppendorf tube with a hole pierced in the lid. The sterile struts were placed into each tube and the Eppendorf tube sealed with an AeraSeal™ film membrane (Sigma-Aldrich, United Kingdom). The samples were then loaded onto an SB tube rotator (SB3, STUART, United Kingdom) and dynamically cultured for 16 h at 8 rpm (37°C, 5% CO_2). The next day, the samples were washed twice with basal medium, then cell adhesion was assessed under an EVOS fluorescent inverted microscope (EVOS M5000, Invitrogen, USA) where the number of cells were quantified. Samples were then incubated in osteogenic media for 21

days with media replaced every two days. After 21 days of culture, cell viability was assessed by live/dead staining. Samples were incubated with basal medium supplemented with CellTracker™ Green CMFDA (2 μM, Thermo Scientific, United Kingdom) and Propidium iodide (1 μg/ml in PBS, Sigma-Aldrich, United Kingdom) for 30 min in the dark. Samples were washed twice with basal medium, then visualised under an EVOS fluorescent inverted microscope (EVOS M5000, Invitrogen, USA).

4.2.5.2 Alkaline Phosphatase (ALP) Activity

ALP activity was determined using the 4-nitrophenyl colourimetric phosphate liquid assay (pNPP, Sigma-Aldrich, United Kingdom) as previously described. Briefly, 10 μL of cell lysate (in 0.1% Triton™ X-100) was added to 90 μL of pNPP and incubated for 60 min at 37°C. The absorbance at 405 nm was read on a SPARK spectrophotometer (TECAN, Switzerland). ALP specific activity (ALPSA) of each sample was calculated using total ALP quantity divided by total DNA content (nM ALP/hr/μg DNA) [218].

4.2.5.3 DNA Quantification

DNA content was quantified by the Quant-iT PicoGreen DNA assay (Invitrogen, Life Technologies, United Kingdom). 10 μL of cell lysate (in 0.1% Triton™ X-100) was added to 90 μL of TE (10 mM Tris-HCl, 1 mM EDTA) buffer. 100 μL of PicoGreen reagent was added to all samples for 5 min. The fluorescence was then measured in a SPARK spectrophotometer (TECAN, Switzerland) at 480/520 nm wavelength.

4.2.5.4 Collagen Production

Collagen deposition was evaluated with picrosirius red staining. Samples were washed twice in PBS and fixed in 10% neutral buffered formalin (NBF, Cellpath, United Kingdom) for 30 min, prior to staining with Picro-Sirius Red Solution (ScyTek Laboratories, Inc., USA) for 1 h. The unbound dye was removed by washing in 0.5 M acetic acid followed by distilled water and left to air dry. To quantify collagen staining, 0.5 M sodium hydroxide was used to elute the bound dye and absorbance read at 590 nm using a SPARK spectrophotometer (TECAN, Switzerland). Collagen production was normalised with DNA content.

4.2.5.5 Calcium Deposition

Alizarin red staining was conducted to evaluate calcium deposition. Briefly, cells were washed twice in PBS and fixed in 10% NBF (Cellpath, United Kingdom) for 30 min. Following fixation, cells were washed in distilled water and then incubated with alizarin red solution (Sigma-Aldrich, United Kingdom) for 10 min. The unbound dye was removed by washing in distilled water. For alizarin red quantification, stained samples were eluted with 10% cetylpyridinium chloride (Sigma-Aldrich, United Kingdom) for 1 h and then absorbance read at 550 nm using the SPARK spectrophotometer (TECAN, Switzerland). Calcium content was normalised with DNA content.

4.2.6 Statistics

All statistical analysis was conducted using Prism (GraphPad Software, version 9.0.0, USA). Two-way ANOVA was performed followed by Tukey's post-hoc to reveal the effects of process parameters and build angles on Ti64 struts. Alpha level was 0.05, p

values lower than or equal to which were deemed significant. *P < 0.05, **P < 0.01, ***P < 0.001, ****P < 0.0001. Results are shown as average standard deviation.

4.3 Results

4.3.1 Effect of process parameters and struts angle on geometric defects

The total porosity was calculated by estimating the area of open pores connected to the strut surface and closed pores which are enclosed by solid material, both of which were captured by CT (Fig. 4.2). Specimens built at the lowest LED of 0.04 J/mm were largely hollow showing a significant lack of fusion in their core that seems to decrease as the strut angle increases with the total porosity of samples built at 20˚ and 45˚ greater than the 70˚ and 90˚ struts. Spheroidization could be observed at the surface and inter-layers of the struts which may be caused due to balling during manufacturing. As the LED increases, the porosity rapidly decreases with struts manufactured using a LED of 0.13 J/mm fully melted, ~ 0.02%, across all strut angles. Further increases in LED, 0.22 J/mm, revealed struts dominated by isolated closed pores, shown as gas pores or keyholes, especially noticeable in 90˚ struts that showed 2.21% porosity compared with those built at 70˚ and lower where porosity remained below 1%.

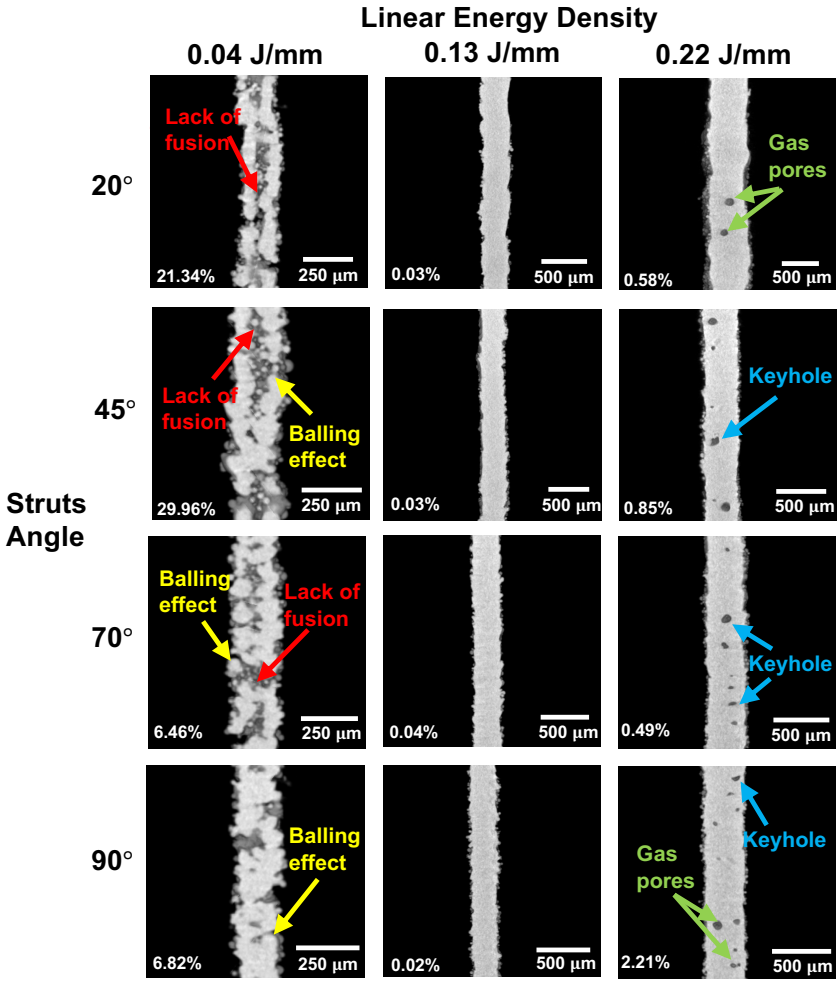

Figure 4.2 Images showing inner morphology of struts scanned by µCT, where defects are indicated by arrows for lack of fusion, balling effect, gas pores and keyholes, total porosity is shown at the bottom left of each image.

4.3.2 Effect of process parameters and struts angle on average roughness

Average roughness R_a of upper and lower areas of the strut was shown to be influenced differently by process parameters and struts angle (Fig. 4.3). The upper surface shows a general decrease in roughness with increased LED for all angles considered, albeit only significantly different for the 20 sample ($p < 0.01$) (Fig. 4.3 (a)). As presented in fig. 4.3 (b), the upper R_a for struts produced at 0.13 J/mm and 0.22 J/mm for 20(9.5 ± 1.6 µm and 10.4 ± 2.0 µm) was shown to be smoother than the struts of 0.04 J/mm (19.4 ± 4.2 µm). These surfaces also seem to be affected by lower struts angle resulting in rougher

surfaces than struts 45˚. On the other hand, the lower areas of the struts appear to raise their average roughness with increased energy density for struts 45˚. Similarly, to the upper surfaces, it should be noticed that the R_a of struts angle of 20˚ was significantly greater than those above 45˚ at LED of 0.22 J/mm (Fig. 4.3 (a)). The lower surface of 20˚ struts were largely covered by partially melted powder with wavier surfaces observed as the LED increases in Fig. 4.3 (b), opposite to the upper surfaces while struts processed under the same LED.

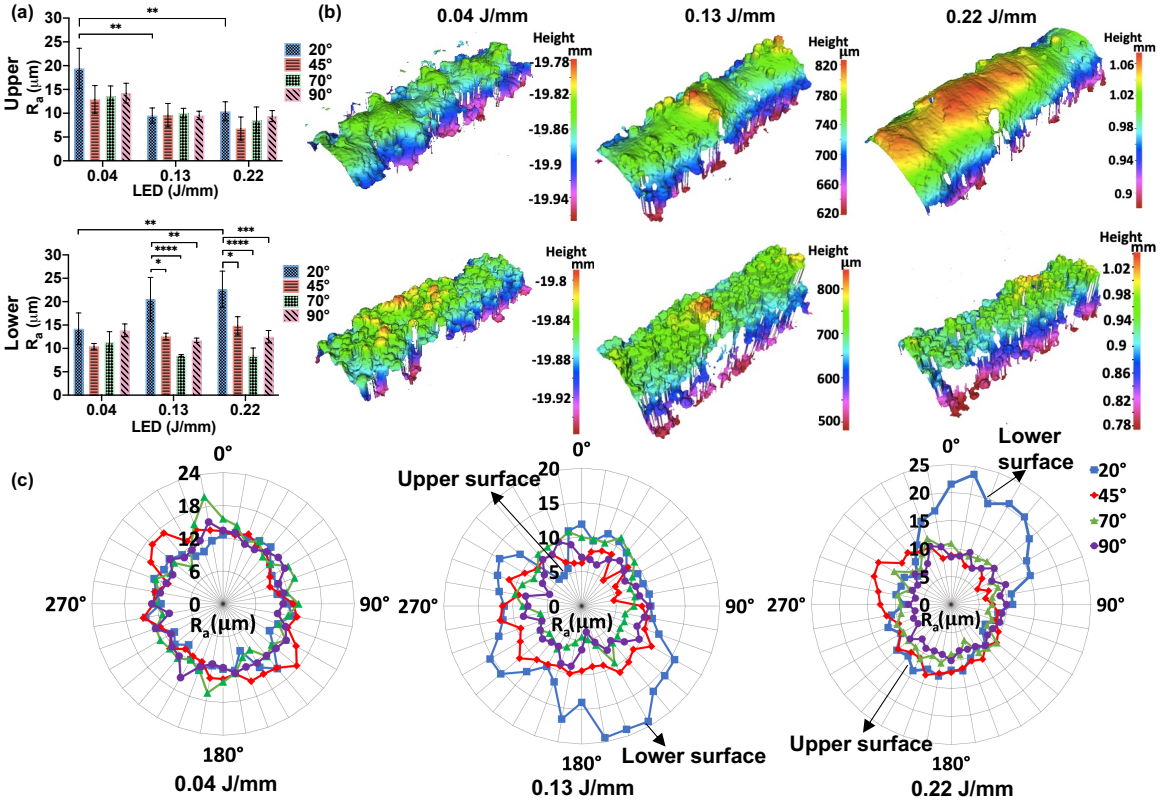

Figure 4.3 Plot showing the build angles and process parameters effects on (a) upper and lower surface of struts; (b) 3D maps presenting the upper and lower surface of 20˚ struts built with 0.04 J/mm, 0.13 J/mm, and 0.22 J/mm energy densities; (c) radar figures showing whole profile of R_a, plotted against measured angle in MATLAB for single strut built with different LED, as well as showing recognizable upper and lower area of 20˚.

The R_a obtained through image analysis in fig. 4.3 (c), reveals values between 10 μm and 15 μm, for strut angles above 45˚ which are in line with the measurements observed with optical profilometry fig. 4.3 (a). Similarly, the R_a of 20˚ drastically increased as the LED was risen for the lower surface, which agrees with the R_a measurements. Roughness appears to be more uniform for strut angles above 45˚, while as LED increases, the R_a map of 20˚ struts tend to be more elliptic. Notably, for struts manufactured by 0.13 J/mm, R_a reached the lowest value of 9.0 ±1.9 μm for 45˚, 7.9 ± 1.8 μm for 70˚, and 7.6 ± 1.4 μm of 90˚.

4.3.3 Effect of process parameters and struts angle on mechanical properties

In fig. 4.4 (a) and (b), there is a general increase in maximum flexural strength (MFS) and elastic modulus as the LED increases from 0.04 J/mm to 0.13 J/mm. Further increase in LED only improved the mechanical properties of the 20˚ strut with 45˚ and 70˚ remaining largely unchanged and 90˚ displaying a slight reduction. These properties seem to display trends highly correlated with the build angle, with positive relationships apparent for lower LED, 0.04 J/mm, negative arising for the higher LED studied, 0.22 J/mm, and stagnation at 0.13 J/mm.

Fig. 4.4 (c-f) shows typical stress-strain curves of the 3-point bending tests on struts; firstly, a linear region of elastic gradient, secondly a region of plastic deformation following the yield point, and finally an irregular region prior to failure. For struts built at 0.04 J/mm, all failed immediately after reaching the MFS (Fig. 4.4 (c)) while, as the LED increased to 0.13 J/mm, struts above 45˚ showed a smooth plateau region until

achieving a 2 mm deformation suggesting a more ductile behaviour (Fig. 4.4 (d)). For the 0.22 J/mm struts, two different phenomena were observed. Those above 45˚ either experienced a direct failure after MFS (Fig. 4.4 (e)) or entered a non-failure plateau region (Fig. 4.4 (f)).

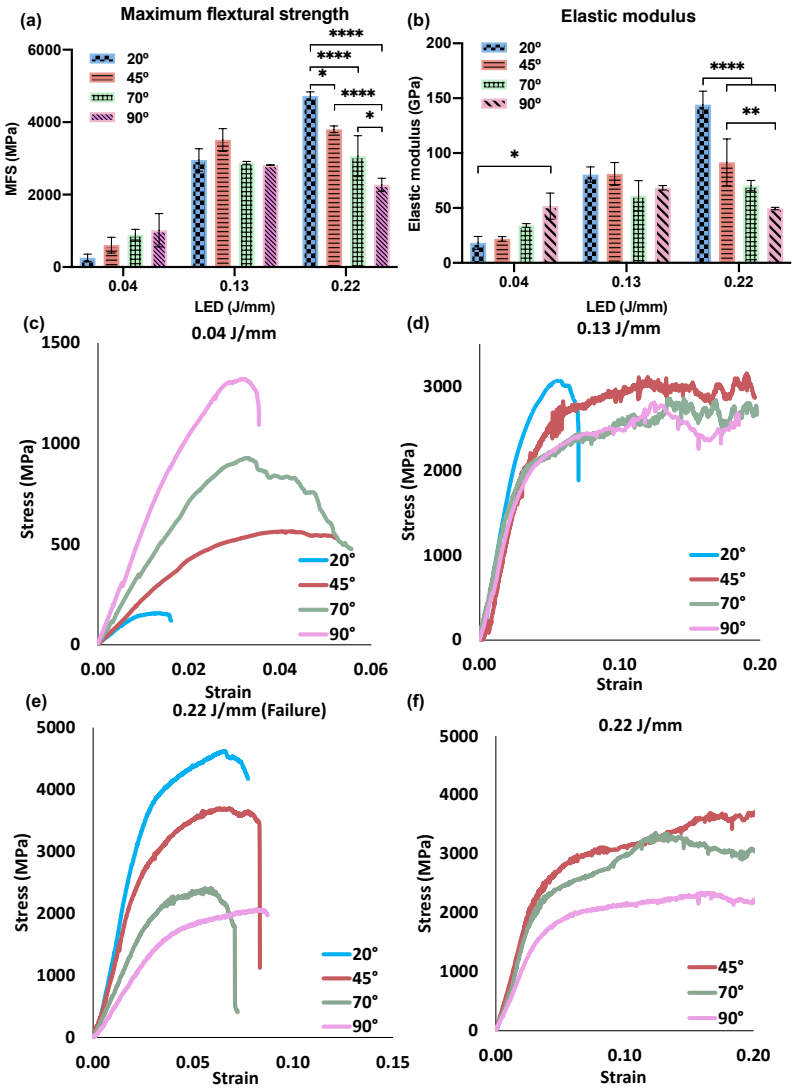

Figure 4.4 3-point bending results showing build angle effects for (a) MFS and (b) elastic modulus of struts; force-displacement curve taken at different LED of (c) 0.04 J/mm, (d) 0.13 J/mm, 0.22 J/mm for (e) failure occurred and (f) without failure.

Struts built at 20˚ all ruptured by crack propagation regardless of process parameters (Fig. 4.5 (a)), where the failed samples showed crack propagation along a zigzag path. No

cracks or fracture were found for struts above 45˚ processed at 0.13 J/mm. Where cracks can be clearly seen on the struts, 0.22 J/mm specimens that ruptured after plastic deformation displayed a notable pore pit at the fracture surface, except those manufactured at 20˚ (Fig. 4.5 (b)). These pores were surrounded by smooth and concentric shapes and displayed rough fracture surfaces. Fig. 4.5 (b) shows secondary electron micrographs of the fracture surface featuring notable dimples and voids, suggesting a ductile behaviour of the 0.22 J/mm manufactured struts.

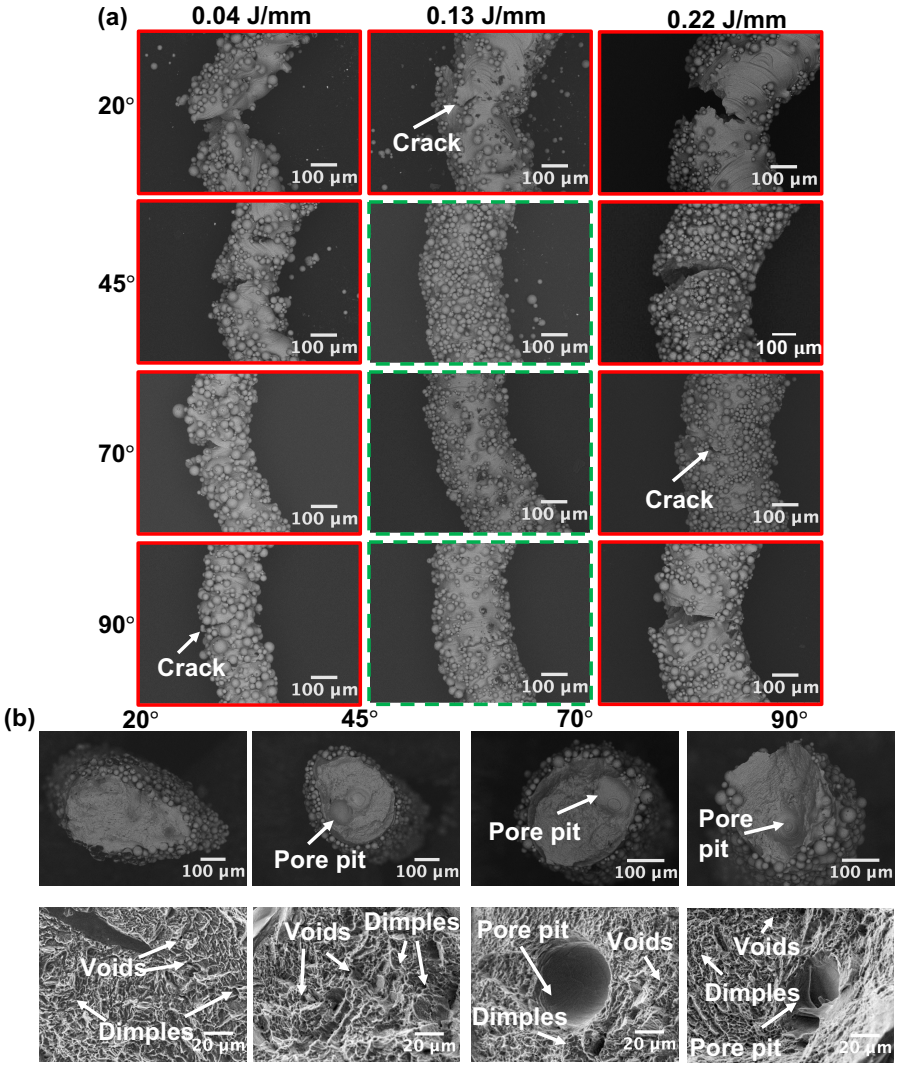

Figure 4.5 Images showing fabricated struts (a) failure in red solid frame and without failure in green dashed frame after bending test; (b) showing cross-section of 0.22 J/mm manufactured struts after failure occurred to illustrate the ductile topography of Ti64 struts.

4.3.4 Effect of process parameters and struts angle on in-vitro osteoblast response

Following dynamic seeding of the struts, cellular adhesion was visualised by fluorescent microscopy. Viable cells could be seen distributed throughout the struts surface in all groups (Fig. 4.6 (a)). The 20˚ struts exhibited increased quantity of cells towards the edge of the struts, whilst cell distribution was more homogenous in the 45˚ and 70˚ struts. Quantification of the images in fig. 4.6 (c) confirmed that 20˚ struts exhibited a significant increase in cell attachment when compared to the 45˚ and 70˚ struts. These findings are likely due to the increased roughness exhibited by the 20˚ struts which likely correlates to increased cell adhesion at early time points. Following 21 days of osteogenic culture, live/dead staining showed that cells on the struts were highly viable and reached confluency in all groups (Fig. 4.6 (b)).

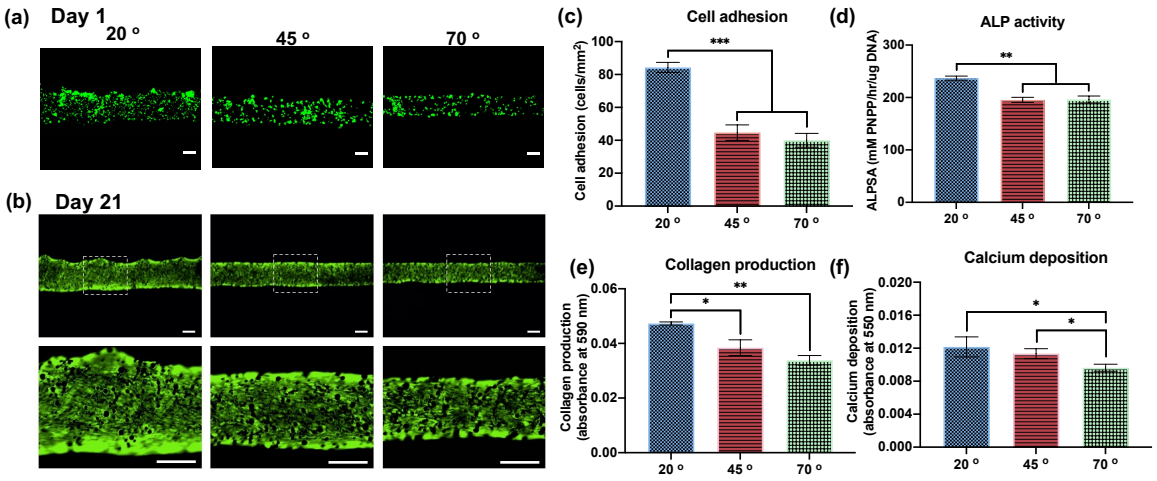

Figure 4.6 Microscopy images showing live cell adhesion on struts surface for (a) day 1 and (b) live/dead cell staining after 21-days culture, plots illustrating (c) cell adhesion, (d) ALP activity, (e) collagen production and (f) calcium deposition on 20° to 70° struts, scale bar represented 200 m for all.

To investigate the influence of the different strut fabrication angles on osteogenic differentiation, alkaline phosphatase (ALP) activity, collagen production and calcium deposition were evaluated. Initially, ALP activity, an early marker of osteogenesis, was evaluated following 14 days in osteo-inductive culture. The findings in fig. 4.6 (d) showed significantly enhanced ALP levels within the 20˚ groups when compared to the 45˚ and 70˚ struts ($p \leq 0.01$). Picrosirius red staining showed that the 20˚ struts exhibited a significant increase in collagen content when compared to the 45˚ ($p \leq 0.05$) and 70˚ struts ($p \leq 0.01$) (Fig. 4.6 (e)). Similarly, in fig. 4.6 (f) alizarin red staining for calcium deposition showed that the 20˚ and 45˚ struts exhibited substantial increase in calcium deposition when compared to the 70˚ group ($p \leq 0.05$). The osteogenic differentiation induced by these different struts clearly shows that reducing the struts angle enhances the osteogenic capacity of cells on these materials. This is likely attributed to the increased roughness observed on these lower tilted struts, as several studies have indicated the influence of roughness on osteo-induction.

4.4 Discussion

The occurrence of lack of fusion (Fig. 4.2 (a)) in struts built at 0.04 J/mm LED can be attributed to insufficient laser energy input, resulting in un-melted powder particles existing between the adjacent melted regions [114]. Lack of fusion tends to be more obvious and severe as struts angle decreasing, due to the larger powder area left un-melted by a low laser energy input. Balling effect fusion (Fig. 4.2 (a)), resulting from poor wettability is also reported to be more prevalent under low energy density conditions as a resulting in spheroidization and discontinuity of the melt pool [81] alongside poor bonding between layers. At higher LED (0.22 J/mm), escaping material vapour during

melting leads to keyhole formation and subsequent porosity following its collapse [219]. Besides, the vertically aligned melt pool between layers of 90˚ possibly leads to the repeating deposited materials experiencing more intense and frequent heat of laser compared to lower struts angle (Fig. 4.2 (a)). This effect of heat accumulation generated as a results of multiple re-melting might increase the porosity for 90˚ struts [220].

At low LED, lack of fusion and balling would be the main factors increasing R_a. These defects not only create an inherent roughness due to introducing discontinuity of material, but they also disrupt the uniform deposition of subsequent powder layers [102]. Process conditions could play a more important role on the roughness profile at this low LED stage than strut angle, leading to the poor melting of materials regardless of geometric angle (Fig. 4.3 (a) and (c)). Whilst as the LED increases, so too does melt pool depth and width which may improve inter-layer bonding and remelting of surface adhered particles. On the other hand, because of loose powders largely distributed at the lower surface as the struts angle decreases, poor heat conduction would expand the formation of overhang for low-angle struts [108]. Surface irregularities could be more observable as the increasing LED causes formation of wider and deeper melt pool, therefore larger sintering of raw materials, leading to greater R_a of lower surface (Fig. 4.3 (b)).

The failure of 3-point bending test samples occurred in all specimens when applying the lowest LED with insufficient energy input resulting in high porosity generated by lack of fusion. The large size and irregular shape of these pores may act as stress concentration and subsequent crack initiation points which leads to weak load-bearing capacity, impacting both mechanical strength and stiffness [221]. As LED increases, enhanced

ductility for struts above 45˚ indicates the importance of optimising parameters for elimination of enclosed pores. For struts manufactured with LED 0.22 J/mm, the failure mode of all the specimens agreed with the study of Paulo et al. and Costanzo et al [222, 223]. At the highest LED, the increased porosity for higher angle struts due to keyhole and gas pore defects (especially for 90˚ struts) may be a critical factor in reducing strength and elastic modulus. The pore pit located at the fracture point for struts above 45˚ are considered as stress concentration risers, which can cause the struts to fail under relatively low level of stress, inducing the failure and propagating to the surrounding solidified region [224].

Moreover, the strut angle and as-built strut thickness tends to result in the dramatic changing of the UFS and elastic modulus (Fig. 4.2 (b) and Fig. 4.4 (b)). It has been found that part heat accumulation depends on build angle, leading to the variation of both mechanical properties and internal porosity [225]. Consistent with the phenomena in this work, it was demonstrated by Palmeri et al. that the Ti64 samples built above 45˚ exhibited lower mechanical strength and higher ductility than the samples built below 45˚. These findings were associated with an increasing heat accumulation due to the larger volume of the solidified materials and number of layers, that below the depositing layer of higher struts angles. Furthermore, as Barba et al. observed that the microstructure could be influenced by the changing of strut size and build orientation, which could potentially cause differences in elastic modulus [92]. It can also be assumed that the failure occurrence was associated with average roughness. The high R_a of 20˚ struts lower surface can influence the mechanical performance of lattices by creating stress concentrations or microcracks at the peaks and valleys of the rough surface and reducing

the overall ductility of the part. This phenomenon corresponds with the results observed by Scott et al., indicating that the higher roughness would be more detrimental to mechanical properties of components, causing earlier strain (work)-to-failure [226]. As explained, struts above 45˚ manufactured by LED of 0.13 J/mm which showed the lowest R_a. Therefore, struts could be less distorted, uniformly melted and solidified, ensuring a more consistent microstructure and stable mechanical properties throughout the part.

There is a growing body of evidence demonstrating the influence of mechanobiological interactions between cells and their substrates on directing cell behaviour [227, 228]. The substrates surface roughness has been proved to critically influence cell response [229]. At optimised process parameters, osteoblasts were shown to preferably adhere to and proliferate on as-build struts of lower angle below 45˚. The results of cell adhesion in fig. 4.6 (c) fit with the changing of lower-surface R_a in fig. 4.3 (a), indicating that a rougher surface is probably a positive factor to enhance initial contact between the implant and cells, a critical process for successful osseointegration. In addition to the initial cell adhesion, several studies have demonstrated the role of substrate roughness on improved osteogenic differentiation via the activation of mechanotransducive signalling [230, 231].

In the present study, we observed that the rougher surfaces also facilitated osteoblast collagen production and calcium deposition. This suggests that the selection of struts angle is extremely important for the initial cell behaviour and the subsequent osseointegration process. Meanwhile, the attached partially melted powders were not shown to be covered by cells, emphasising the importance of eliminating these particles during post processing. These observations are in line with the work of Cox et al., where

the relatively large angle between partially melted particles and the solid surface might block the spread of cells [229].

With the idea of improving implant mechanical and biological properties whilst controlling the manufacturing process, a map was developed to guide the design of AM lattices. Fig. 4.7 (a) defined the angle and used to calculate the struts angle assembled in a BCC lattice. Starting from either adjusting build orientation of lattices, fig. 4.7(b) or adjusting the unit cell size (height) (Fig. 4.7(c)), the build angle of individual strut , and in the lattice can be customised. As the gradient colour maps of fig. 4.7(d) & (e) indicate, struts built lower than 45˚ display improved osteoblast cell adhesion but poor mechanical performance (green), while struts built above 45˚ show an opposite behaviour (red) with a superior ductility but reduced cell response. Overall, 45˚ struts built with LED of 0.13 J/mm showcase superior properties in both mechanical strength and osteoblast behaviour than other struts. The deviation from 45˚ was thus calculated by Eq. 4.4 and Eq. 4.5, which can be used as an indicator to determine the actual build angle of struts in a rotated or unit cell size changed lattice.

$$\text{Deviation from } 45^\circ = \sqrt{(\alpha^* - 45^\circ)^2 + (\alpha^{**} - 45^\circ)^2 + 2 * (\gamma - 45^\circ)^2} \quad (4.4)$$

$$\text{Deviation from } 45^\circ = 2 * |(\alpha^* - 45^\circ)| \quad (4.5)$$

Struts angle against lattice rotation in fig. 4.7 (d) can be used to select the orientation of a preferred BCC unit cell in a selected geometry, assisting further design and property modification of the whole part. Meanwhile, fig. 4.7 (e) showcases a design map to modify a lattice with fixed orientation These two approaches can be combined to enable full tailoring of unit cell height and/or part build orientation to optimise geometry of lattices

(Fig. 4.7 (f)). Furthermore, these could be adapted depending on specific needs on an implant.

The ideal and key properties of porous metallic implants include biocompatibility, comparable mechanical strength and stiffness, surface morphology facilitating cell attachment, proliferation, differentiation and migration [232]. For biomedical devices requiring load bearing, it is critical to avoid mechanical failure while maintaining suitable mechanical strength of implants to patients' bone, which is further challenged by different bone conditions, such as quality, density, and disease location of bone [233]. The representative 3-point bending results suggest that lattice struts manufactured above 45˚ have exceptional ductility without failure, plus a wide range of strength between 2811 MPa to 3715 MPa that could be tailored into porous implants to meet various personalisation requirement. Mechanical strength and elastic modulus could be adjusted through either rotating lattice or varying unit cell height, therefore, by containing more, or less struts above 45˚ to accommodate broader bone implants application.

When bone defect exceeds the size limit (approximately cm) of bone self-regeneration, implantable lattices with surface quality satisfying bone cell response are essential to promote initial bone ingrowth effectively. In this study, it is demonstrated that AM processed struts with different topological features could significantly influence mammalian cell behaviour, where the struts built below 45˚ possess an outstanding performance on bone cell attachment, proliferation, and differentiation. This work created the map to allow users to select lattices with precise control of surface finish to improve bone regeneration process [131]. The map with the customisation function of combining

the mechanical and surface morphology features, could be particularly applicable as new-generation bone substitute for bone defects repair caused by trauma, tumour, or functional atrophy [234]. In the future, it is also essential to explore the optimal build orientation of whole lattices regarding to the map. De Biasi et al. has proposed and verified a cost-efficient way to utilise struts and nodes built with different orientations to predict and improve the fatigue of lattice structures through algorithm driven by experimental results [235]. Further utilizations of the map to design optimal meta-biomaterials has been taken into account by the authors, to conduct evaluation and verification by combining simulation and experimental work.

Moreover, given the highly complex and fine geometry features of lattices, common post-processing, such as sand blasting, would be extremely difficult to complete for these geometries. Thus, this approach could also be potentially useful to select part build orientation and/or unit cell height to alter and predict surface quality, conducting further post-process, rendering higher efficiency for research community, engineers, AM users and clinicians.

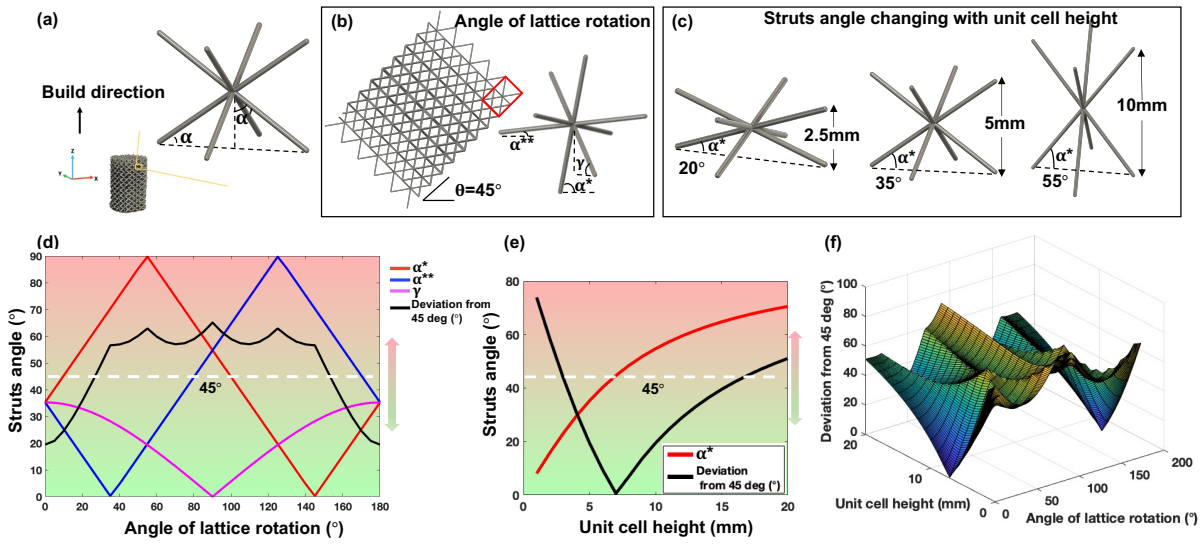

Figure 4.7 (a) BCC unit cell showing the angles used for the determination of actual strut angle after lattice rotation and unit cell height changing; (b) showing an example of unit cell orientated when rotating a lattice to angle of θ=45°, α*, α** and γ indicate the actual build angle of struts (c) presenting the difference of struts angle after the unit cell height adjusted; (d) illustrating struts angle being manufactured in a rotated lattice, whilst (e) plotting the build angle of struts when unit cell height changes; up-down arrows indicate areas for enhanced ductility but poor cell attachment (red) or improved cell adhesion but reduced ductility (green); (f) map illustrating the deviation of struts angle from 45 while rotating the lattices and adjusting the unit cell height.

4.5 Conclusions

To improve of the osseointegration ability of Ti64 porous medical devices, this study explored the effect of process parameters and struts angle on surface quality, mechanical properties, and cell response of lattice struts. From the presented results, it was observed that both laser energy input and design properties heavily influenced the behaviour of the final product. For struts built at optimised LED of 0.13 J/mm, all parts were fully melted with those above 45˚ exhibiting greater ductility without obvious failure. For strut angles below 45˚, mammalian cells showed the preference of attachment, proliferation, and mineralisation to the overall rougher surface comparing to struts built higher than 45˚.

However, a less ductile behaviour from 3-point bending test was observed at low struts angle. An image analysis method was developed to detect the whole profile roughness of struts and promised to be an effective way to represent and predict the surface quality of complex lattice structure.

Combining these findings, by using 45˚ as a reference and BCC lattice as a representative demonstrator, processing maps were developed to take advantage of part rotation and unit cell design to optimise complex AM structures. As a design-assistance map, the final output would be able to enable functionalisation of these parts during the early manufacturing stages for improved mechanical and/or cell behaviour. Thus, it will be possible to predict and modify the properties of PBF-LB latticed structures in situ, increasing the confidence and applicability of these techniques for all AM stakeholders, and healthcare professionals while also improving the outcomes of medical devices.

Chapter 5 MULTI-CONTOUR SCANNING STRATEGIES OF LATTICE STRUCTURES

Abstract

Porous lattice structures are being extensively investigated for mechanical modulation of biomedical implants. The laser scan strategy used to additively manufacture these intricate designs significantly influences key physicochemical properties, including geometrical accuracy. Typically, a single laser contour and fill (SC+F) strategy is employed for bulk parts, however when producing fine lattices this may create an imbalanced laser energy input.

In this chapter, multi-contour (MC) approaches for PBF-LB are explored with the aim of acquiring consistent and stable manufacture of fine lattice structures. To evaluate adaptability of MC strategies lattices struts were produced as various angles (9˚, 45˚, and 65˚) and thicknesses (250 µm and 450 µm). Results show that when using an optimised linear energy density of 0.13 J/mm, and appropriate contour distance, geometric error was reduced to 0.5%, and the enclosed pores to 0.006% by using MC. Moreover, roughness was decreased to 3.4 µm for the upper surface, and to 9.7 µm for the lower surface due to improved uniformity of the melt pool when employing MC. Besides, the compressive results of MC show 17% improved ductility than SC+F, which was attributed to fewer

edge defects in struts produced by MC compared with SC+F. Whilst, all the samples were dominated by acicular / martensite without obvious preferential texture.

5.1 Introduction

PBF-LB has made it possible to produce porous lattice structures that may be used to reduce orthopaedic implant stress-shielding and promote osseointegration [11]. Laser power and scan speed are the most common PBF-LB parameters that are optimised since they effect geometric accuracy, surface roughness, and the formation of internal defects [112, 236]. The effects of PBF-LB scanning strategy has also widely been studied for bulk Ti64 components, enabling microstructure refinement and thereby improved mechanical properties [237]. Notably, the part size and build orientation also play significant roles in defining microstructure and mechanical properties [92]. Specifically, they concluded that as the volume of Ti64 parts increases from thin beam to surface and bulk, the microstructural features changed from fine to coarse and in turn this reduced ductility and tensile yield strength while increasing the number of defects. This showcases the importance of aligning PBF-LB parameter optimisation with part geometry, conditions used for bulk parts are not appropriate for fine lattice structures [238]. As the development of lattice structures requires broader geometric and dimension variety, such as stochastic lattices with various strut angle, graded lattices with different strut thickness, the exploitation of specific scanning strategy and parameters are suggested to facility this design freedom [239].

Initiating from different directions, some studies have focused on developing scanning strategies specifically for lattice structures. Vrána et al. reported that applying a contour

scanning strategy has advantages for manufacturing metal lattice structures [238]. Their results showed that surface roughness of contour strategy was reduced compared to use of default hatching parameters. Whilst the material density was achieved up to 99.8% of by an adjusted linear energy density of 0.25 – 0.4 J/mm in a wide range of strut thickness of 0.6 – 3 mm. Whilst Pauzon et al. found that the geometric accuracy of Alloy 718 with a maximum deviation nearly zero, and compressive yield strength of 141.51 ± 5.9 MPa can be largely improved by using border contour strategy, compared to the gyroid lattices manufactured without contour (geometric deviation shifted –50 μm and 81.3 ± 9.8 MPa of yield strength) [240]. Karami et al. compared the continuous and pulsed laser scanning strategy with less defects and higher fatigue resistance found when using a continuous laser mode, while a more homogenous microstructure was observed for the pulsed mode and thus a more isotropic mechanical performance [241]. Moreover, Onal et al. explored the microstructure for lattices printed by single point exposure strategy, the microstructure of double melted lattices possess a more uniform -lamellar microstructure and resulted in improved mechanical properties compared to a single melted structure [242]. As Qian et al. reported that the length of scanning vector can also influence the final mechanical deformation due to different heat dissipation, where the shorter length of the island scanning strategy could effectively lower the temperature gradient [243].

One of the main underlying mechanisms that PBF-LB scanning strategies may influence parts is through thermal history that ultimately influences microstructure. More specifically, thermal gradient, cooling rate, and direction of heat flow significantly impact grain size, grain aspect ratio, texture intensity, dislocation density and solidification cell size [244, 245]. Among these, Thijs et al. concluded that the elongation

direction of grains in Ti64 bulk material relies on the local heat conduction behaviour decided by the scanning strategy. This can be a powerful tool to control the grain orientation and therefore the microstructural texture [78]. It can be seen from their work that the grain slanted to the left as the laser beam moved from right to left, and vice versa. They explained with the pragmatic model, where the grain growth direction is perpendicular to the isotherm of the melt pool is influenced by scanning strategy and local part geometry. Furthermore, Al Mangour et al. found that the remelting of their design double scanning strategy influences the grain size of the PBF-LB bulk TiC/316L material resulting in the formation of finer dendrites [246]. A decreasing number of pores was also reported by the remelting process.

Factors of scanning strategy including rotation angle, length scanning vector, and distance of scanning vector, all of which may influence the properties of PBF-LB parts. For example, the island strategy with shorter scanning vector allows less interval time between two neighboured scanning vectors. Hence, the surface temperature of subsequent printing would be higher than the initial temperature of the powder layer, potentially reducing the temperature gradient [247]. Liu et al. found that the default bi-directional scanning strategy without scan vector rotation led to parts with higher yield strength and 17% higher elongation than samples manufactured with scanning vector rotated 90 [248]. Overall the literature highlights that control of scanning strategy enables desirable properties of PBF-LB part.

Since as-built Ti64 presents an acicular α′/ α martensite possessing high strength but low ductility, several researchers have explored post manufacturing treatments to optimise microstructure for improving mechanical properties [241]. Most of the studies focused on improving the mechanical properties of Ti64 lattice structures through tailoring the topological design [249, 250] or heat treatment [251, 252]. Pegues et al. suggested that the thermal gradient and solidification rate governed by PBF-LB process parameters, provides potential opportunities to adjust the microstructure of bulk Ti64 parts [107]. Notably limited work has been conducted on achieving desirable properties of Ti64 lattice structures via in-process parameters and scanning strategies.

Herein, a multi-contour (MC) strategy was developed specifically for production of Ti64 lattice structures. MC was defined as laser scanning the material based on the structure contour shape circle-by-circle with a given distance. Save for few studies, effects of MC process parameters on geometric, defects generation, surface roughness, mechanical properties and microstructure are rarely reported for Ti64 lattice manufacturing [240, 253]. As showing in fig. 5.1 (b) and (c), the length of scanning vector is non-uniform in the default hatch filling and contour (i.e. SC+F), while the MC maintains a symmetric and uniform scanning pattern for various geometric changes of lattice structures. To address the difficulties of manufacturing complex lattices regardless of dimensions, topology design or build angles, herein, scanning strategy including MC, single contour (SC) and contour with filling (SC+F), and the effects of process parameters on manufacturing accuracy, defects, surface quality, mechanical properties and microstructure were explored. An industrial in-situ monitoring system was also used to evaluate changes in melt pool responses. MC scanning strategy was optimised to improve

the lattice manufacturing and associated property refinement. It is the first time that the understanding of MC microstructure and mechanical properties are studied and compared with that of SC and SC+F in Ti64 lattices. This could further assist the development of bespoke orthopaedic devices, encourage the variety and novelty of implants design manufactured by PBF-LB.

5.2 Method

5.2.1 Design of Experiments and Manufacturing

20×20×20 mm BCC lattices with 450 μm struts thickness (Fig. 5.1(a)) were chosen to accommodate the strut size commonly applied for bone scaffolds and designed in nTopology (version 3.35.2, nTopology Inc., USA). 80˚ rotated lattices and the struts (9˚, 45˚, 65˚) consisted of it were also prepared for learning the effects of scanning strategies on surface finish to the lattices (Fig. 5.1(b)). Plasma atomised Ti-6Al-4V (Grade 23) powder feedstock with a size range of 15-53 μm was used to fabricate all samples in the RenAM 500S (Renishaw, UK). Notably, the pulsed mode in the Renishaw AM system used in this work is known as modulated mode. In this case, the laser fires for a pre-defined duration of time (i.e. exposure time), then switches off and moves to the next point according to a given distance (namely, point distance) [254]. Samples were all manufactured with layer thickness of 30 μm, and the point distance was fixed at 45 μm by varying the exposure time to study the influences of scan speed and laser power (Table 5.1). 80 μm and 125 μm contour distance between the inside and outer contour was chosen by measuring the previous hollow samples manufactured by single contour strategy. For the contour strategies, a laser power of 150 W and scanning speed of 1125 mm/s were used for the outer contour based on the parametric optimisation study of

Chapter 3&4 melting the metal powder with inside-out sequence [236]. Besides, contour with hatching scan were chosen to compare the differences and effects of scanning strategies on lattices manufacturing. Samples were named by '**linear energy density (J/mm)_contour distance (mm)**' as shown in Table 5.1.

Table 5.1 The scanning strategies and process parameters used for manufacturing the specimens.

Scan strategy	Contour distance (mm)	Border contour laser power (W)	Border contour scanning speed (mm/s)	Inside contour laser power (W)	Inside contour scanning speed (mm/s)	Sample name
MC	0.08	150	1125	100	2250	0.04_0.08
				150	1125	0.13_0.08
				200	900	0.22_0.08
	0.125	150	1125	100	2250	0.04_0.125
				150	1125	0.13_0.125
				200	900	0.22_0.125
SC		150	1125			
SC+F		100	1125	200 (Hatch)	1100 (Hatch)	

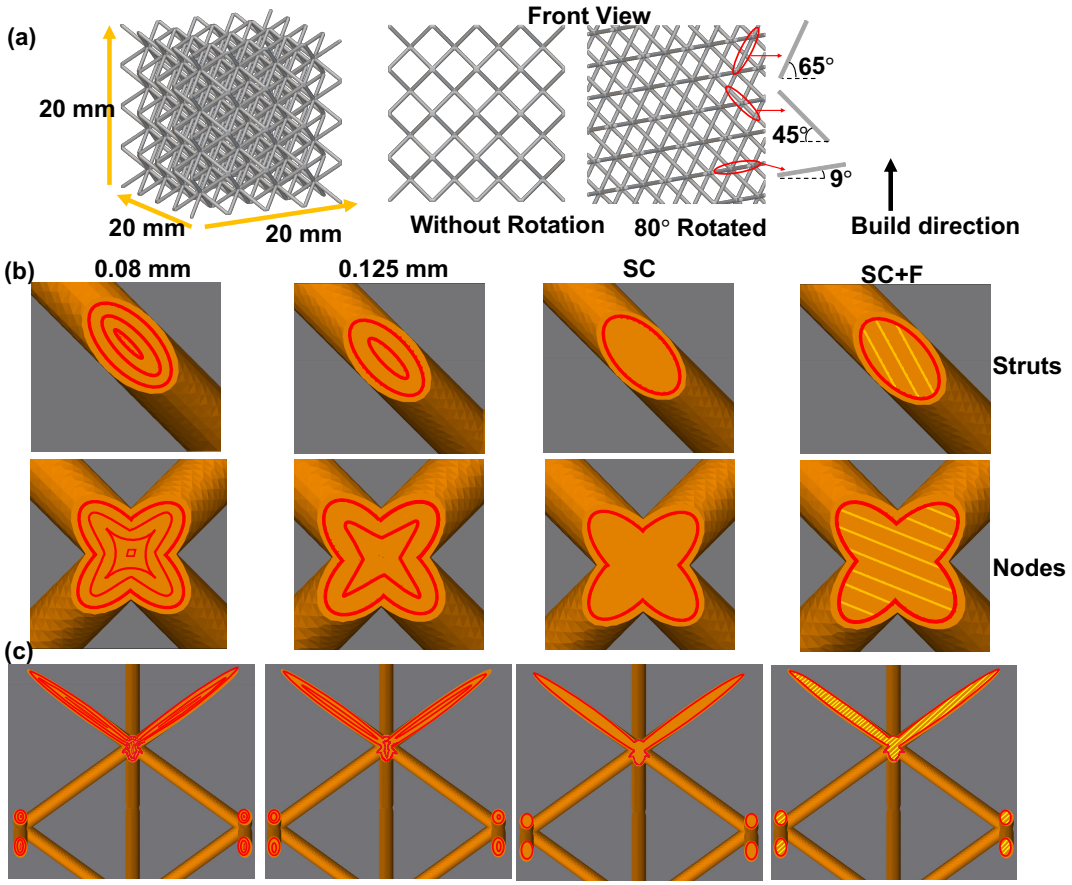

Figure 5.1 Images showing (a) dimension of lattices and the struts angle of the rotated lattices; (b) pattern of multi-contour (MC), single contour (SC) and contour with filling/hatching (SC+F) scanning strategy in non-rotated lattice, and (c) 80° rotated lattice.

During the process, the Renishaw InfiniAM Spectral system (AMPM system, Renishaw, UK) was used to monitor the melt pool response (MPR) in fig. 5.2. The optical emissions from both the laser and melt pool were captured by photodiodes. When the laser interacts with the powder bed, the melt pool (18) is formed (Fig. 5.2). The response is time averaged over the dwell time for each point in this system. A part of emitted radiation from melt pool (13, 15 &17) is transmitted back along the laser path, and directed by the mirrors to the two photodiodes (4&5) consisting the melt pool monitoring system [255]. To process the MPR dataset and visualise the actual energy input difference for different

parameters and scanning strategies, a MATLAB program was developed to locate specific lattice parts and layers of interest.

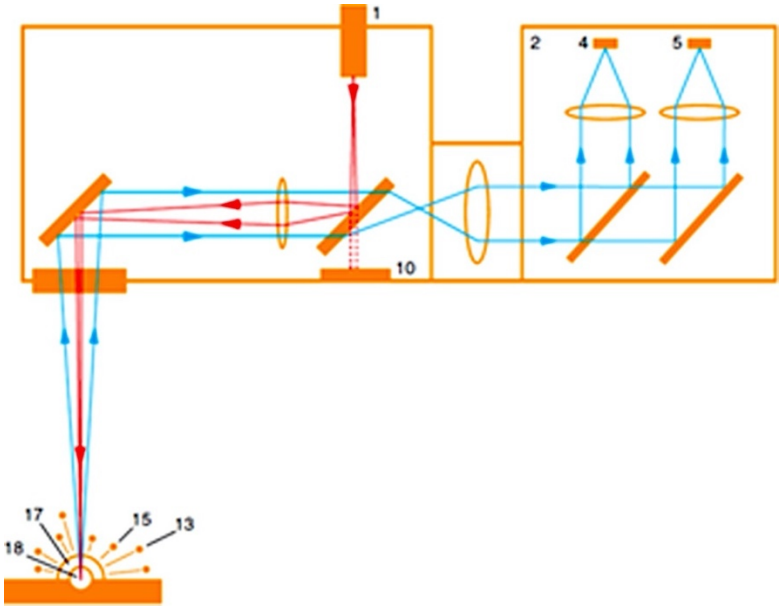

Figure 5.2 Diagram showing the Renishaw InfiniAM Spectral system for process monitoring, where the red arrows representing the laser path, the blue arrows meaning the melt pool radiation returned to photodiodes.

5.2.2 Characterisation of Geometry Accuracy and Average Roughness

Micrographs taken by scanning electron microscope (SEM, Hitachi TM3000, Japan) were analysed with ImageJ (NIH, USA., 1.53a) (Schneider et al., 2012). Strut contour was initially defined by an appropriate global threshold or via manual outline for fragmented sections. For both methods, the boundary included any internal pore areas. Individual struts within the lattice built at an angle of 37.6˚ resulting in an elliptical cross-section, thus, strut diameter was determined as the minor axis of a fit ellipse.

As-fabricated struts at 9˚, 45˚ and 65˚ were marked before removing from the plate for roughness measurements of upper and lower surfaces. Images were captured vertically to the sample surface using an optical profilometer (Alicona Infinite Focus G5, Austria)

with a 20× lens. Three areas from the up- and down-faces of each strut were scanned with average roughness (R_a) obtained with a cut-off wavelength of 2.5 mm as per ISO 4288-1996. Surface morphology of 9˚ struts were captured by SEM (Apreo 2S HiVac) at 20 kV and a current of 50 pA.

5.2.3 Micro_CT Characterisation

A CT system (Skyscan 1172 Bruker, Belgium) was used to investigate the 3D volume of struts. Scans were obtained using a voltage of 80 kV, current of 100 mA, exposure time of 5000 ms, an aluminium + copper filter, pixel size of 2.44 µm, camera resolution of 2664×1120, rotation step of 1.12˚ and a frame averaging of 4. The internal defects generated in the PBF-LB process were detected and exhibited in 3D geometries by CTan and CTvox after reconstruction in NRecon (version 1.7.1, Bruker).

5.2.4 Static Compression Test

Uniaxial static compression tests were conducted with a 50 kN load cell of the universal testing machine Z030 (ZwickRoell, United Kingdom) at ambient temperature. Three replicates of 0.13_0.08, 0.13_0.125, SC and SC+F were tested under 0.5 mm/min deformation rate, cylindric samples with dimension of 15 mm diameter and 20 mm height were designed. The elastic modulus was calculated at the linear elastic region from the slope of the stress-strain curve, while the yield strength was obtained at 0.2 % strain. Ultimate compressive strength (UCS) was also gained from the stress-strain plot. Fracture surfaces were captured by SEM (Hitachi TM3030, Japan).

5.2.5 Microstructure characterisation

Electron backscattered diffraction (EBSD, Jeol 7000, Japan) was conducted to detect the grain size and crystallographic orientation for down-selected lattices manufactured with multi-contour of 0.13_0.08 and 0.13_0.125, SC+F. Images were captured by a step size of 0.47 μm at 20 kV, after which EBSD results were analysed in AztecCyrstal (version 2.2, Oxford). The data collected by EBSD was analysed by an in-house script for prior-reconstruction according to the Burgers orientation relationship.

5.3 Results

5.3.1 Manufacturing accuracy

Struts thickness of lattices presented in fig. 5.3 (a) indicated a clear increasing relationship between struts thickness and the energy input for the same contour distance of MC. Noticeably, the thickness of single border contour lattice the lowest energy input showed a slightly higher value of 457.1±18.9 μm than that of 0.04_0.125, 0.13_0.125 and SC+F. By comparing the contour distance groups, it can be found that the struts thickness of lattices manufactured with 0.08 mm is larger than the 0.125 mm, regardless of the actual energy input. The 0.13_0.125 (447.7 ± 13.9 μm) and the default SC+F (447.9 ± 10.6 μm) share the lowest error of 0.5% in struts thickness, i.e., the highest geometric accuracy (Fig. 5.3 (b)). Besides, lattices manufactured by 0.22_0.08 presents the largest struts thickness of (497.7 ± 10.3 μm), whilst the struts thickness of 0.04_0.125 stays the lowest actual size of (442.0 ± 10.1 μm).

Surface finish of lattices was influenced differently by scanning strategies and parameters, where an obviously smooth surface of lattice top surface can be seen from the 0.22_0.08 and 0.22_0.125 samples in Fig 5.3 (c). On the other hand, with the lowest energy input and contour, a lack of fusion from the nodes was observed from the SC lattice.

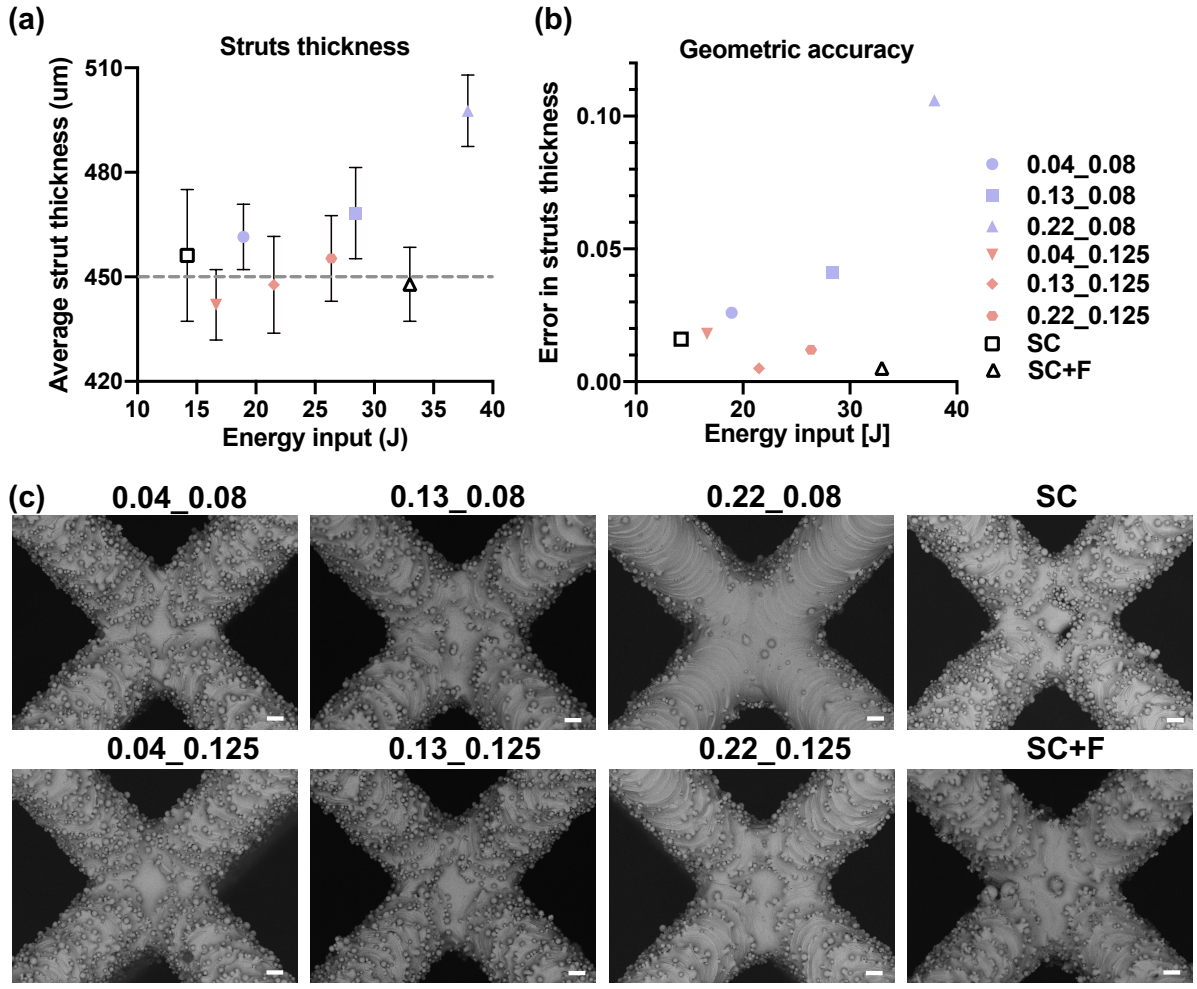

Figure 5.3 (a) Struts thickness and geometric accuracy versus energy input for all samples, (b) manufacturing error against energy input, and (c) SEM images for upper surface morphology (scale bar representing 100 μm).

5.3.2 Defects characterisation

Lattices of both non-rotated and the 80˚ rotated were characterised by scanning electron microscopy (SEM) to observe the defects generation at cross-section region of struts. As showed in fig. 5.4 (a) and (b), lack of fusion with irregular shape occurs in struts when

using the SC, 0.04_0.08 and 0.04_0.125 scanning strategies and parameters. The area of lack of fusion of 0.125 mm contour distance tends to be larger than the 0.08 mm, Larger un-melted area inside of the strut manufactured by SC shows a hollow structure with a powder channel of 217.1 µm. Pores appearing in 0.22_0.08, 0.22_0.125 and SC+F show a spherical shape, and sizes are within diameters of common gas pores of 1-100 µm and randomly distributed in the samples. However, the larger parameter of MC, including 0.22_0.13 and 0.22_0.08 presents less defects in the rotated lattices, where a larger cross-sectional area was exposed to the laser scan. Except for the SC+F strategy generates the pores in the rotated lattice. On the contrary, no clear pores were observed for MC 0.13_0.08 and 0.13_0.125 samples in both the non-rotated and 80˚ rotated lattices (Fig. 5.4 (a) & (b)).

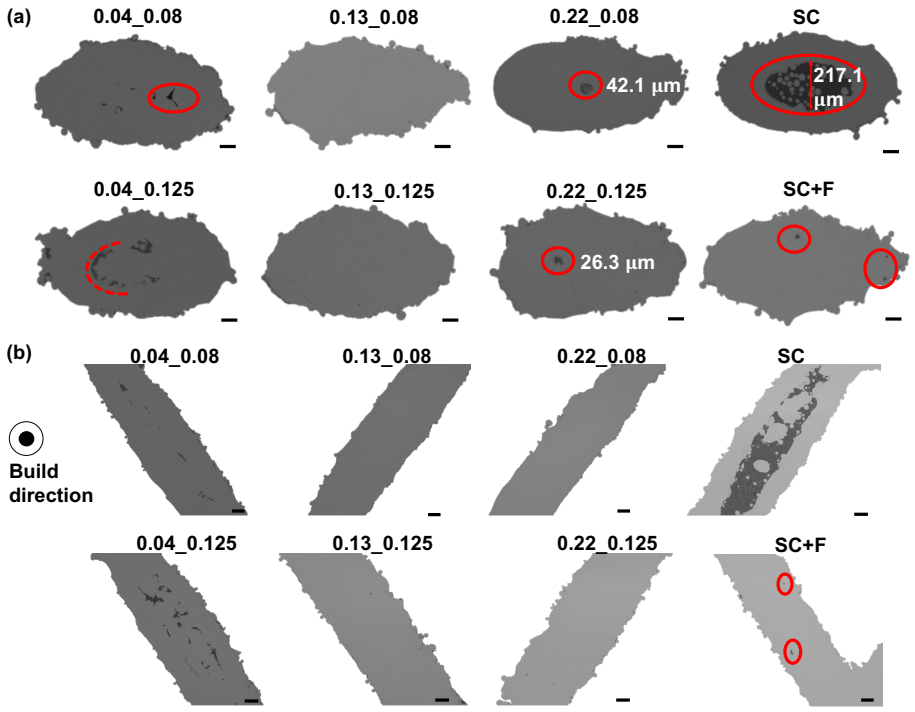

Figure 5.4 SEM micrographs for strut cross sections with internal defects highlighted in red (a) non-rotated lattices and (b) for 9° struts of 80° rotated lattices (scale bar representing 100 µm).

Based on the observation of pores in cross-section and geometric accuracy, 0.13_0.08 and 0.13_0.125 were down selected to further compare with SC and conventional SC+F strategies. CT was conducted to visualise in 3D and quantify the pores with red marked inside the lattices and zoomed in unit cell. From fig. 5.5 (a), it can be seen that no pores were found in the node areas of 0.13_0.08 with the lowest porosity of 0.004%. Comparing to it, pores in 0.13_0.125 and SC+F formed in the nodes or at the near-nodes zone (Fig. 5.5 (b) and (c)) with a higher closed porosity of 0.007% and 0.04%, respectively. Hollow structure in Fig. 5.5 (d) of SC demonstrates a severe lack of fusion effect due to low energy input, where Table 5.2 illustrates the SC has the highest volume of pores.

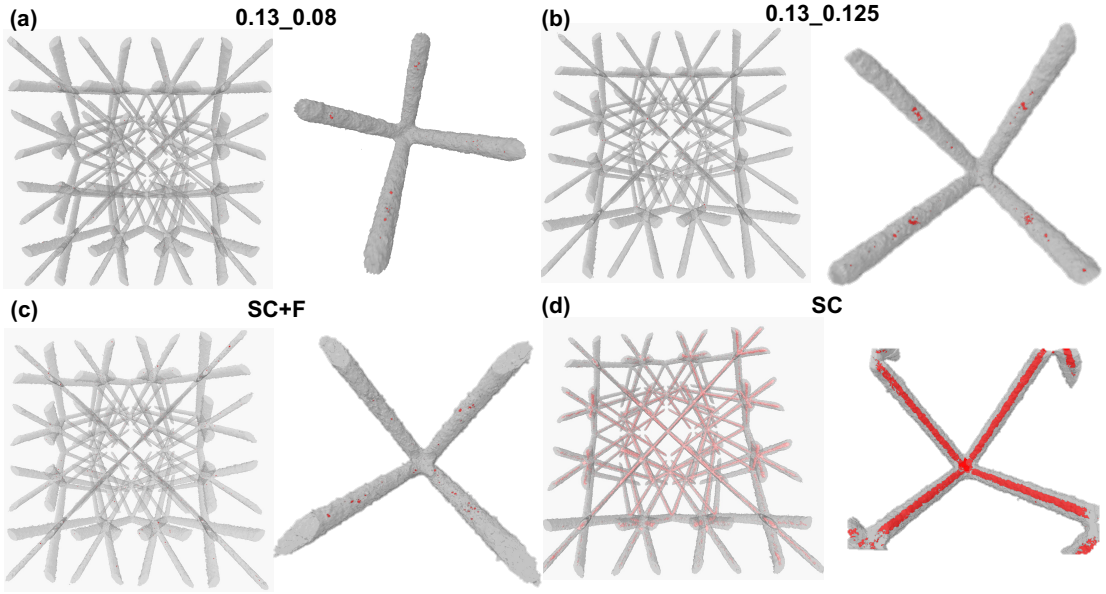

Figure 5.5 Volume renders of micro-CT images highlighting internal defects marked as red and shown with respect to the build direction for samples produced under different PBF-LB scan strategies (a) MC 0.13_0.08, (b) MC 0.13_0.125, (c) SC+F, and (d) SC.

Table 5.2 The comparison of closed pores inside of the lattices manufactured by different scanning strategies.

Sample ID	Number of closed pores	Volume of closed pores (mm^2)	Closed porosity (%)
0.13_0.08	824	0.01	0.006
0.13_0.125	530	0.011	0.007
SC	3141	0.045	0.04
SC+F	14724	0.142	0.07

5.3.3 Surface characterisation

9˚, 45˚ and 65˚ struts of 80˚ rotated lattices were evaluated to study the effects of scanning strategies and parameters on average roughness of struts produced at different angles to the build plate. From the micrographs of the 9˚ upper surface in Fig. 5.6 (a), the samples manufactured with contour strategy show smoother surfaces and less partially melted particles, especially for 0.13_0.08 and 0.22_0.08, that exhibited the lowest R_a for all the strut angles (Fig. 5.6 (b)). Moreover, the melt track of SC and MC strategies tend to be aligned along the struts, while SC+F performs a more random pattern (Fig. 5.6 (a)). It is obvious that surface finish is influenced by the inside contour and the parameters, where the R_a of all multi-contour samples are lower than the single contour.

Lower surfaces are heavily covered by the partially melted powders (Fig. 5.6 (c)), whilst showing higher R_a for 9˚ struts manufactured by SC (35.65 ± 11.98 μm) and SC+F (31.61 ± 15.77 μm) than the upper surface in Fig. 5.6 (d). However, for 45 and 65 the lower-surface R_a is more evenly distributed, among which the highest R_a is found for 0.22_0.08 and SC+F. Besides, in both upper and lower surface of the SC, voids due to lack of fusion can be observed in the low angle struts (Fig. 5.6 (a) and (c)).

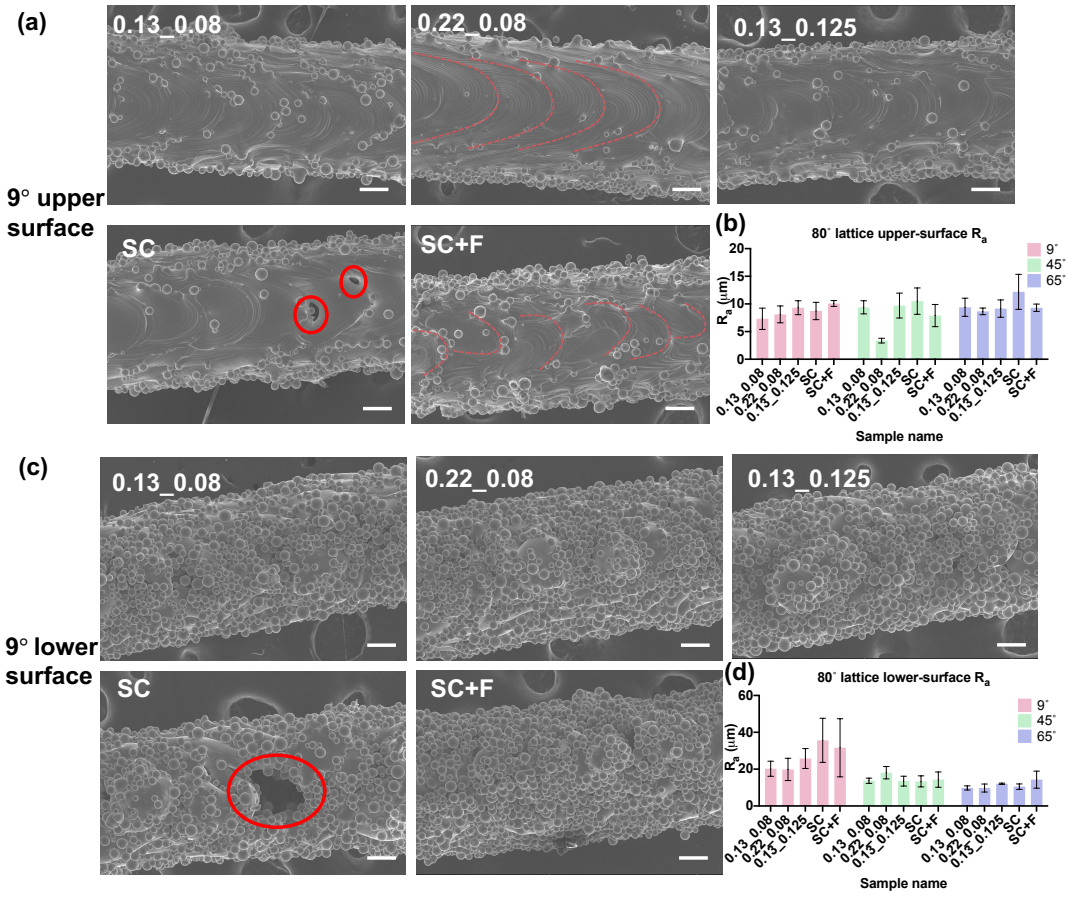

Figure 5.6 (a) SEM images of upper surface for 9° struts, (b) upper-surface Ra results of all strut angles for 80° rotated lattices, (c) images of lower surface for 9° struts, and (d) lower-surface Ra (scale bar representing 100 μm), red circle highlights the manufacturing defects of pores in SC.

5.3.4 Mechanical properties

Fig. 5.7 (a) and (b) illustrate the compressive properties of different scanning strategies and parameters. The elastic modulus, yield strength and the ultimate compression strength (UCS) in Table 5.3, are comparable between 0.13_0.08 (YS—51.64±1.16 MPa, UCS—72.69±0.87 MPa) and SC+F (YS--51.11±2.15 MPa, UC--71.38±1.71 MPa) without showing significant differences, whereas the ductility of SC+F (11.6±1.4%) is lower than the multi-contour 0.13_0.08 (13.8 ± 1.8%). Such phenomenon is also evident for 0.13_0.125 and SC, from which the ductility is higher than the SC+F. Besides, the

mechanical strength of 0.13_0.08 and SC+F is significantly higher ($p < 0.0001$) than 0.13_0.125 and SC.

Images of the fracture surfaces are presented in fig. 5.7 (c), from which a combined ductile and brittle fracture mechanism can be observed from all the samples. The elongated dimples in 0.13_0.08 and 0.13_0.125 illustrate that the lattice experienced plastic deformation before the fracture. A significant amount of cleavage facets in SC+F samples indicates less ductile behaviour, while micro-void calescence is predominantly distributed in the SC manufactured lattice.

Table 5.3 Compression test results of lattices manufactured by MC, SC and SC+F.

Sample name	Elastic modulus (MPa)	Yield Strength (MPa)	UCS (MPa)	Strain at failure (%)
0.13_0.08	1397.224.6	51.61.2	72.70.9	13.81.8
0.13_0.125	1125.033.2	40.5	57.71.8	14.01.2
SC	844.312.7	27.20.4	38.90.2	12.40.4
SC+F	1364.032.6	51.12.1	71.41.7	11.61.4

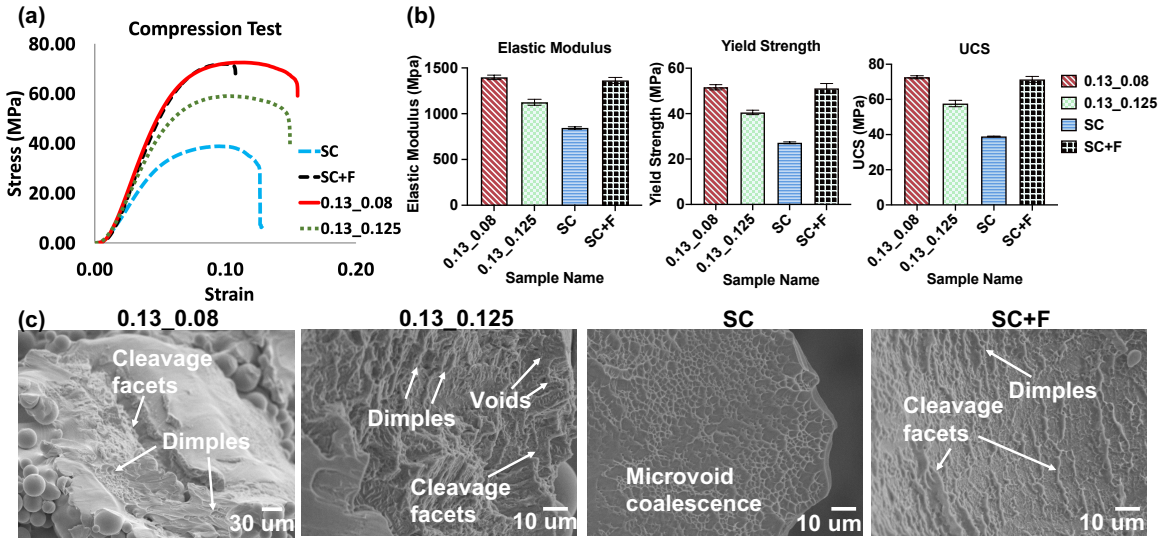

Figure 5.7 (a) Compressive stress-strain curves for lattice structures of different scanning strategies and parameters; (b) the comparison of elastic modulus, yield strength, and ultimate compressive strength; (c) images of the fracture surfaces for MC, SC and SC+F after failure.

5.3.5 Melt pool response

In order to visualise the thermal behaviour of different scanning strategies, melt pool response for MC, SC and SC+F is presented in fig. 5.8. The same slice of the scanning pattern was collected for all groups to compare the amount of energy input to the melt pool. Colour bars indicating the intensity of signals collected by the AMPM system. It should be clarified that although the same parameters were applied for each exposure, the MPR is different, which might be due to a data collection delay of the system. Numbers of inside-contour for 0.13_0.08 and 0.13_0.125 are clearly shown, where it is noticeable that the size of first inside-contour in 0.13_0.125 is between the size of first and second inside-contour in 0.13_0.08. Besides, even with an inside-contour for 0.13_0.125, the highest MPR of which is similar to the SC (220±20). However, comparing to 0.13_0.125, the highest MPR of 0.13_0.08 reached above 250. In addition, MPR of SC+F shows the

highest value can be attributed to the larger laser power and lower scanning speed for the hatching scan.

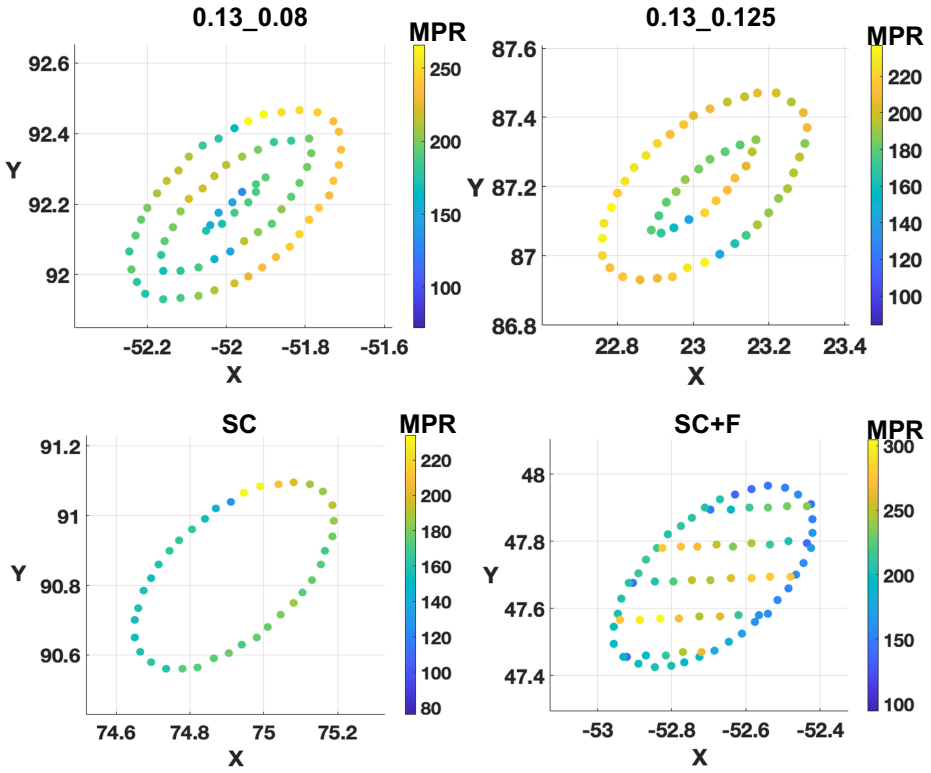

Figure 5.8 Melt pool response plotted showing actual energy input for single strut of lattices fabricated by 0.13_0.08, 0.13_0.125, SC and SC+F.

5.3.6 Microstructures

Generally, the observations of microstructure for samples along the build direction, mainly martensitic were found where fine and acicular α′(α) is the dominated phase in fig. 5.9 (a). 0.13_0.125 shows a more random texture than 0.13_0.08 and SC+F regards to the build direction, where the α′(α) laths display a preferred orientation along {0001} orientated to x or y axis for 0.13_0.08 and SC+F in fig. 5.9 (a).

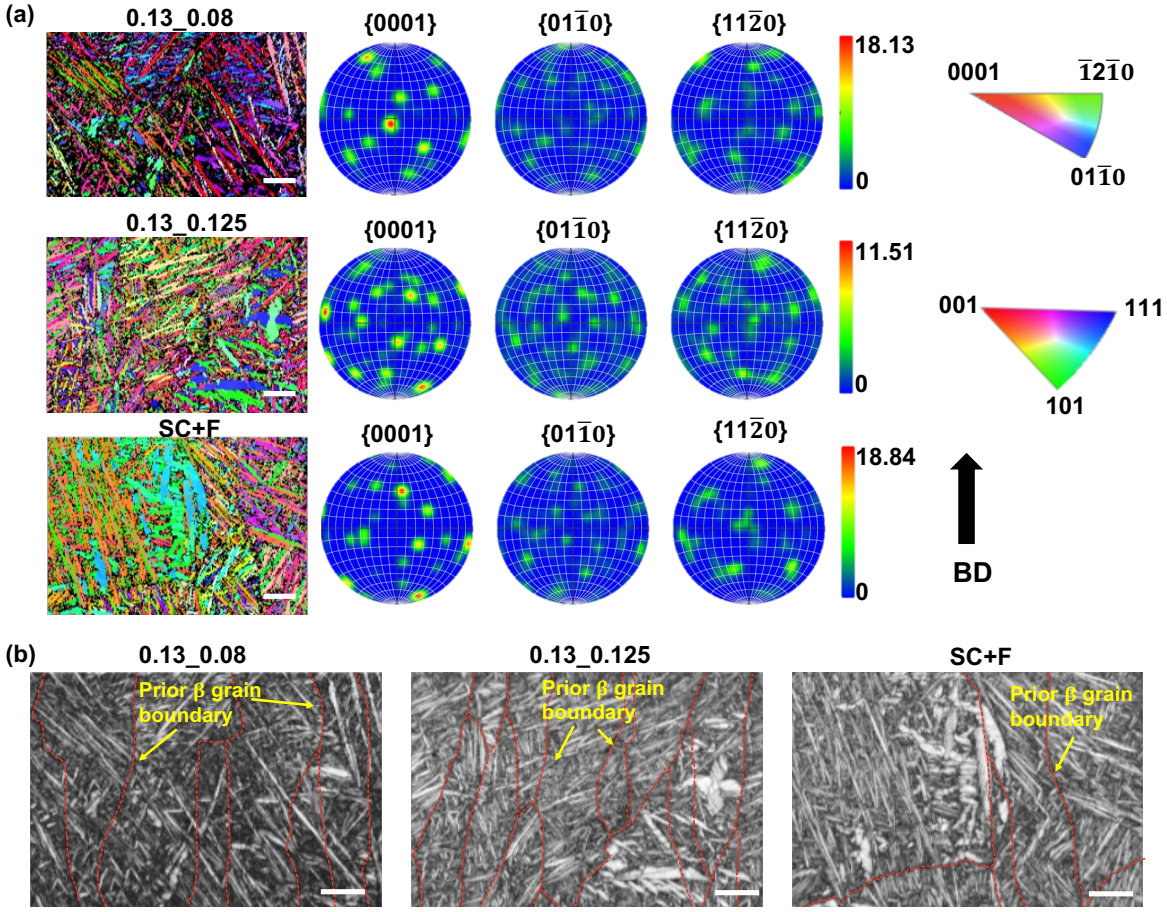

Figure 5.9 EBSD map, pole figures and inverse pole figure showing (a) samples with respect to the build direction, and (b) with respect to normal direction of 0.13_0.08, 0.13_0.125 and SC+F (scale bar representing 15 μm).

While prior β phase was poorly presented in the inverse pole figure (IPF), the band contrast in fig. 5.9 (b) helped to outline the prior grain boundaries, indicating the transformation from prior β phase to metastable martensite during the rapid solidification process. Besides, the prior β microstructure presents finer grains in the MC samples, 0.13_0.125 in particular (Fig. 5.10 (a)), compared to the more coarsening grains in SC+F (Fig. 5.10 (b)). A typical epitaxial growth of the reconstructed prior β columnar grains along the build direction in is observed in fig. 5.10.

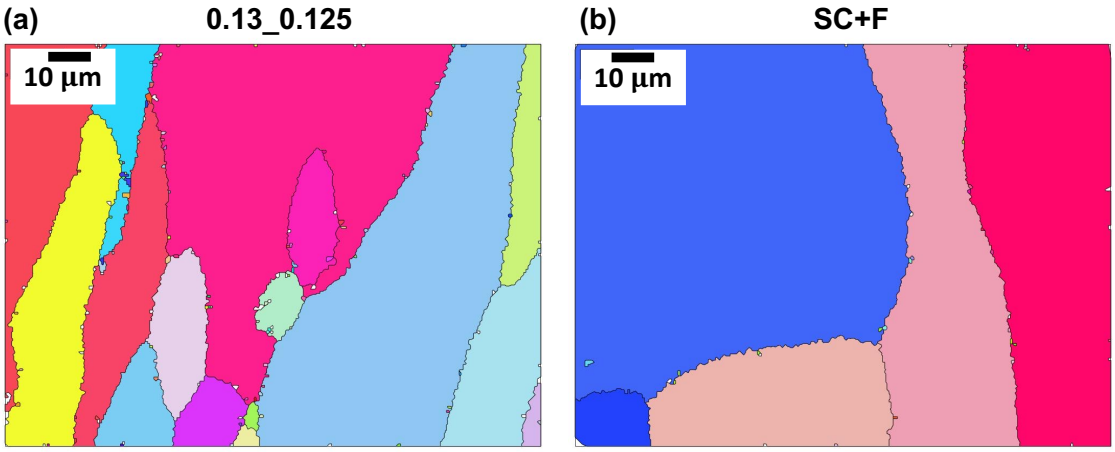

Figure 5.10 Reconstructed prior- grain microstructure of (a) 0.13_0.125 and (b) SC+F along the build direction.

5.4 Discussion

Scanning strategies influence the manufacturing accuracy significantly through number of contour and selection of parameters. It is interesting that although the energy input of SC+F is higher than other multi-contour scanning, the strut thickness of which is even lower than the SC. Thus, it can be assumed that the border contour plays a key role in deciding the overall strut thickness. The single border contour tends to generate the melt pool regarding to the scanning pattern designed in the pre-build software. Compare to the MC of using 0.125 mm distance with 0.04 J/mm and 0.13 J/mm, the higher struts thickness of SC might be attributed to increased wetting of the loose powder due to lower heat conduction than connecting to solidified adjacent tracks [208]. From the perspective of contour distance, it can be concluded that the re-melting is essential to the increased strut thickness regardless of the actual energy input, where 0.04_0.08 with low LED and lower distance presents higher thickness than 0.22_0.125 with higher energy input and larger contour distance.

The border contour tends to decide the final struts thickness of the lattice, while inside contour and hatching scan would influence both the defects generation and struts thickness due to the key role of scan distance [78]. Both the pre-defined scan path in fig. 5.1 (b) and MPR of SC+F in fig. 5.8 showcase regions of hatching path close to border contour in a distance less than 0.1 mm, indicating the inappropriate overlapping of melt pools cause the formation of keyhole and/or gas pores due to vapour pressure [256]. This is aligned with the pores observed in fig. 5.4 where pores located near the edge of upper and/ or lower surfaces. In contrast, the homogenous distance of scan path and suitable energy input such as 0.13_0.08 and 0.13_0.125 of MC ensure proper overlap of melt pool resulting in defect reduction.

Furthermore, length of scanning path in MC and SC+F is different, where the inside contour of MC is longer than SC+F (Fig. 5.1 (b) and Fig. 5.8) in a regular BCC lattice structures. As Lu et al. summarised, the shorter straight scan vector may lead to more pores [257]. Consistent with their finding, the MC has 1.8 times longer scanning vector of the inside contour than the longest scanning vector of SC+F. Both the shorter scanning vector and bi-directional scan of SC+F might lead to the pile-up of material towards one end of the scanning path, resulting in excessive powder spread to melt pool and generation of pores. The porosity of 0.04_0.125 could be attributed to the lack of insufficient overlapping at the low energy density parameter. Similarly, for shorter contour distance of 0.08 mm, even fewer irregular pores showed in fig. 5.4 (a), the lowest LED of 0.04 J/mm would also introduce lack of fusion due to the insufficient energy input.

It has been proved that the loose powders located at the down-facing side results in low heat conduction and therefore poor dissipation, while the new layer of powders on up-facing side is melted upon the previous solidified region where the heat could be largely dissipated [258]. Lower heat conduction of unsupported powders leads to amount of heat dissipated into the powder bed, partially melting or sintering powders then attach to the melt pool edge, causing the overhang effect and dross formation. Overall, the roughness of lower surface is influenced by the overhanging effect, where the lower surface is covered by partially melted powders are more severe on the low angle struts of 9. This is aligned with our previous work, for lower angle struts, larger area of the down-skin surfaces is exposed to the loose particles, lower heat conduction and therefore more heat dissipated to the powder bed [112]. The relative low R_a of 0.13_0.08 (7.32 $\pm$ 1.92 μm) and especially 0.22_0.08 (8.12 $\pm$ 1.53 μm) can be attributed to the re-melting effect.

Given that the pores within the SC sample were also found to preferentially occur at strut edges this also reiterates the importance of re-melting in relation to defects. In the case of SC+F there are areas in which the hatching tracks may overlap the contour, which as evidence by fig. 5.6 (b) and (d) may increase the absolute roughness or its degree of variation. Another factor to consider is the influence of scanning direction. In contrast to the uniform scanning tracks of MC strategy, the pore formation of SC+F due to overconcentrated and overheating could lead to irregular laser track and thus impact R_a [259]. It is generally accepted that the larger portion of pore defect can be detrimental to the strength and ductility, resulting from the decreasing of load-bearing areas led by the occurrence of defect in material [260]. In SC+F, the pore defects tend to appear stress

concentration and reach the yield limit to form cracks, following which the crack rapidly propagate until the brittle fracture leading to degradation of ductility.

In terms of compressive properties, both the 0.13_0.08 and SC+F present significant differences to 0.13_0.125 in the elastic modulus (19%), yield strength (22%) and UCS (21%), as well as SC. This could be attributed to the more textured microstructure cyclically obtained from the higher cooling rate [107]. Besides, the yield strength and UCS are related to any defects in the lattices, on which stress could concentrate leading to lower strength or poor ductility. Dimples and cleavage facets appeared in fracture surfaces for all samples except SC, which suggests a combined ductile and brittle behaviour during the mechanical loading. Larger re-melted regions of 0.13_0.08 and SC+F compared to 0.13_0.125 might lead to materials experiencing repeated melting and fast cooling and thus the {0001} of α phase strongly orientated towards the X or Y axis. This observation is consistent with the microstructural characteristics observed by Onel et al., the double-melted region of lattices presents more textured microstructure [242].

The mechanical behaviour of Ti64 lattices is largely dependent on its microstructural characteristics, which is fundamentally influenced by the thermal behaviour of the PBF-LB process. With a combination of low thermal gradient and high solidification rate, β microstructure tends to be finer and more equiaxed than a high thermal gradient and low solidification rate [107]. Although the parameters studied in this work are not different enough to completely change the β grain from columnar to equiaxed, a finer and less coarsened β grain microstructure was observed in fig. 5.10 (a). MPR might further

support this line of thinking, where a higher response value of SC+F than MC indicates the higher thermal gradient between the melting area and the surrounding powder material, causing the β microstructure to turn into larger columnar grains compared to the finer β grain in MC. Similar microstructural variation was reported by Barba et al., where larger columnar grains were observed in the hatching area within a Ti64 part [92]. Reflecting on the mechanical behaviour, high anisotropy of these structures is notable with high strength when loaded parallel to the columnar but lower ductility for highly textured α′(α). On the other hand, high thermal gradient has been proved that leading to thermal stress remained inside PBF-LB part, further causing early failure due to poor ductility [261].

5.5 Conclusion

Overall, the multi-contour strategy developed in this chapter with optimised process parameters provides an efficient way to manufacture lattice structures regardless of the dimensions and build angles. This study assists with understanding the of multi-contour strategy, which is necessary for manufacturing highly complex lattice structures. Lattices and struts built with different parameters and angles were manufactured to study the effects of different scanning strategy and parameters on geometric accuracy, surface quality, defects, mechanical properties, and microstructure by PBF-LB. It can be concluded that:

- The actual strut thickness depends on the inside contour distance and the process parameters, which increases with LED. The lowest manufacturing error of 0.005 was acquired at LED of 0.13 J/mm and contour distance of 0.125 mm and SC+F,

indicating that for struts dimension as large as 450 μm both scanning strategies are capable of assuring the geometric accuracy.

- Multi-contour strategy presents opportunities to reduce the size and numbers of defects within lattices, both 0.13_0.08 and 0.13_0.125 show 10 times fewer the number of closed pores compared to a traditional SC+F, and the pores were minimised at 0.13_0.08. Meanwhile, hollow structure appears while using single border contour due to insufficient melting of enlarged strut dimensions.
- Surface quality relates with the parameters and scanning strategy, where the remelting and higher LED of multi-contour led to the lowest R_a value for all build angles and surfaces was found for the struts manufactured by the 0.22_0.08. Thus, multi-contour shows its potential to improve the surface roughness through a more uniform melt pool track and re-melting process compared to conventional scanning strategy.
- Mechanical properties of lattices fabricated by multi-contour, especially ductility, was up to 17% higher than that of SC+F, attributing to the lower porosity and microstructural differences. The yield strength and ultimate compressive strength were not significant differences between 0.13_0.08 and SC+F.
- From the melt pool response, it can be confirmed that the actual energy input is influenced by the selection of scanning strategy and parameters.
- The microstructure shows α' dominated phase without strong texture in 0.13_0.125 along the build direction, but more textured for the 0.13_0.08 and SC+F. Smaller and more homogenised size of columnar grain in MC might play a key role in improving the ductility of lattice structures compared with the default SC+F.

Chapter 6 APPLYING ROTATION STRATEGY TO ENHANCE BIOMEDICAL RELATED PERFORMANCES OF LATTICES

Abstract

Powder bed fusion – laser beam (PBF-LB) has been commonly applied for the manufacture of lattices, enhancing the base material properties by creating a metamaterial for biomedical devices. However, the performance of lattices, such as mechanical properties and biological responses, are influenced by the lattice topologic design and surface quality.

In this work, three different rotation strategies involving the altering of strut angle and unit cell rotation with respect to the loading direction were investigated. Quasi-static compression fatigue and *in-vitro* test were conducted, where fatigue strength showed 98% increasing, and 67% increasing of DNA content expression for lattices applied rotation compared to the default lattice structure. To further guide the design and optimisation of meta-biomaterials, the mechanism of mechanical failure was explored for different build angles of strut. The findings and improvement of fatigue and biological response simply through tailoring the strut angle and unit cell orientation by rotating lattice structures,

showing its great potential to be applied for biomedical devices, as well as meeting the requirements for orthopaedic implants.

6.1 Introduction

Lattice structures has been intensively developed for their light-weight and mechanical properties applied in biomedical, aerospace, electronics and other areas [44]. With the development of additive manufacturing (AM), the advancement of functional materials has not been limited by changing alloy composition designs within monotonous bulk, but also achieve specific requirements through flexible geometric design [262]. Among the advantages of lattice structures, the high strength and low weight combination is one of the most important performances for load-bearing bone implants. For example, after the joint replacement implanted to the patients, it needs to sustain millions of times of cyclic musculoskeletal loads yearly [263]. Lattice structures applied for temporary bone substitute are required to maintain at least six months load-bearing capacity, whilst the service time should be decades for the permanent bone devices. Fatigue performance and to understand the mechanism of fatigue for lattices are thus vital to ensure the reliability and success of the orthopaedic devices [264]. Besides, considering the biomedical devices application requiring specific density or pore size for cell in-growth, whether the mechanical strength, fatigue life and biological behaviour could be improved is essential to further facilitate osteointegration [265].

The mechanical properties of lattice structures are governed by various factors including geometric design, roughness, microstructure, residual stress and etc., which are in turn influenced by process parameters (laser power, scanning speed, scanning strategies, etc.),

and parent materials [199]. Among these variants, the design of lattice geometry involving struts features and unit cell topology is decisive to determine the final mechanical performances through influencing the stress distribution to the implants.

Given the basic of various lattice design is the different topologic designs of struts, the global macroscopic property of lattice structures is dominated by the combined mechanical behaviour of struts with different angles competing uniaxial or bending stress under load. Build orientation of lattice determines the strut angle and associated mechanical properties of both the quasi-static and fatigue bending behaviour. Pérez et al. reported that lower angle strut of 45˚ withstands a 26.1% higher bending force than the 90˚ strut, as well as an higher fatigue strength of 45˚ improved 40% than 90˚ due to the main load direction is not parallel to the longitudinal axis of the lattices or implants [266]. Hossain et al. found that the strut angle has no significant effect on elastic modulus, but the ultimate tensile strength strongly depends on the struts build angle, the vertically built strut are stronger than the low angle struts [213]. On the contrast, Murchio et al. proposed that there is no clear effect of strut angle on the tensile properties, while the fatigue life of vertical and 45˚ struts are higher than that of low angle struts [207]. Build orientation influences mechanical properties through the defects and morphology formed during processing. Dallago et al. reported that the struts features are significantly affected by build orientation, fatigue strength can be promoted by the altering of the build direction and the topology of the nodes [267]. They also reported that the fatigue failure sites occurring at the struts, or the nodes are governed by the struts angle. Wauthle et al. observed that the 45˚ build lattice has 35% less compressive strength and stiffness than that build vertically [126]. These findings all highlights the importance of exploring

proper selection of unit cell orientation and strut angle, which intensively impacting the mechanical properties of biomedical implants.

Unit cell orientation influences the anisotropic or isotropic mechanical property, stiffness, strength, and fatigue by changing the stress fields within lattice struts. Hence, research on unit cell orientation with respect to the load direction can provide pathway to satisfy required needs such as tailoring the elastic modulus of mimicking bone to avoid stress-shielding effect, especially under complex loading conditions [44]. Weissmann et al. studied the unit cell with 0˚, 45˚ and 90˚ orientations, indicating that the 0˚ orientated lattice performed outstanding elastic modulus and compressive strength compared to higher orientation angle [268]. Attributing to the struts within zero-degree orientated lattice undertaking load vertically, and the uniform angle of struts share the identical force direction. As the unit cell orientation increases, the stiffness decreased significantly due to the changing angle of struts, where the strain accumulates in the scaffold with a deterioration of the strut position. Cuadrado et al. compared the cubic, cross (cubic unit cell 45˚ orientated), and BCC structure [269]. Cubic lattice structure performed the ~4-fold higher elastic modulus and compressive strength than BCC and cross structures. They concluded that due to the struts in cubic lattice are parallel to the load direction, the main deformation in these struts is compression rather than bending, which has higher bearing ability. For BCC and cross lattices, the inclined angle between angle and load direction causes a bending-dominated deformation behaviour.

In addition to the mechanical properties, biological response on the PBF-LB lattice structures is one of the ultimate aims to ensure the stability and effectiveness of implants.

The biological response mainly relies on the surface topology and chemistry. It has been widely studied that the surface quality largely depends on the build orientation of struts. Lerebours et al. proposed that the two main surface morphology including micro-grooved, and the semi-molten powders have inverse effect on cell adhesion [270]. Where upper surface dominated by the micro-grooves is preferred for mammalian cells rather the lower surface covered by partially melted powders.

Obviously, optimising the structural design along the loading direction enables the potential enhancement of mechanical strength and biological property via unit cell orientation. Aforementioned works highlight the importance of exploring the lattice features, including strut angle, unit cell orientation, to improve the mechanical and biological performances of meta-biomaterials. Regardless of the great efforts contributing to the lattice geometric design, mechanical properties, and biological response, there is a need to link and integrated all the main properties of lattices after applying for biomedical implants. The effects of strut angle and unit cell orientation on lattice performance were evaluated independently and collaboratively. Herein, three different rotation strategies were investigated and the behaviour of lattices under quasi-static compression, fatigue loading, and in-vitro were assessed. With the purpose of improving the predictability and control of lattices applied for healthcare, FEA analysis and microstructure were investigated to understand the mechanism of the effect of rotation strategies.

6.2 Method

6.2.1 Lattice Manufacture

Uniform unit cell of BCC lattice structure consisted of unit cell size of 2 mm and strut thickness of 450 μm (fig. 6.1 (a)) was used as basic geometry for the following structural design via rotation strategies. Specific variations are as follows, and illustration of rotation and tilting of lattices is showed in **Appendix B.3**:

1) Changing strut build orientation (SO) through varying build direction (BD) 45˚ of lattice structure to cover a low and high strut angle of 9.4˚ and a high strut angle of 80.6˚, named as SO45 in fig. 6.1 (b). The SO45 lattice is firstly rotated 45˚ around z-axis, then titled 45˚ along y-axis [112]; The SO45 and Default BCC shares the same unit cell orientation.

2) Both struts and unit cell orientation are 45˚ (SOUO45) varied, which is applied the same rotation and titling strategy as SO45 (fig. 6.1 (c)). While the unit cell orientation of SOUO45 is 45˚ rotated with respect to the loading direction;

3) Unit cell orientation (UO) was built as the Default BCC lattice without strut angle changing, the unit cell orientated 45˚ (UO45) with respect to the load direction as shown in fig. 6.1 (d).

Cylindric specimens including default BCC, SO45, SOUO45, and UO45 lattices were designed in the nTopology (version 3.35.2, USA) with 15 mm diameter and 20 mm height for mechanical tests, whilst height and diameter 6 mm for *in vitro* biological characterisation. Then design was transformed to STL file before input to the RenAM 500S system (Renishaw, UK). For this PBF-LB process, the Ti-6Al-4V powders (Grade

23) with a size range of 15-53 µm was applied for manufacturing on the 170°C pre-heated substrate. Under the argon atmosphere, each specimen with three replicates were manufactured by uniformly using the previous optimised multi-contour strategy in Chapter 5. Supports for each specimen were added and fabricated with laser power of 150 W, scanning speed 1125 mm/s of point distance 45 µm to exposure time of 40 µs, and contour distance of 0.08 mm.

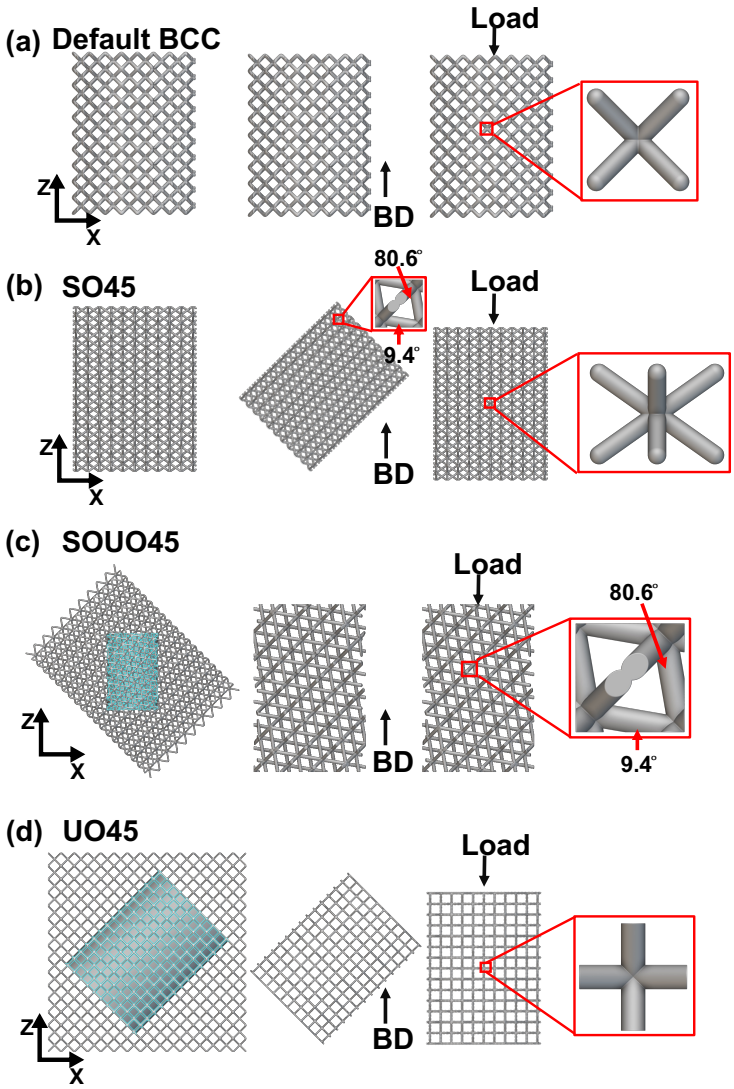

Figure 6.1 Images showing the comparison of (a) default BCC lattice structures, (b) SO45, (c) SOUO45, (d) UO45, with zoomed in unit cell orientation under load direction, and the front view of octahedral lattice structures.

Default BCC (Fig. 6.1 (a)) and SO45 (Fig. 6.1 (b)) structures were compared regarding to the effect of strut build angle, while unit cell orientation effect on mechanical properties was studied by comparing SOUO45 (Fig. 6.1 (c)) and UO45 (Fig. 6.1 (d)). In terms of the combined effect of strut build angle and unit cell orientation, SOUO45 was compared to Default BCC.

6.2.2 Morphology Characterisation and Microstructure Characterisation

Scanning electron microscope (EVO15, ZEISS, Germany) was used under an acceleration voltage of 20 kV and secondary electron mode, to capture the surface morphology of as-built lattices and the fracture surface.

Samples were cut and mounted followed by a standard metallurgic preparation from grinding to a final fine polishing with 30% H_2O_2 activated OP-S (Struers, Denmark). Electron backscattered diffraction (EBSD, Jeol 7000, Japan) was used to detect the crystallographic orientation of grains for the SOUO45 lattices. Maps were created by a step size of 0.45 μm at 10kV.

6.2.3 Mechanical Testing

Uniaxial static compression tests were conducted with a 50 kN load cell of the universal testing machine Z030 (ZwickRoell, United Kingdom) at ambient temperature. Three replicates of each group were tested under 0.5 mm/min constant rate. The Young's modulus was calculated in the linear elastic region from the slope of the stress-strain curve, while the yield strength was obtained at 0.2 % proof stress.

Compression-compression fatigue test was conducted with sinusoidal cycle at 0.1 stress ratio of minimum/maximum stress on dynamic load frame (ElectroForce 3510, TA instruments, USA). A block process was applied to which involved increasing the frequency from 1 Hz to 10 Hz progressively for the initial 200 cycles, then maintaining at 15 Hz for 10^6 cycles. The maximum stress was selected between 10% - 70% of the yield strength from the static compression test of the Default BCC lattice. End criteria of test was set at either survived 10^6 cycles (ran-out) or 90% stiffness reduction while the displacement is 10 times higher of the initial value [271].

6.2.4 FEA simulation

To further investigate the stress distribution in lattices of SOUO45 and UO45 under the compressive loading, finite element models were analysed. 1/8 of the real tested lattice volume was designed in Fusion 360 (v.16.5, Autodesk, USA) and assessed in ABAQUS (Dassault Systems Simulia Corps. USA), while considering the simulation efficiency and demanded accuracy with a total number of 106,351 for elements and 188,521 for nodes. The bottom plate of lattice structure was constrained, whereas a load was acted on the top plate. A total strain of 50% was applied for the models. The tetrahedral mesh type with the size of 0.6 was applied for the 3D lattice model. Young's modulus was set as 114 GPa and 0.33 for Poisson's ratio.

6.2.5 Biological evaluation in-vitro

6.2.5.1 Cell culture

MC3T3 murine pre-osteoblasts of were purchased from the American Type Culture Collection (ATCC, United Kingdom), and passage 16 used throughout this study to test cell adhesion, differentiation and mineralisation. Default BCC and SOUO45 lattices were chosen to study their influence on osteoblast cell response, and three replicates were used for each test. Basal culture media was prepared using minimal essential medium (α-MEM; Sigma-Aldrich, United Kingdom) supplemented with 10% Foetal Bovine Serum, 1% penicillin/streptomycin (Sigma-Aldrich, United Kingdom) and 1% L-glutamine (Sigma-Aldrich, United Kingdom). Mineralisation medium consisted of basal culture media supplemented with 10 mM β-glycerophosphate (Sigma-Aldrich, United Kingdom) and 50 μg/mL L-ascorbic acid (Sigma-Aldrich, United Kingdom).

The lattices were sterilised in 70% ethanol for 24 hours, then washed three times with sterile phosphate buffered saline (PBS, Lonza, United Kingdom) prior to use. MC3T3s labelled with CellTracker^{TM} Green CMFDA (2 μM, Thermo Scientific, United Kingdom) were dynamically seeded onto the lattices as previously described [227]. Briefly, 2 x 10^5 cells were transferred into a sterile 2 ml Eppendorf tubes with a hole pierced in the lid.

The lattices were then placed into each tube and sealed with an AeraSeal™ film membrane (Sigma-Aldrich, United Kingdom) to enable gas exchange. The samples were loaded onto an SB tube rotator (SB3, STUART, United Kingdom) and dynamically cultured for 16 h at 8 rpm (37℃, 5% CO_2). Following which samples were washed twice with basal medium, and cell adhesion assessed under an EVOS fluorescent inverted microscope (EVOS M5000, Invitrogen, USA). Samples were then incubated in mineralisation medium for 21 days with media replaced every two days.

After 21 days of osteoinductive culture, lattices were incubated with basal medium supplemented with CellTracker™ Green CMFDA and Propidium iodide (1 μg/ml in PBS, Sigma-Aldrich, United Kingdom) and incubated for 30 mins in the dark. After washing the lattices twice with basal medium, cells were visualised under an EVOS fluorescent inverted microscope (EVOS M5000, Invitrogen, USA).

6.2.5.2 Alkaline Phosphatase (ALP) Activity

ALP activity was assessed using the 4-nitrophenyl colorimetric phosphate liquid assay (pNPP, Sigma-Aldrich, United Kingdom) as previously described [218]. 10 μL of cell lysate (in 0.1% Triton™ X-100) was combined with 90 μL of pNPP and incubated for 60 min at 37℃ with absorbance at 405 nm read on a SPARK spectrophotometer (TECAN, Switzerland). ALP specific activity of each sample was calculated using total ALP quantity divided by total DNA content and reaction time (μg DNA) [272].

6.2.5.3 DNA content

DNA content was evaluated using the Quant-iT PicoGreen DNA assay (Invitrogen, Life Technologies, United Kingdom) [273]. 10 μL of cell lysate (in 0.1% Triton™ X-100) was added to 90 μL of TE (10 mM Tris-HCl, 1 mM EDTA) buffer. Next, 100 μL of PicoGreen reagent was added to all samples and incubated for 5 min in the dark. The fluorescence was measured in a SPARK spectrophotometer (TECAN, Switzerland) at 480/520 nm wavelength.

6.2.5.4 Collagen Production

Picrosirius red staining was used to assess collagen production as described previously [274]. Lattices were washed twice in PBS and fixed in 10% neutral buffered formalin (NBF, Cellpath, United Kingdom) for 30 min. After fixation, the samples were incubated with Picro-Sirius Red Solution (ScyTek Laboratories, Inc., USA) for 1 h. Following which, samples were washed in 0.5 M acetic acid then distilled water and left to air dry overnight. 0.5 M sodium hydroxide was used to elute the bound picrosirius red dye and absorbance read at 590 nm using a SPARK spectrophotometer (TECAN, Switzerland). Collagen production was normalised with DNA content.

6.2.5.5 Calcium Deposition

Calcium deposition on the lattices was assessed using alizarin red staining [275]. Briefly, lattices were washed twice in PBS and fixed in 10% NBF (Cellpath, United Kingdom) for 30 min. After fixation, lattices were washed in distilled water and then incubated with alizarin red solution (Sigma-Aldrich, United Kingdom) for 10 min and the unbound dye removed by washing in distilled water. To quantify alizarin red staining, stained samples were eluted with 10% cetylpyridinium chloride (Sigma-Aldrich, United Kingdom) for 1 h and then absorbance was read at 550 nm using a SPARK spectrophotometer (TECAN, Switzerland). Calcium content was normalised with DNA content.

6.3 Results

6.3.1 Surface characteristic and deviation

Secondary electron micrographs are presented in fig 6.2 and show typical lattice surface. Surface adhered powder particles dominate the surface morphology. Images in fig. 6.2

(a1) – (d1) showcase that there is less unmelted powder attachment on the top surface of 9.4˚ printed struts in SO45 and SOUO45, compared to the 35.6˚ strut of Default BCC and UO45. In the case of 9.4˚ and 35.6˚ strut, more obvious staircase effect (denoted by red dashed line) occurred compared to higher angle strut of 80.6˚. Bottom surface was covered by unmelted powders across all specimens without showing clearly difference (Fig. 6.2 (a2) – (d2)).

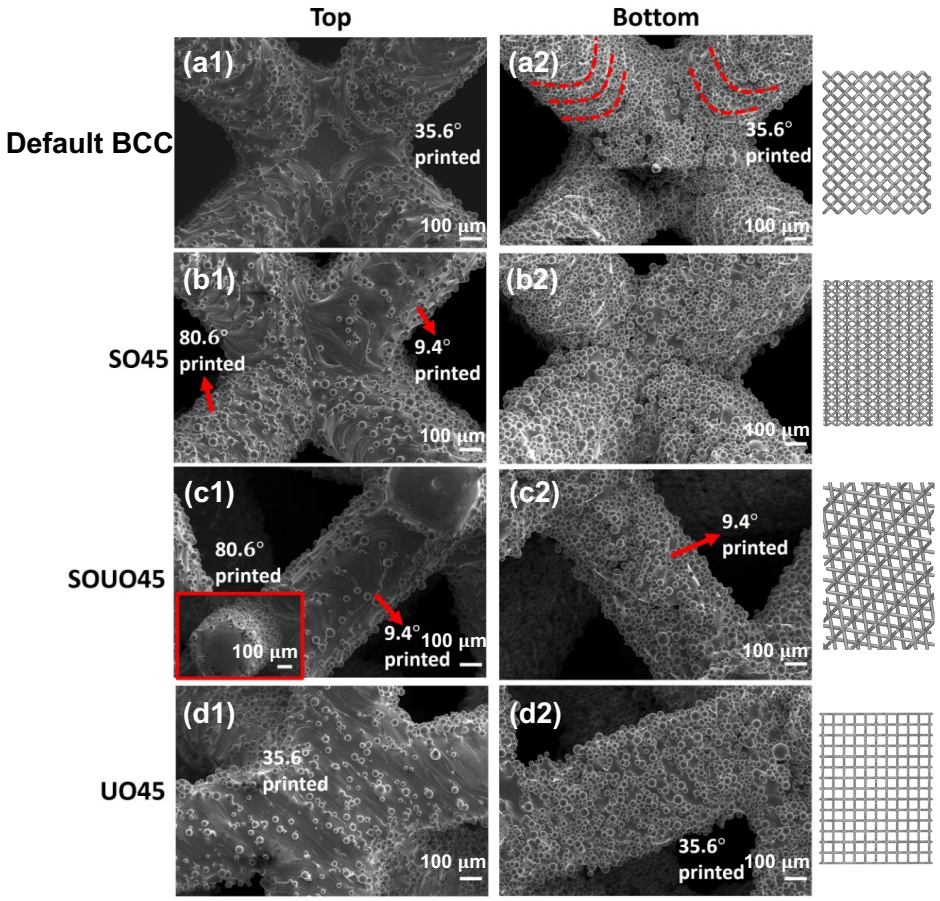

Figure 6.2 SEM images showing the top and bottom surface morphologies of Default BCC in (a1) and (a2), SO45 in (b1) and (b2), SOUO45 in (c1) and (c2), and UO45 in (d1) and (d2) lattices, where red arrows direct different strut angle of 9.4˚, 35.6˚ and 80.6˚ included in lattice structures, red dashed line outlined the staircase effect.

6.3.2 Quasi-static compressive properties

The stress-strain curve of SOUO45 and UO45 in fig. 6.3 (a) tend to overlap in the elastic region, which elastic modulus was measured at 2.09±0.17 GPa and 2.12±0.04 GPa respectively (Fig. 6.3 (b)). Whilst similar stress-strain curve is observed in the Default BCC and SO45 lattices, but significantly ~50% lower modulus than SOUO45 and UO45. No plateau or densification was observed for either Default BCC or SO45 lattices, suggesting rapid mechanical failure process without layer-wisely collapse. Continuous fracture plateau of SOUO45 slightly fluctuated as the strain increases from 0.2 to 0.4. While a ~ 50 MPa stress fluctuation was found in UO45 (Fig. 6.3 (a)). Noticeably, the SOUO45 and UO45 lattices present $p < 0.0001$ significantly higher yield strength of 81.96±4.0 MPa and 83.51±1.45 MPa, and UCS of 107.77±4.0 MPa and 105.86±2.06 MPa than that of Default BCC and SO45 (Fig. 6.3 (b)-(d)).

Photographs in fig. 6.3 (e) – (d) show the deformation behaviour and compressive failure modes for all specimens. Default BCC and SO45 exhibited barrelling after reaching yield strength (Fig. 6.3 (e) & (f)), both showing a 45˚ shear fracture plane along the diagonal direction with the increasing strain. A different deformation behaviour of SOUO45 was shown as buckling from right to the left at the bottom of the part and after strain of 0.2 and collapse of the lower layers (Fig. 6.3 (g)). UO45 lattice displays a contraction deformation towards centre at the strain of 10% (Fig. 6.3 (h)).

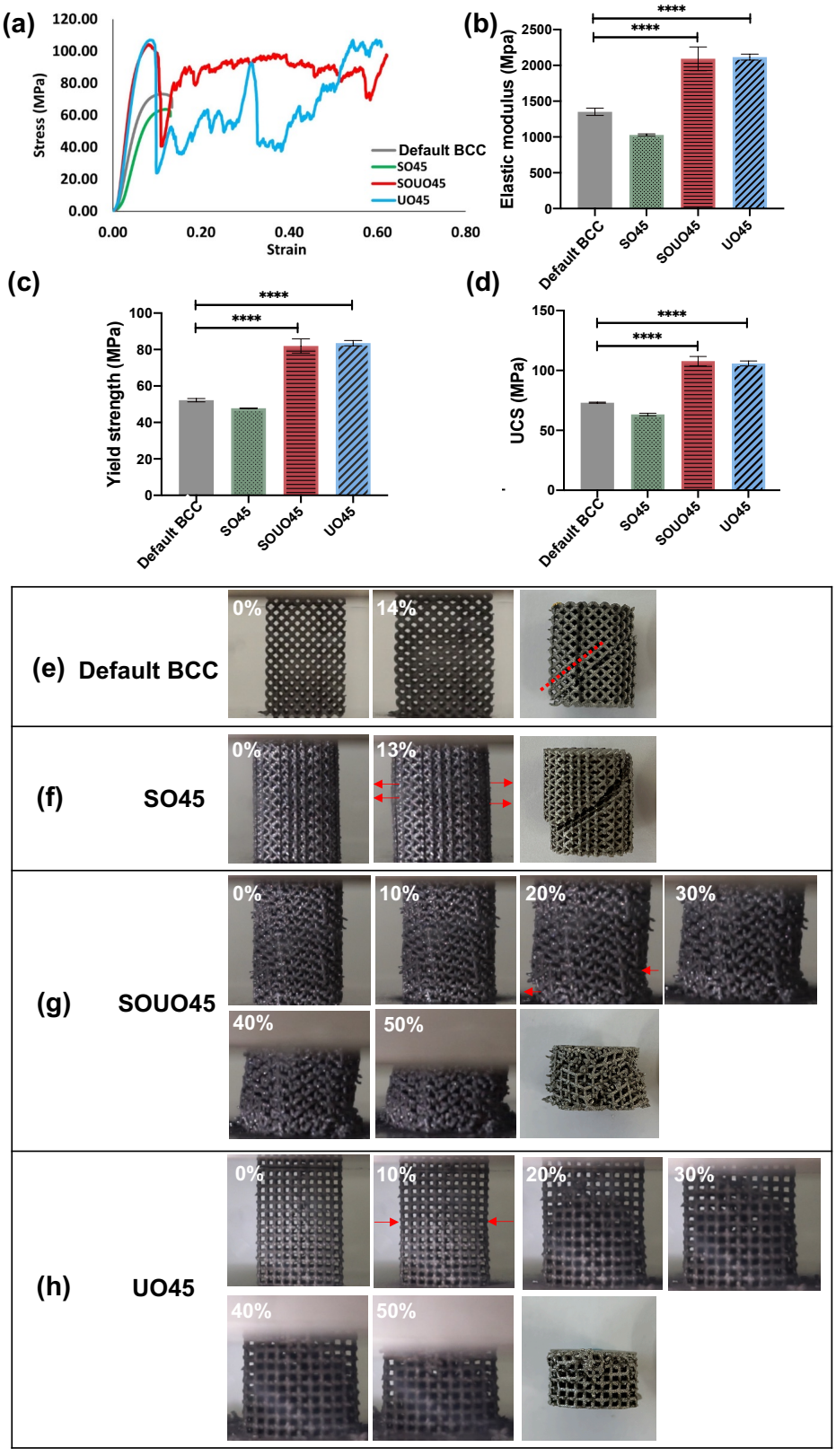

Figure 6.3 (a) The compressive test stress-strain curve, and the results comparison of (b) elastic modulus, (c) yield strength and (d) UCS; the failure mode and fracture collapsing status of (e) Default BCC, (f) SO45, (g) SOUO45, and (h) UO45 lattices, deformation

marked by red arrows, red dashed line outlined the fracture plane (n=3, * signifies p value < 0.05).

6.3.3 Fatigue performances of Default BCC and SOUO45

To explore the effects of both strut and unit cell orientation, SOUO45 was chosen to compare against the Default BCC lattice. Hysteresis curves of Default BCC and SOUO45 are shown in fig. 6.4 (a) and (b) under the stress level of 36.54 MPa. It is obvious that as the cyclic number increases, the hysteresis curves of both Default BCC and SOUO45 gradually move to the right with a larger strain difference comparing to lower cycles of 200^{th} for Default BCC and 1000^{th} - 10000^{th} cycles of SOUO45. This indicates fatigue ratcheting, known as a cyclic creep phenomenon, occurring and accumulating during the dynamic loading process. The strain distance between maximum stress is larger than that of the minimum stress with increasing cycles, which may be due to crack initiation and propagation within individual struts. In general, SOUO45 shows less pronounced ratcheting compared to the Default BCC lattice. The hysteresis curve of SOUO45 is similar until $50{,}000^{th}$ cycles, while the stiffness starts to change below $5{,}000^{th}$ cycles of Default BCC.

Fig. 6.4 (c) and (d) shows the strain accumulation of the Default BCC and SOUO45, where the curve shows the maximum strain of the hysteresis curve under a specific loading level against each cycle. Under the dynamic compressive loading, the plots show that the strain accumulates, supporting the hysteresis curves (Fig. 6.4 (a) and (b)). Strain accumulation has three main stages: strain rising , plateau as stain stabilises, and a dramatic strain increase region. The decreasing of the point of strain demarcation (N_c) of

SOUO45 is ~50% lower for same stress level , suggesting less plastic deformation before the final fatigue failure compared to Default BCC.

Fatigue life for both Default BCC and SOUO45 was influenced by the stress level, where the number of cycles to failure increases with decreasing load. A 75 % improvement for the fatigue life was obtained by SOUO45 lattice, with a fatigue strength of above 20.88 MPa (stress ratio of 0.4) surviving 10^6 cycles loading compared to the Default BCC lattice (5.22 MPa,stress ratio 0.1) (Fig. 6.4 (e)). SOUO45 lattice has a greater resistance to deformation and fatigue life under higher loading level than Default BCC structure. In addition, the fatigue life of SOUO45 gained 76%, 94%, 98%, 97%, 98%, 97% under the stress level of 10.44 - 36.54 MPa showed in fig. 6.4 (f) to the Default BCC lattice.

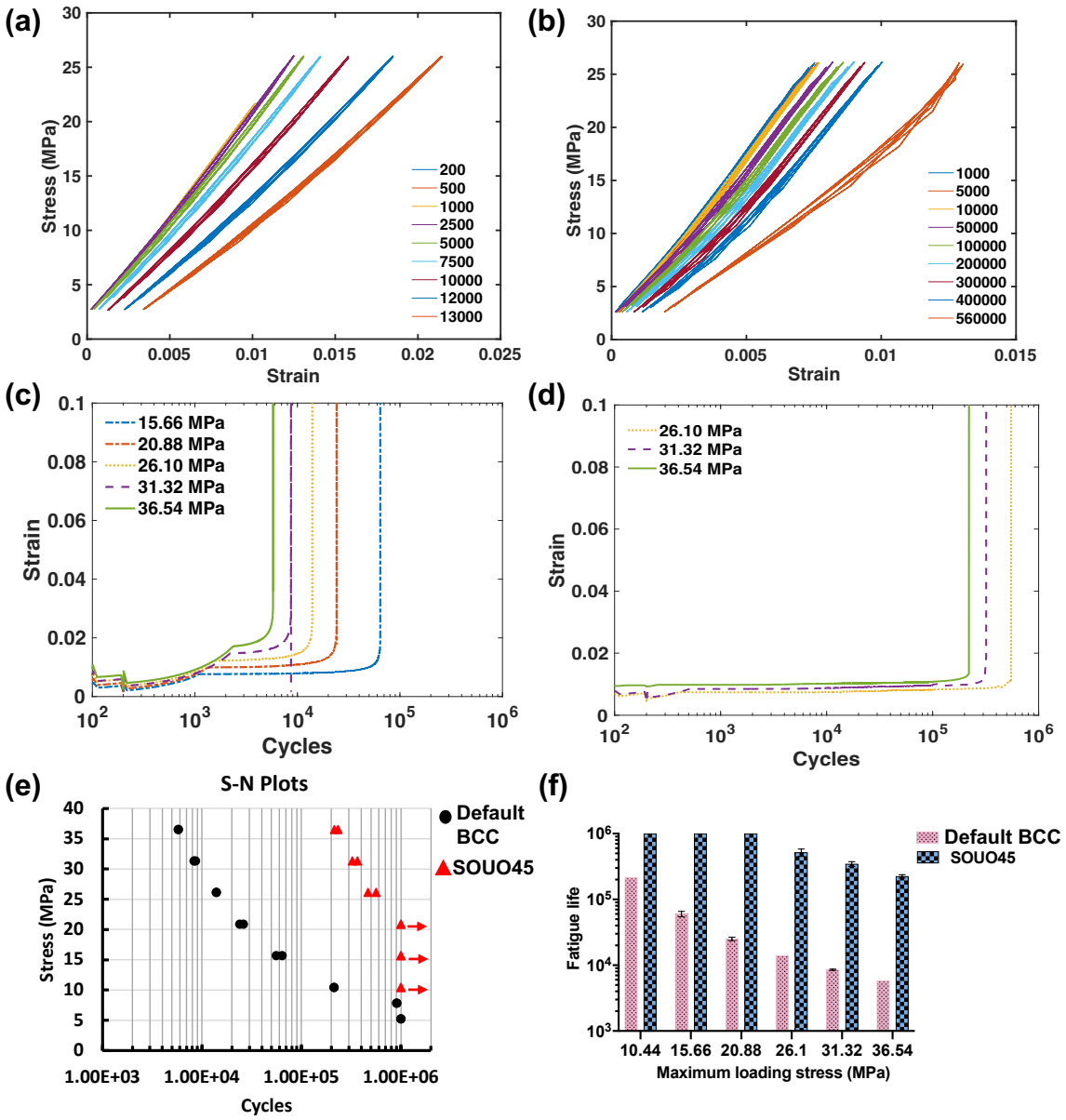

Figure 6.4 The hysteresis curves of (a) Default BCC and (b) SOUO45 lattices during the fatigue test under the maximum load of 36.54 MPa; strain accumulation plot against cycles of (c) Default BCC and (d) SOUO45; (e) S-N plot and (f) comparison of fatigue strength for Default BCC and SOUO45 lattices.

Typically fatigue failure occurs in three stages: crack initiation, crack propagation and growth, and fracture failure. Crack initiation in the lattice was detected near to a node, at a strut intersection (Fig. 6.5 (a)). A single crack split and propagated in two directions along the strut fig. 6.5 (b) and (c) show crack initiation at a surface with extensive particle

adhesion. this could suggest initiation due to both the irregular surface and attached particles creating stress concentration points.

Due to rapid cooling rate, martensite acicular dominates the microstructure of PBF-LB manufactured Ti64 lattices [276]. Crack nucleation slip and growth are along the grains, presenting as transgranular cleavage can be observed in fig. 6.5 (d) and (e). Fatigue striations were observed in the SOUO45 (Fig. 6.5 (f)). These are parallel to each other and elongated along the crack propagation direction. The number of striations should increase with the cyclic loading and further lead to the propagation of cracks. As the cracks initiate and grow, the stiffness of individual struts reduces, and the loading stress is less equally distributed across the structure resulting in more stress concentration. Ultimately this leads to fatigue failure of the whole structure. Dimples were observed in fig. 6.5 (g) and (h) at the fatigue fracture surfaces support this progression, indicating a combined ductile and brittle failure. Moreover, dimples were observed surrounding a pore defect in fig. 6.5 (h), whilst the outer region shows a flat fracture surface with striations generated due to shear force.

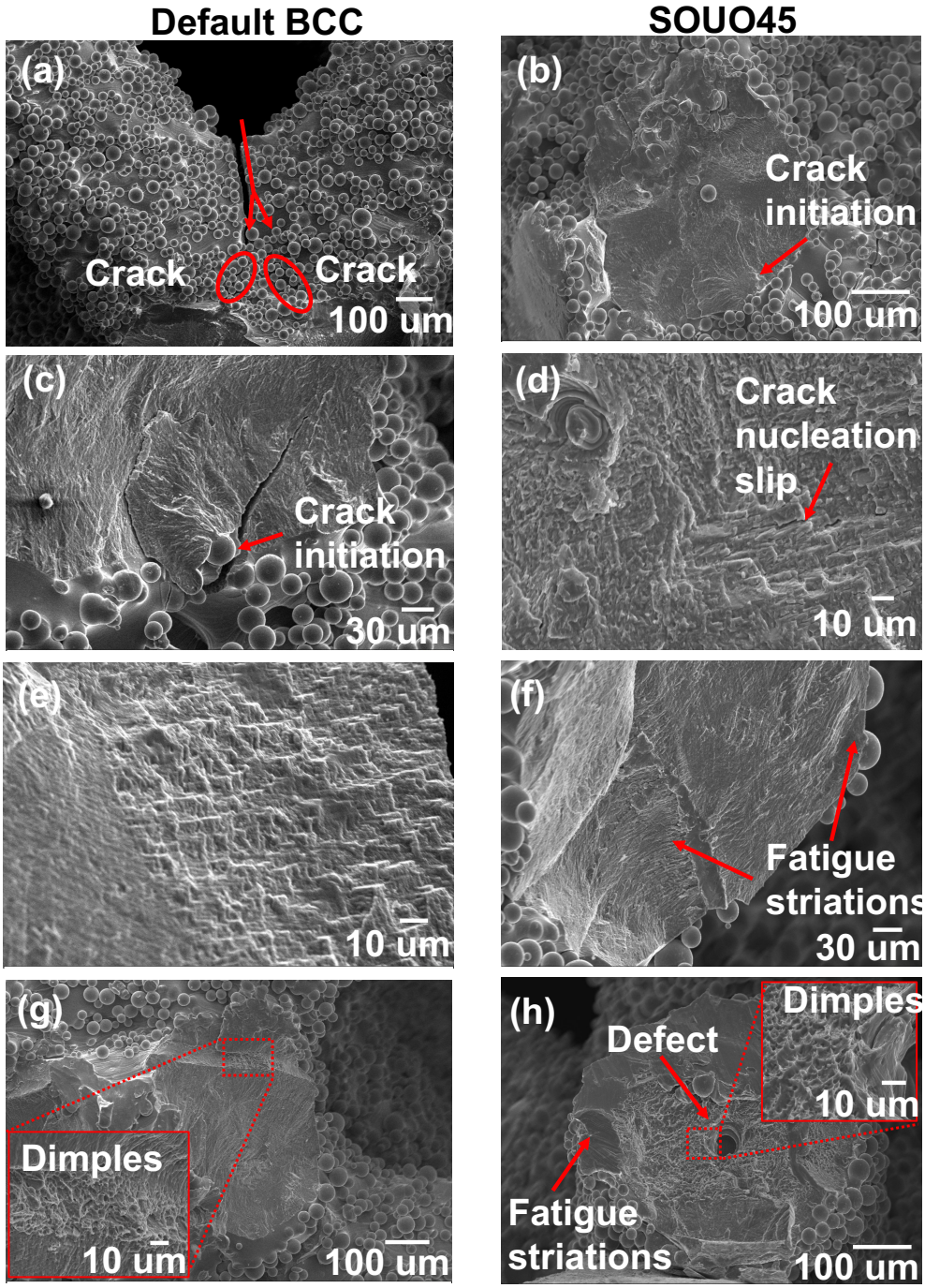

Figure 6.5 The morphology of fracture surface for lattices after fatigue test showing the crack initiation of (a) Default BCC lattice at node, (b) SOUO45 lattice, and (c) Default BCC at powder attached surface; crack propagation for (d) SOUO45 and (e) Default BCC, (f) fatigue striations in SOUO45, final fatigue fracture features for (g) Default BCC and (h) SOUO45 lattices.

6.3.4 Microstructure of low- and high-angle strut of SOUO45 lattices

The EBSD captured microstructural differences in low- and high-angle of SOUO45 lattice struts, as shown in fig. 6.6 (a) for low-angle printed strut, and fig. 6.6 (b) for high-angle strut in SOUO45 lattice structure. Generally, struts present martensite acicular laths typical of PBF-LB Ti64. The grain size for low angle struts is generally larger than that of the high angle struts (Fig. 6.6 (c) & (d)). Pole figures show a random texture of the low angle struts when compared to the strong texture of {0001} α towards the X or Y axis of high angle struts.

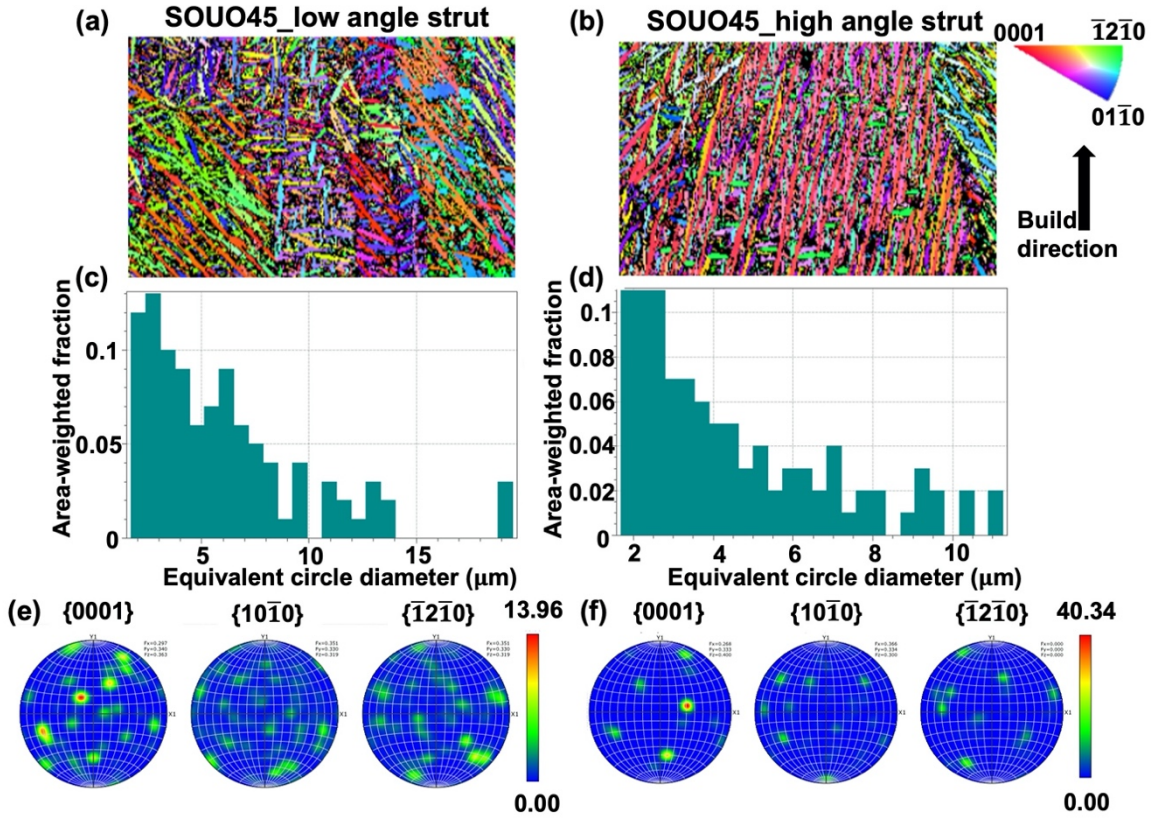

Figure 6.6 EBSD map and the corresponding colour scheme of (a) low angle strut, (b) high angle strut; grain size for (c) low angle strut, (d) high angle strut; pole figures for (e) low angle strut, and (f) high angle strut in SOUO45 lattice along the build direction.

6.3.5 In-vitro MC3T3 response on Default BCC and SOUO45

The influence of the different lattices on cellular adhesion was visualised following dynamic seeding. The fluorescent images show viable cells homogeneously distributed on the top, side and bottom surfaces of the Default BCC and SOUO45 lattices after 24 hours (Fig. 6.7 (a)). After 21 days in osteogenic conditions, there is a clear difference between samples with cells preferentially attached to the rotated lattice fig. 6.7 (c) and (d). SOUO45 with same porosity and unit cell presents an improvement of cell adhesion, especially on the side and bottom surfaces that appear densely covered by MC3T3, while viable cells on the Default BCC sample seem to be fewer than those displayed on the same sample after 1 day of seeding. It should be noticed that cell coverage on both samples after 21 days seem to be dependent on the observed area with the top surface revealing lower cell attachment. This enhanced cell attachment in the rotated samples is confirmed by the significant increase ($p<0.05$) in DNA content in Day 21, suggesting the enhanced capacity of SOUO45 to enable cell-lattice interactions.

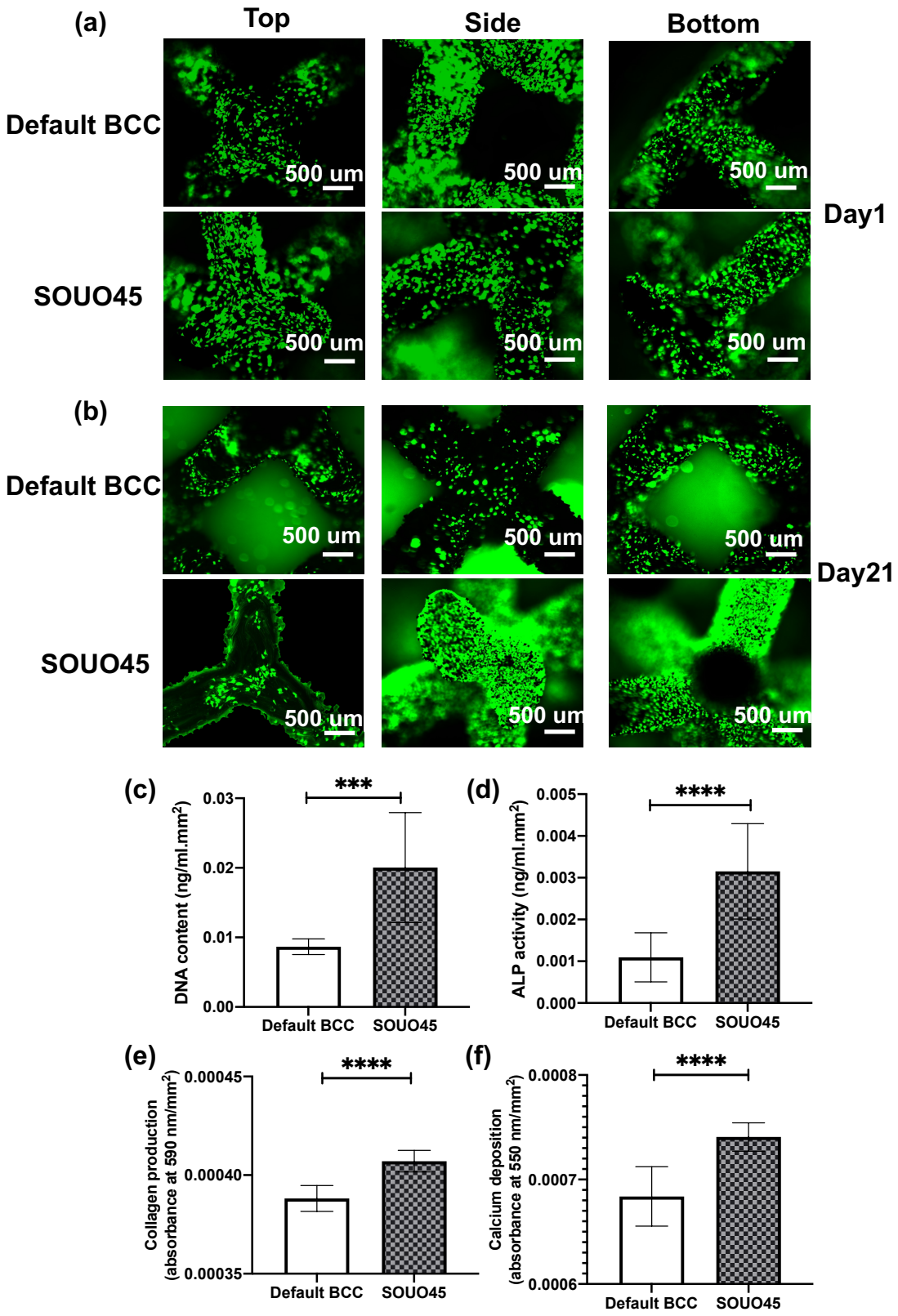

Figure 6.7 Biological interactions of porous lattices with MC3T3 cells including live/dead staining after (a) 1 day and (b) 21 days of culture, (c) DNA content (after day 14 and normalised (d) ALP (after day 14), (e) collagen and (f) calcium deposits after 21 days of

culture, (c) DNA content (after day 14 and normalised (d) ALP (after day 14), (e) collagen and (f) calcium deposits after 21 days respectively (n=3, * signifies p value < 0.05).

Critically, we evaluated the influence of these lattices on MC3T3 osteogenic differentiation and mineralisation by initially quantifying ALP activity. After 14 days of osteogenic culture, the SOUO45 lattices exhibited a three-fold increase in ALP activity when compared to the non-rotated scaffolds ($p<0.0001$) (Fig 6.7 (d)). At day 21, we investigated the influence of these lattice on stimulating MC3T3 extracellular matrix production and mineralisation through quantifying collagen production and calcium deposition respectively. Our findings showed that the SOUO45 lattices exhibited 8% and 5% increase in collagen production and calcium depositions when compared to the default BCC samples after 21 days of osteoinductive culture (Fig 6.7 (e) & (f)). Thus, it seems that design control in the early stages of manufacturing can enhance biological interactions of AM porous structures.

6.4 Discussion

Strut surface is highly influenced by the individual build angle. The low strut angle of 9.4˚ has a smoother upper surface due to less surface for surrounding loose powders to attach initially, and re-melting of the attached powders in the previous melted layers than the high-angle struts of 80.6 in SO45 and SOUO45 lattices (Fig. 6.2). The irregularity and amount of unmelted powder particles on as-built lower surface, resulting from the poor heat conduction originated from the nearly full exposure of lower surface to loose powder particles. These difference in surface finish could further influence mechanical performance and relate to the mammalian cell behaviours as discussed below [277].

The SOUO45 and UO45 lattice showed higher elastic modulus and yield strength compared to the default BCC and SO45 lattices, suggesting unit cell orientation is a governing factor for the elastic anisotropy. This is in line with the finding of Cutolo et al., they concluded that the compression behaviour of diamond lattice is significantly impacted by the unit cell orientation due to the global compressive loads redistributed to local tensile and shear stress [278]. Reflecting that different failure modes are attributed to the reorientation of the stress distribution.

To further explain the different mechanical behaviour observed, FEA analysis was conducted for SOUO45 and UO45 to visualise the stress distribution inside the lattices (Fig. 6.8). The result in fig. 6.8 (a) of Von Mises illustrates that the maximum stress is located at the near node region for both low- and high-angle struts in SOUO45, while the minimum stress (blue) occurs inside the low-angle struts. It is also clear that the high angle struts of 80.6˚ in fig. 6.8 (b) is highly deformed causing the shearing failure mode of SOUO45 is consistent with the observations in fig. 6.3 (g). It can be assumed that lattice interior combined with both low and high-angle struts, stress mainly transmits through nodes to the high-angle struts. The maximum principal stress concentrated near nodes would result in crack formation and propagation during the dynamic loading (Fig. 6.8 (c)). Besides, the maximum negative stress is also observed near nodes, suggesting a combined tensile-compressive stress distribution in the SOUO45 lattice.

Similarly, fig. 6.8 (d) presents a consistent deformation mode reflecting the experimental conditions (Fig. 6.3 (h)), the Von mises stress of UO45 is mainly distributed at the node region (Fig. 6.8 (e)). Comparing to the SOUO45, the maximum principal stress of UO45

is significantly lower (Fig. 6.8 (f)). The free body diagram in fig. 6.8 (g) further illustrates that the high angle struts experience combined compressive stress along the struts and the shear stress. It can also be seen that in fig. 6.8 (c) the red colour representing the tensile stress is in two opposite direction and concentrates on the two ends of the high angle struts.

The analysis in fig. 6.8 (h) also fits with the maximum principal stress distribution in fig. 6.8 (f), where the tensile stress dominants the struts connection region. The failure mode of UO45 can be pictured that for the tensile stress dominated horizontal strut, one end of strut would move towards the interior of the unit cell, while the other end tends to move outward from the centre of unit cell. These stress concentration areas would lead to the mechanical failure, crack initiation and propagation in fatigue test. Both the SOUO45 and UO45 contains the low angle struts inside the lattice geometry, which plays an important role to trade off the stress concentration and redistribute and conduct the stress from the loading direction to the transverse direction.

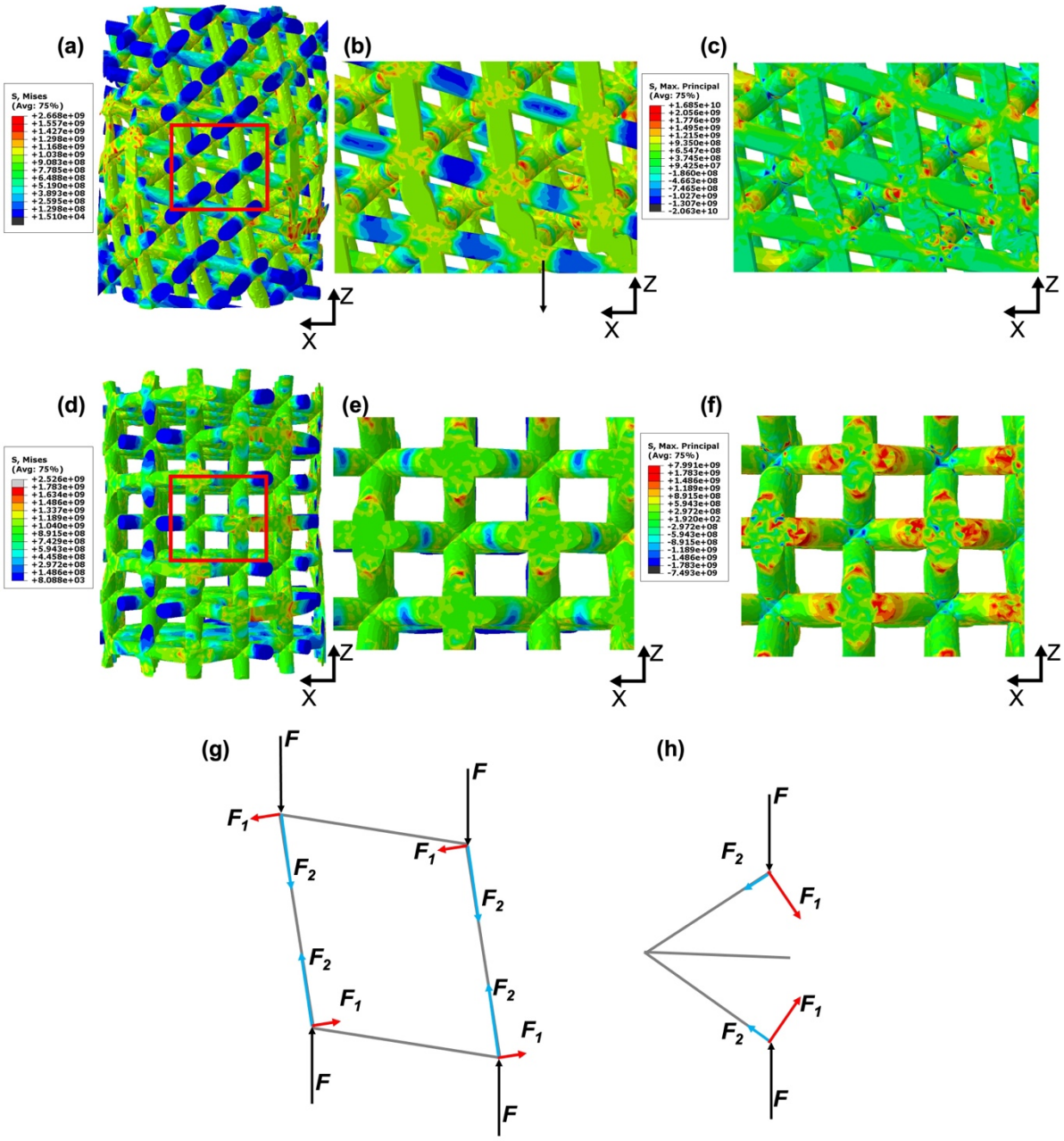

Figure 6.8 FEA analysis showing the Von Mises and maximum principal stress distribution for (a) whole structure, (b) and (c) interior for deformed SOUO45, (d) overview, (e) and (f) sampled from internal of UO45 lattice; free body diagram of (g) SOUO45 and (h) UO45 lattices.

However, the only difference between Default BCC and SO45 lattices is the strut angle during the manufacturing. There is no significant difference for the slip plane of the during the failure of both SO45 and Default BCC, which both appear at 45˚ (Fig. 6.3 (e)

and (f)). Therefore, quasi-static compression fracture behaviour appears unaffected by strut build angle. Yield and compression strength of SO45 is lower than the Default BCC lattice, indicating that the overall yield is influenced by the build angle. Hossain et al. found that the Ti64 lattice mechanical strength highly depend on the strut angles, where the higher strength was observed on high angle struts due to fewer imperfections of the surfaces than lower angle struts [279]. Therefore, it can be concluded that for consistent loading direction towards unit cell and lattice design, it is the surface condition and consequently the individual strut build angle which plays a critical role in mechanical performance.

The crack initiation observed in fig. 6.5 of SOUO45 supported by the FEA results and corresponding free body diagram in fig. 6.8, where the formation of crack is near the node. Due to the topological design, both the dimples and the fatigue striations indicate that the combined effect of tensile stress and shear stress distributed in the lattice [271]. The high angle struts initially show buckling (Fig. 6.8 (a) and (b)), followed by a shear failure, demonstrating a stretching-dominated behaviour. Based on this, the improved resistance to fracture of SOUO45 can be related to the presence of high angle struts. Kang et al. also highlights the effects of ratcheting on fatigue failure [280]. The ratcheting effect is the plastic strain accumulation during the cyclic loading under a specific stress amplitude. The topology of internal struts has been proved to influence the fatigue behaviour through stress redistribution or adjusting the bending/stretching properties. Fatigue ratcheting was reduced with improved fatigue performance as the number of the stretching-dominated struts increased [143]. The mechanism could be attributed to bending deformation largely being avoided to minimise the magnitude of strain amplitude. Additionally, the fatigue

crack growth could be alleviated by the compressive stress dominated component under a buckling deformation, which is observed from the high angle struts in fig. 6.8 (c) [264]. Fatigue ratcheting is also influenced by the ductility of the material, more specifically, more plastic strain can be accumulated due to better ductility. Based on the results of the quasi-static compression tests (Fig. 6.3 (a)), the Default BCC performs a better ductility after yielding than SOUO45, indicating that more plastic accumulation and thus earlier ratcheting effect would occur during the fatigue test in fig. 6.4 (a) and (b).

Fatigue response is also influenced by the surface roughness and internal defects as stress concentration sites leading to the crack initiation [132]. The effect of surface roughness might increase as the stress level increases. In particular, the HCF is more significantly influenced by the surface roughness than low cycle fatigue, due to the continuous intrusion and extrusion interactions for crack nucleation [132]. The effect of surface quality can be observed on both Default BCC and SOUO45 (Fig. 6.5), where the attached particles act as the crack initiation sites.

For high cycle fatigue (HCF), the early-stage crack initiation and propagation takes the majority of the fatigue life. The common plastic slip relating to the microstructure usually initiates the fatigue cracks [281]. Substructures such as BCC and Hexagonal Close Packed (HCP) of materials localise the macro-loaded deformation into the micro slip band resulting in numerous shear deformation [282]. Thus, the fatigue crack generated from the grain boundaries or free surface due to the intrusion-extrusion mechanism [283]. Some of proposed fatigue studies have concluded the importance of microstructures characteristics to the crack propagation [132, 284]. As shown in fig. 6.6 (a) and (b), the

microstructure of Ti64 lattices is dominated by the needle-like martensite due to the rapid cooling rate during the SLM process. In fig. 6.7 (d) and (e), the crack grew along the grains in both non-rotated and SOUO45 lattices. The crack propagate and growth are influenced by the grain boundaries because of the strain localisation. In addition, the grain size was found increasing as the struts getting thicker. Thus, the stress concentration ahead the crack growth is lower due to the larger plastic zone of low angle struts, hindering the crack propagation. Besides, the texture of low angle struts shows less texture preference, illustrating a higher resistance to fatigue crack than that of high angle struts (Fig. 6.6 (e) and (f)).

Due to SOUO45 and default BCC share the same unit cell size (similar porosity), the difference of MC3T3 response mainly relates to surface morphology determined by strut angle. Higher cell adhesion has been quantified in low-angle strut from the previous work, where results of struts built at 20° exhibited a surface topography that facilitated the highest level of cell adhesion (84.3 cells/mm^2) after 24 hrs ($p \leqslant 0.001$) [112]. Similar cell adhesion was observed in the low-angle strut in SOUO45 and default BCC, which aligns with the finding of Villapun et al. where the upper surface of lower-angle PBF-LB part facilitates cell attachment attributing to the surface wettability transformed from hydrophilic (20 coupon angle) to hydrophobic (60 coupon angle) [131]. The underlying mechanism of the transformation is the changes of surface finish due to the severity of attached powder particles influenced by various build angle of PBF-LB part. A massive increasing of live cells in the Day 21 imaging in SOUO45, indicating that the rougher lower surface with more unmelted powders attached could promote further cell proliferation, differentiation, and mineralisation. Studies of Chen et al. support this

phenomena, of which the MC3T3 E1 was found spread and proliferated much denser 90˚ printed discs than 40˚ discs [285]. They demonstrated that the higher roughness due to more powder s attached creates favourable microenvironment to improve cell spreading with more elongated morphology. Both of Villapun et al. and Chen et al. evaluated the upper face of part with a larger volume. This work showed that the low strut angle of lattice compared to high strut angle can potentially achieve promoting cell adhesion on upper surface at the early stage, as well as creating a condition for proliferation and the following cell activities at rougher lower surface.

The discussion demonstrates the anisotropic mechanical properties of lattices is mainly governed by the unit cell orientation, whilst the biological performance depends on the strut angle. These indicate that the potential of further exploitation on PBF build strategy of lattice structures for biomedical applications requiring mechanical strength in specific load direction, as well as ensuring the osseointegration efficiency.

6.5 Conclusion

In this work, lattices with three different rotation strategies involving the strut angle changing, unit cell orientation were designed and manufactured by laser powder bed fusion. Surface morphologies varied with strut angle, which further influenced the mammalian cell response. The unit cell orientation shows a significant effect on both the quasi-static compression and fatigue test, where with the rotation of unit cell, the fatigue life was improved to 98% higher than that of the Default BCC lattice. Moreover, the biological response was enhanced by using the SOUO45 rotation strategy, presenting a $p<0.001$ difference to the structure without rotation. These indicate that the selection of

strut angle, unit cell orientation and the distribution of high and low angle struts can drive the final properties of the lattices as meta-biomaterials. Improved fatigue and compressive strength, as well as cell response indicating the potential use of unit cell orientation and struts angle, such as SOUO45, UO45 or SO45 as a BCC variant, to fulfil specific and/or comprehensive functions in biomedical application.

Chapter 7 CONCLUSIONS AND FUTURE WORK

This Chapter covered the main results and conclusions presented in Chapter 3, 4, 5, & 6. PBF-LB process and lattice design specific for biomedical implants are briefly discussed. Future works are listed given the limitation of this work could have.

7.1 Overall Discussion and Conclusions

The focus of Chapter 3 was to optimize a single contour (SC) scanning strategy capable of manufacturing lattice structures with fine geometries, which was achieved for a minimum strut thickness of 150 µm. A manufacturing accuracy of above 90% was achieved by optimized SC. Notably, it was found that using a laser scanning path comprising of both contour and fill strategies, originally developed for bulk solids, resulted in an inhomogeneous energy input to individual lattice struts. In contrast, SC tends to provide the homogeneity and consistency of laser spot distribution in PBF-LB process making it more suited to lattice manufacturing. Beyond scanning strategy, laser power and scanning speed were adjusted and integrated to energy density as an indicator to enable the precise control of geometric accuracy as well as the internal pore defects. Low laser power (below 50 W) and high scanning speed (above 1000 mm/s) can introduce the lack of fusion defect, whilst the combination of 50 W laser power and 2250 mm/s scanning speed resulted lattice build failures across all thickness dimensions (150 – 350 µm). Process parameters including laser power and scanning speed are imperative to evaluate the parametric effects on lattice porosity, mechanical properties and fatigue

performance. Herein, with the calculated processing window, the PBF-LB manufacturing of fine lattice structures could potentially be predictable and the processing route on lattice structures although the wider adaptability to various PBF-LB system need to be validated.

Alongside the possibility to optimize various PBF-LB processing parameters there is also a myriad of geometrical characteristics that may be tailored for lattice structures. The large combinations of parameters that may be varied across process and geometry may hinder insight into final properties of lattice structures. To aid this bottleneck, a fundamental study focused on optimization of lattice struts was conducted (Chapter 4), which highlighted conflicting parameters for mechanical and biological across a range of strut angle from 20˚ to 90˚. Enhanced biological responses for pre-osteoblast cells seeded on struts produced at angles below 45˚ compared to above 45˚, were observed including greater cell adhesion, faster proliferation and a higher amount of osteogenic differentiation. On the other hand, more inclined struts exhibited more ductile behavior during three-point bending tests compared with struts produced at 20˚. SEM micrographs revealed that the defects formed inside struts due to inappropriate process parameters affect the ductility, driving an early failure during loading. Significant difference in elastic modulus of specimens across all strut angles were found at the minimum or maximum energy density (0.04 J/mm and 0.22 J/mm), illustrating various defect types, including lack of fusion and gas pores that clearly played a key role in mechanical integrity. In contrast, at the energy density of 0.13 J/mm, elastic modulus tends to overlap among all strut angles, all of which exhibited fully dense internal morphology.

Surface roughness were evaluated through both profilometer, and newly developed image analysis method in Chapter 4. Attributing to different strut angles, roughness of the upper and lower surfaces showcases distinct variations. From the perspective of biological response, the overall higher roughness of the lower surface in 20˚ struts show a more positive trend than 45˚ and 70˚ for promoting the cell adhesion and the following production of calcium and collagen. Based on these results, a parameter map of strut angle in a representative BCC structure was proposed to assist the design of lattices intended for use in bone implants. Potential and broader use of the map would allow to tailor the topology via strut angle to achieve desirable mechanical strength and/or biological requirement. Further validation of the map application was conducted in Chapter 6.

Concerns accompanied with the previously discussed multi-strut angle structures raise questions on how to improve the manufacturing quality for lattices with non-uniform elements, as well as how to improve the contour strategy to accommodate the larger-dimension elements. Herein, the multi-contour scanning strategy was studied on regular BCC lattices with larger strut thickness of 450 μm and 80˚ rotated lattices in Chapter 5. The multi-contour strategy is defined as filling the core via “drawing” contour pattern circle-by-circle according to the part cross-section shape. It was found that reducing the distance between adjacent contour path can efficiently improve the surface finish of upper surfaces of lattices, but compromise the manufacturing accuracy (i.e., overbuild of lattice struts) due to higher energy input. Through applying the pre-optimized process parameters with energy density of 0.13 J/mm, the contour distance of 0.08 mm and 0.125 mm were down selected, since minimal internal defects and maximum geometric accuracy were acquired at these combinations. Furthermore, the compressive strength

testing revealed that there was a 17% increase in ductility when using multi-contour (MC) strategy compared to the traditional single contour + filling (SC+F), as well as an equivalent compressive strength to SC+F were obtained by MC. EBSD analysis displays that the α′ martensite dominates all specimens due to the high cooling rate. Without explanation from the microstructural side, the difference in mechanical behavior of lattices produced by MC and SC+F strategies may be attributed to the number of defects.

Sticking to the goal of developing lattices applied for biomedical implants with functions of load bearing and cell response, rotation strategies based on the developed strut angle map were explore in Chapter 6. Three strategies including solely changing strut angle, changing strut angle and unit cell orientation, solely changing unit cell orientation were examined in relation to effects on compressive mechanical response, fatigue behavior and biological response. Strut orientation (SO) lattices showed a similar compressive property to regular BCC structures, while the increasing of both stiffness and yield strength occurred in the strut and unit cell orientation (SOUO), and unit cell orientation (UO) lattices with a build angle of 45˚. SOUO45 lattice consisted of low-angle (9.4˚) and high-angle (80.6˚) struts. The PF of EBSD firstly presents the {0001} orientated towards X or Y axis inside high-angle struts, while α′ grains in low-angle struts is more randomly distributed without showing preferential orientation. The strong textured α′ phase demonstrates a higher mechanical strength but lower ductility during compressive loading. Fatigue experiments of SOUO lattice showcase an 98% improvement compared to the regular BCC structure. The main mechanism of fatigue failure in SOUO and regular BCC lattices is the fatigue ratcheting, where the plastic strain accumulates as the number of cycle increases. Notably, the rough surface finish inherent in as-printed PBF-LB parts

due to partially adhered powder particles is known to be a contributor to crack initiation. This was confirmed in the present study using SEM, which revealed the crack initiation site to be co-located at the edge of these surface adhered particles. FEA simulations were used to explore expected stress distributions, which were found to be concentrated at the end of struts close to nodes, consistent with the fracture morphology observed. Due to the presence of low-angle struts, the SOUO lattice exhibited improved pre-osteoblast cell adhesion, proliferation and differentiation compared to regular BCC lattices.

7.2 Future Work

Multi-contour has potentially provided an in-process solution to alter the microstructure associating with mechanical properties. This could enable fabrication of lattice structures possessing suitable mechanical performance in the as-built state, theoretically to save time and cost for production and post-process. However, the MC strategy and numerous ideas of in-process optimization need to be further investigated as well as their effect throughout the part as the geometry changes during PBF-LB process.

To build on the fatigue analysis conducted in Chapter 6, it would add value to local variation in residual stress, which may help to further contextualize these findings. This may be of particular utility for orthopedic devices given their relatively long residence times within patients. Notably, limited work has been done on the effect of scanning strategy and geometric structures on residual stress of lattices. The use of high-energy synchrotron X-Ray facilities would be a feasible route to exploring residual stress distribution within a lattice structure.

Wider exploration on lattice topology that improving mechanical properties, fatigue in particular are still needed for load-bearing devices. Functionally lattices have shown great potential in this work through tailoring the struts angle and unit cell, fully using the strut angle parameter map for further advantages of lattices in biomedical and other engineering filed can be attractive.

More in-vitro and in-vivo tests, as well as follow-up of patients will be needed to ensure the feasibility of well-designed implants. Most of the lattice designs as meta-biomaterials are still in a conceptual status with lab-based validation. It would be necessary to collect and assess the practical data for future development of PBF-LB processed implants. Furthermore, it is essential to establish uniform standards and regulations to facilitate the standardized manufacturing of lattice structures.

Accuracy of FEA simulation considering actual built quality of lattices should be further improved. Factors such as features of customized implants, microstructure, residual stress, physiological environment conditions (e.g. pH and temperature), body fluid dynamic and etc. are suggested to be taken into account. Selection of factors may vary according to various application, the complexity of amounts of lattice structures tend to stress the computation efficiency. Therefore, simplified but high-fidelity model will be ideal.

To further discuss the impact of PBF-LB process parameters in lattice structures, in-situ process monitoring would be helpful to visualize the real melt pool behaviour and understand the 'black box', and interaction between laser and powder bed while varying laser power and scanning speed. Applying this technology and dataset to gain an 'in-between' view and generate reliable models for predicting the biomedical related quality of lattice structures can be an innovative tool.

7.3 Final remarks

Studies in this thesis have covered the exploitation of PBF-LB process specific for the fabrication of lattice structures, and the accomplishment of comprehensive function required for implementation in skeletal implants. Future work has been listed considering the limitations of this work, and challenges of PBF-LB, lattice structures, and biomedical applications. To overcome these challenges, AM engineers, material scientists, and clinicians are encouraged to contribute to this topic together, and nourishing the development of healthcare and AM techniques.

Reference

[1] W.H. Organization, Ageing and health, 2022. https://www.who.int/news-room/fact-sheets/detail/ageing-and-health.

[2] N.E.C.a. contributors, National Joint Registry 20th Annual Report, National Joint Registry, 2023.

[3] Z.R. Mi, Shuib, S., Hassan, A. Y., Shorki, A. A., & Ibrahim, M. M, Problem of stress shielding and improvement to the hip Implat designs: A review, J. Med. Sci 7(3) (2007) 460-467.

[4] K. Barri, Q. Zhang, I. Swink, Y. Aucie, K. Holmberg, R. Sauber, D.T. Altman, B.C. Cheng, Z.L. Wang, A.H. Alavi, Patient-Specific Self-Powered Metamaterial Implants for Detecting Bone Healing Progress, Advanced Functional Materials 32(32) (2022).

[5] M. Kaur, K. Singh, Review on titanium and titanium based alloys as biomaterials for orthopaedic applications, Mater Sci Eng C Mater Biol Appl 102 (2019) 844-862.

[6] A.A. Zadpoor, Mechanical performance of additively manufactured meta-biomaterials, Acta Biomater 85 (2019) 41-59.

[7] P. Jiao, J. Mueller, J.R. Raney, X.R. Zheng, A.H. Alavi, Mechanical metamaterials and beyond, Nat Commun 14(1) (2023) 6004.

[8] J.Y. Rho, L. Kuhn-Spearing, P. Zioupos, Mechanical properties and the hierarchical structure of bone, Med Eng Phys 20(2) (1998) 92-102.

[9] E.F. Morgan, G.U. Unnikrisnan, A.I. Hussein, Bone Mechanical Properties in Healthy and Diseased States, Annu Rev Biomed Eng 20 (2018) 119-143.

[10] D.B. Burr, O. Akkus, Bone Morphology and Organization, Basic and Applied Bone Biology2014, pp. 3-25.

[11] N. Koju, S. Niraula, B. Fotovvati, Additively Manufactured Porous Ti6Al4V for Bone Implants: A Review, Metals 12(4) (2022).

[12] M.S. Ghiasi, J. Chen, A. Vaziri, E.K. Rodriguez, A. Nazarian, Bone fracture healing in mechanobiological modeling: A review of principles and methods, Bone Rep 6 (2017) 87-100.

[13] C.S. Bahney, R.L. Zondervan, P. Allison, A. Theologis, J.W. Ashley, J. Ahn, T. Miclau, R.S. Marcucio, K.D. Hankenson, Cellular biology of fracture healing, Journal of Orthopaedic Research 37(1) (2018) 35-50.

[14] D. Savio, A. Bagno, When the Total Hip Replacement Fails: A Review on the Stress-Shielding Effect, Processes 10(3) (2022).

[15] A. Chmielewska, D. Dean, The role of stiffness-matching in avoiding stress shielding-induced bone loss and stress concentration-induced skeletal reconstruction device failure, Acta Biomater 173 (2024) 51-65.

[16] V.I. Sikavitsas, J.S. Temenoff, A.G. Mikos, Biomaterials and bone mechanotransduction, Biomaterials 22(19) (2001) 2581-93.

[17] R.K. Fuchs, S.J. Warden, C.H. Turner, Bone anatomy, physiology and adaptation to mechanical loading, Bone Repair Biomaterials2009, pp. 25-68.

[18] M. Burke, S. Goodman, Failure mechanisms in joint replacement, Joint Replacement Technology2008, pp. 264-285.

[19] A. Goharian, Conception of Osseointegration in Development of Orthopedic Implant Industry, Osseointegration of Orthopaedic Implants2019, pp. 163-183.

[20] D.R. Sumner, Long-term implant fixation and stress-shielding in total hip replacement, J Biomech 48(5) (2015) 797-800.

[21] Q.H. Zhang, A. Cossey, J. Tong, Stress shielding in periprosthetic bone following a total knee replacement: Effects of implant material, design and alignment, Med Eng Phys 38(12) (2016) 1481-1488.

[22] J.R. Martin, C.D. Watts, D.L. Levy, R.H. Kim, Medial Tibial Stress Shielding: A Limitation of Cobalt Chromium Tibial Baseplates, J Arthroplasty 32(2) (2017) 558-562.

[23] J. Nagels, M. Stokdijk, P.M. Rozing, Stress shielding and bone resorption in shoulder arthroplasty, J Shoulder Elbow Surg 12(1) (2003) 35-9.

[24] I.F. P.C. McAFEE, C.E. Sutterlin, K.R. Gurr, K.E. Warden, B.W. Cunningham, The effect of spinal implant rigidity on vertebral, Spine 16 (1991) 190-197.

[25] M.T. Andani, N. Shayesteh Moghaddam, C. Haberland, D. Dean, M.J. Miller, M. Elahinia, Metals for bone implants. Part 1. Powder metallurgy and implant rendering, Acta Biomater 10(10) (2014) 4058-70.

[26] Orthopaedic Devices Market Size By Product (Accessories and Surgical Devices), By Application (Hip Orthopedic Devices, Joint Reconstruction, Knee Orthopedic Devices, Spine Orthopedic Devices, Trauma Fixation Devices, Dental Orthopedic Devices, and Others), Global Industry Analysis, Share, Growth, Trends, and Forecast 2022 to 2030, 2022. https://www.thebrainyinsights.com/report/orthopaedic-devices-market-13035.

[27] Global Orthopedic Surgery Market Report, 2017 to 2022 - Procedure Volume Trends by Type, Country, and Region, 2019. https://www.globenewswire.com/news-release/2019/08/13/1901268/0/en/Global-Orthopedic-Surgery-Market-Report-2017-to-2022-Procedure-Volume-Trends-by-Type-Country-and-Region.html.

[28] G.D. Revankar, R. Shetty, S.S. Rao, V.N. Gaitonde, Wear resistance enhancement of titanium alloy (Ti–6Al–4V) by ball burnishing process, Journal of Materials Research and Technology 6(1) (2017) 13-32.

[29] Y.H. Kim, M. Choi, J.W. Kim, Are titanium implants actually safe for magnetic resonance imaging examinations?, Arch Plast Surg 46(1) (2019) 96-97.

[30] A. Szczes, L. Holysz, E. Chibowski, Synthesis of hydroxyapatite for biomedical applications, Adv Colloid Interface Sci 249 (2017) 321-330.

[31] M. Rizwan, M. Hamdi, W.J. Basirun, Bioglass(R) 45S5-based composites for bone tissue engineering and functional applications, J Biomed Mater Res A 105(11) (2017) 3197-3223.

[32] K.P. Parate, N. Naranje, R. Vishnani, P. Paul, Polyetheretherketone Material in Dentistry, Cureus 15(10) (2023) e46485.

[33] A.N. Aufa, M.Z. Hassan, Z. Ismail, Recent advances in Ti-6Al-4V additively manufactured by selective laser melting for biomedical implants: Prospect development, Journal of Alloys and Compounds 896 (2022).

[34] J. W. Nicholson, Titanium Alloys for Dental Implants: A Review, Prosthesis 2(2) (2020) 100-116.

[35] E. Marin, A. Lanzutti, Biomedical Applications of Titanium Alloys: A Comprehensive Review, Materials (Basel) 17(1) (2023).

[36] M.N. Mohamed Abdel-Hady Gepreel, Biocompatibility of Ti-alloys for long-term implantation, Journal of the mechanical behavior of biomedical materials 20 (2013) 407-415.

[37] L. Bai, C. Gong, X. Chen, Y. Sun, J. Zhang, L. Cai, S. Zhu, S.Q. Xie, Additive Manufacturing of Customized Metallic Orthopedic Implants: Materials, Structures, and Surface Modifications, Metals 9(9) (2019).

[38] C. Yan, L. Hao, A. Hussein, S.L. Bubb, P. Young, D. Raymont, Evaluation of light-weight AlSi10Mg periodic cellular lattice structures fabricated via direct metal laser sintering, Journal of Materials Processing Technology 214(4) (2014) 856-864.

[39] M. Sarraf, E. Rezvani Ghomi, S. Alipour, S. Ramakrishna, N. Liana Sukiman, A state-of-the-art review of the fabrication and characteristics of titanium and its alloys for biomedical applications, Biodes Manuf (2021) 1-25.

[40] H. Shipley, D. McDonnell, M. Culleton, R. Coull, R. Lupoi, G. O'Donnell, D. Trimble, Optimisation of process parameters to address fundamental challenges during selective laser melting of Ti-6Al-4V: A review, International Journal of Machine Tools & Manufacture 128 (2018) 1-20.

[41] F. Trevisan, F. Calignano, M. Lorusso, J. Pakkanen, A. Aversa, E.P. Ambrosio, M. Lombardi, P. Fino, D. Manfredi, On the Selective Laser Melting (SLM) of the AlSi10Mg Alloy: Process, Microstructure, and Mechanical Properties, Materials (Basel) 10(1) (2017).

[42] L.J. Gibson, Modelling the mechanical behavior of cellular materials, Materials Science and Engineering: A 110 (1989) 1-36.

[43] C. Pan, Y. Han, J. Lu, Design and Optimization of Lattice Structures: A Review, Applied Sciences 10(18) (2020).

[44] R. Liu, W. Chen, J. Zhao, A Review on Factors Affecting the Mechanical Properties of Additively-Manufactured Lattice Structures, Journal of Materials Engineering and Performance 33(10) (2023) 4685-4711.

[45] S. Babaee, J. Shim, J.C. Weaver, E.R. Chen, N. Patel, K. Bertoldi, 3D soft metamaterials with negative Poisson's ratio, Adv Mater 25(36) (2013) 5044-9.

[46] E.B. Duoss, T.H. Weisgraber, K. Hearon, C. Zhu, W. Small, T.R. Metz, J.J. Vericella, H.D. Barth, J.D. Kuntz, R.S. Maxwell, C.M. Spadaccini, T.S. Wilson, Three-Dimensional Printing of Elastomeric, Cellular Architectures with Negative Stiffness, Advanced Functional Materials 24(31) (2014) 4905-4913.

[47] J.N. Grima, D. Attard, R. Caruana-Gauci, R. Gatt, Negative linear compressibility of hexagonal honeycombs and related systems, Scripta Materialia 65(7) (2011) 565-568.

[48] Q. Wang, J.A. Jackson, Q. Ge, J.B. Hopkins, C.M. Spadaccini, N.X. Fang, Lightweight Mechanical Metamaterials with Tunable Negative Thermal Expansion, Phys Rev Lett 117(17) (2016) 175901.

[49] X. Zheng, H. Lee, T.H. Weisgraber, M. Shusteff, J. DeOtte, E.B. Duoss, J.D. Kuntz, M.M. Biener, Q. Ge, J.A. Jackson, S.O. Kucheyev, N.X. Fang, C.M. Spadaccini, Ultralight, ultrastiff mechanical metamaterials, Science 344(6190) (2014) 1373-7.

[50] P. Köhnen, C. Haase, J. Bültmann, S. Ziegler, J.H. Schleifenbaum, W. Bleck, Mechanical properties and deformation behavior of additively manufactured lattice structures of stainless steel, Materials & Design 145 (2018) 205-217.

[51] L.J. Gibson, Cellular Solids, MRS Bulletin 28(4) (2011) 270-274.

[52] E. Cetin, C. Baykasoğlu, Energy absorption of thin-walled tubes enhanced by lattice structures, International Journal of Mechanical Sciences 157-158 (2019) 471-484.

[53] H. Lei, C. Li, J. Meng, H. Zhou, Y. Liu, X. Zhang, P. Wang, D. Fang, Evaluation of compressive properties of SLM-fabricated multi-layer lattice structures by experimental test and μ-CT-based finite element analysis, Materials & Design 169 (2019).

[54] C.L. Hongshuai Lei, Jinxin Meng, Hao Zhou, Yabo Liu, Xiaoyu Zhang, Panding Wang, Daining Fang, Evaluation of compressive properties of SLM-fabricated multi-layer lattice structures by experimental test and μ-CT-based finite element analysis, Materials and Design (2019).

[55] G.N. Labeas, M.M. Sunaric, Investigation on the Static Response and Failure Process of Metallic Open Lattice Cellular Structures, Strain 46(2) (2010) 195-204.

[56] T. Zhong, K. He, H. Li, L. Yang, Mechanical properties of lightweight 316L stainless steel lattice structures fabricated by selective laser melting, Materials & Design 181 (2019).

[57] T. Tancogne-Dejean, D. Mohr, Elastically-isotropic truss lattice materials of reduced plastic anisotropy, International Journal of Solids and Structures 138 (2018) 24-39.

[58] M. Leary, M. Mazur, H. Williams, E. Yang, A. Alghamdi, B. Lozanovski, X. Zhang, D. Shidid, L. Farahbod-Sternahl, G. Witt, I. Kelbassa, P. Choong, M. Qian, M. Brandt, Inconel 625 lattice structures manufactured by selective laser melting (SLM): Mechanical properties, deformation and failure modes, Materials & Design 157 (2018) 179-199.

[59] Z. Xiao, Y. Yang, R. Xiao, Y. Bai, C. Song, D. Wang, Evaluation of topology-optimized lattice structures manufactured via selective laser melting, Materials & Design 143 (2018) 27-37.

[60] B. Bahrami Babamiri, H. Askari, K. Hazeli, Deformation mechanisms and post-yielding behavior of additively manufactured lattice structures, Materials & Design 188 (2020).

[61] X. Yan, Q. Li, S. Yin, Z. Chen, R. Jenkins, C. Chen, J. Wang, W. Ma, R. Bolot, R. Lupoi, Z. Ren, H. Liao, M. Liu, Mechanical and in vitro study of an isotropic Ti6Al4V lattice structure fabricated using selective laser melting, Journal of Alloys and Compounds 782 (2019) 209-223.

[62] N. Shivakumar, T. Ramesh, S. Muthukumaran, A short review of molecularly inspired strut-based metal lattice structures, Materials Today: Proceedings (2024).

[63] B. Zhang, X. Pei, C. Zhou, Y. Fan, Q. Jiang, A. Ronca, U. D'Amora, Y. Chen, H. Li, Y. Sun, X. Zhang, The biomimetic design and 3D printing of customized mechanical properties porous Ti6Al4V scaffold for load-bearing bone reconstruction, Materials & Design 152 (2018) 30-39.

[64] F. Deng, L. Liu, Z. Li, J. Liu, 3D printed Ti6Al4V bone scaffolds with different pore structure effects on bone ingrowth, J Biol Eng 15(1) (2021) 4.

[65] C. Wang, J. Wu, L. Liu, D. Xu, Y. Liu, S. Li, W. Hou, J. Wang, X. Chen, L. Sheng, H. Lin, D. Yu, Improving osteoinduction and osteogenesis of Ti6Al4V alloy porous scaffold by regulating the pore structure, Front Chem 11 (2023) 1190630.

[66] Z. Chen, X. Yan, S. Yin, L. Liu, X. Liu, G. Zhao, W. Ma, W. Qi, Z. Ren, H. Liao, M. Liu, D. Cai, H. Fang, Influence of the pore size and porosity of selective laser melted Ti6Al4V ELI porous scaffold on cell proliferation, osteogenesis and bone ingrowth, Mater Sci Eng C Mater Biol Appl 106 (2020) 110289.

[67] K.D. Traxel, C. Groden, J. Valladares, A. Bandyopadhyay, Mechanical properties of additively manufactured variable lattice structures of Ti6Al4V, Mater Sci Eng A Struct Mater 809 (2021).

[68] B. Yao, Z. Zhang, Z. Li, M. Liu, H. Li, J. Zhu, T. Wen, Y. Qi, Compressive properties and energy absorption of selective laser melting formed Ti-6Al-4V porous radial gradient scaffold, Powder Technology 442 (2024).

[69] M. Araya, M. Jaskari, T. Rautio, T. Guillén, A. Järvenpää, Assessing the compressive and tensile properties of TPMS-Gyroid and stochastic Ti64 lattice structures: A study on laser powder bed fusion manufacturing for biomedical implants, Journal of Science: Advanced Materials and Devices 9(1) (2024).

[70] I.A.J. van Hengel, M. Riool, L.E. Fratila-Apachitei, J. Witte-Bouma, E. Farrell, A.A. Zadpoor, S.A.J. Zaat, I. Apachitei, Selective laser melting porous metallic implants with immobilized silver nanoparticles kill and prevent biofilm formation by methicillin-resistant Staphylococcus aureus, Biomaterials 140 (2017) 1-15.

[71] J.M. Ralph, F.; Coughlan, M.; Thompson, R.; sutterlin, C. E., III; phan, K., The utility of 3D printing for surgical planning and patient-specific implant design for complex spinal pathologies: case report, J Neurosurg Spine 26(4) (2017) 513-518.

[72] I. Yadroitsev, Selective laser melting: Direct manufacturing of 3D-objects by selective laser melting of metal powders, LAP Lambert Academic Publishing, 2009.

[73] O. Rehme, Cellular Design for Laser Freeform Fabrication, Technische Universität Hamburg-Harburg, 2008.

[74] R. Nandhakumar, K. Venkatesan, A process parameters review on selective laser melting-based additive manufacturing of single and multi-material: Microstructure, physical properties, tribological, and surface roughness, Materials Today Communications 35 (2023).

[75] K.G. Prashanth, S. Scudino, T. Maity, J. Das, J. Eckert, Is the energy density a reliable parameter for materials synthesis by selective laser melting?, Materials Research Letters 5(6) (2017) 386-390.

[76] L.N. Carter, X. Wang, N. Read, R. Khan, M. Aristizabal, K. Essa, M.M. Attallah, Process optimisation of selective laser melting using energy density model for nickel based superalloys, Materials Science and Technology 32(7) (2016) 657-661.

[77] L.X. Meng, H.J. Yang, D.D. Ben, H.B. Ji, D.L. Lian, D.C. Ren, Y. Li, T.S. Bai, Y.S. Cai, J. Chen, J.L. Yi, L. Wang, J.B. Yang, Z.F. Zhang, Effects of defects and microstructures on tensile properties of selective laser melted Ti6Al4V alloys fabricated in the optimal process zone, Materials Science and Engineering: A 830 (2022).

[78] L. Thijs, F. Verhaeghe, T. Craeghs, J.V. Humbeeck, J.-P. Kruth, A study of the microstructural evolution during selective laser melting of Ti–6Al–4V, Acta Materialia 58(9) (2010) 3303-3312.

[79] J. Wang, R. Zhu, Y. Liu, L. Zhang, Understanding melt pool characteristics in laser powder bed fusion: An overview of single- and multi-track melt pools for process optimization, Advanced Powder Materials 2(4) (2023).

[80] Y. Li, D. Gu, Parametric analysis of thermal behavior during selective laser melting additive manufacturing of aluminum alloy powder, Materials & Design 63 (2014) 856-867.

[81] H. Salem, L.N. Carter, M.M. Attallah, H.G. Salem, Influence of processing parameters on internal porosity and types of defects formed in Ti6Al4V lattice structure fabricated by selective laser melting, Materials Science and Engineering: A 767 (2019).

[82] C. Britt, C.J. Montgomery, M.J. Brand, Z.-K. Liu, J.S. Carpenter, A.M. Beese, Effect of processing parameters and strut dimensions on the microstructures and hardness of stainless steel 316L lattice-emulating structures made by powder bed fusion, Additive Manufacturing 40 (2021).

[83] H. Jia, H. Sun, H. Wang, Y. Wu, H. Wang, Scanning strategy in selective laser melting (SLM): a review, The International Journal of Advanced Manufacturing Technology 113(9-10) (2021) 2413-2435.

[84] J. Jhabvala, E. Boillat, T. Antignac, R. Glardon, On the effect of scanning strategies in the selective laser melting process, Virtual and Physical Prototyping 5(2) (2010) 99-109.

[85] H. Zhang, D. Gu, D. Dai, C. Ma, Y. Li, R. Peng, S. Li, G. Liu, B. Yang, Influence of scanning strategy and parameter on microstructural feature, residual stress and performance of Sc and Zr modified Al–Mg alloy produced by selective laser melting, Materials Science and Engineering: A 788 (2020).

[86] Q. Bo, S. Yu-sheng, W. Qing-song, W. Hai-bo, The helix scan strategy applied to the selective laser melting, The International Journal of Advanced Manufacturing Technology 63(5-8) (2012) 631-640.

[87] R. Stamp, P. Fox, W. O'Neill, E. Jones, C. Sutcliffe, The development of a scanning strategy for the manufacture of porous biomaterials by selective laser melting, J Mater Sci Mater Med 20(9) (2009) 1839-48.

[88] P. Nandwana, Y. Lee, Influence of scan strategy on porosity and microstructure of Ti-6Al-4V fabricated by electron beam powder bed fusion, Materials Today Communications 24 (2020).

[89] E. Yasa, J.P. Kruth, Microstructural investigation of Selective Laser Melting 316L stainless steel parts exposed to laser re-melting, Procedia Engineering 19 (2011) 389-395.

[90] S. Siddique, M. Imran, M. Rauer, M. Kaloudis, E. Wycisk, C. Emmelmann, F. Walther, Computed tomography for characterization of fatigue performance of selective laser melted parts, Materials & Design 83 (2015) 661-669.

[91] T. Puttonen, S. Chekurov, J. Kuva, R. Björkstrand, J. Partanen, M. Salmi, Influence of feature size and shape on corrosion of 316L lattice structures fabricated by laser powder bed fusion, Additive Manufacturing 61 (2023).

[92] D. Barba, C. Alabort, Y.T. Tang, M.J. Viscasillas, R.C. Reed, E. Alabort, On the size and orientation effect in additive manufactured Ti-6Al-4V, Materials & Design 186 (2020).

[93] L. Di Angelo, P. Di Stefano, E. Guardiani, Search for the Optimal Build Direction in Additive Manufacturing Technologies: A Review, Journal of Manufacturing and Materials Processing 4(3) (2020).

[94] M.X. Gan, C.H. Wong, Practical support structures for selective laser melting, Journal of Materials Processing Technology 238 (2016) 474-484.

[95] X. Zhou, D. Wang, X. Liu, D. Zhang, S. Qu, J. Ma, G. London, Z. Shen, W. Liu, 3D-imaging of selective laser melting defects in a Co–Cr–Mo alloy by synchrotron radiation micro-CT, Acta Materialia 98 (2015) 1-16.

[96] X. Yang, Z. Zhang, T. Zhang, F. Song, X. Yao, B. Xiao, P. Lin, H. Qi, S. Liu, H. Tang, Multi-build orientation effects on microstructural evolution and mechanical behavior of truly as-built selective laser melting Ti6Al4V alloys, Journal of Materials Research and Technology 30 (2024) 3967-3976.

[97] M. Simonelli, Y.Y. Tse, C. Tuck, Effect of the build orientation on the mechanical properties and fracture modes of SLM Ti–6Al–4V, Materials Science and Engineering: A 616 (2014) 1-11.

[98] L. Ding, S. Tan, W. Chen, Y. Jin, Y. Zhang, Manufacturability analysis of extremely fine porous structures for selective laser melting process of Ti6Al4V alloy, Rapid Prototyping J 27(8) (2021) 1523-1537.

[99] R.A. Yildiz, A.-A. Popa, M. Malekan, On the effect of small laser spot size on the mechanical behaviour of 316L stainless steel fabricated by L-PBF additive manufacturing, Materials Today Communications 38 (2024).

[100] A. Sarker, N. Tran, A. Rifai, J. Elambasseril, M. Brandt, R. Williams, M. Leary, K. Fox, Angle defines attachment: Switching the biological response to titanium interfaces by modifying the inclination angle during selective laser melting, Materials & Design 154 (2018) 326-339.

[101] J. Noronha, M. Qian, M. Leary, E. Kyriakou, S. Brudler, M. Brandt, Manufacturability of Ti-6Al-4V Hollow-Walled Lattice Struts by Laser Powder Bed Fusion, Jom 73(12) (2021) 4199-4208.

[102] C. Qiu, S. Yue, N.J.E. Adkins, M. Ward, H. Hassanin, P.D. Lee, P.J. Withers, M.M. Attallah, Influence of processing conditions on strut structure and compressive properties of cellular lattice structures fabricated by selective laser melting, Materials Science and Engineering: A 628 (2015) 188-197.

[103] S. Van Bael, G. Kerckhofs, M. Moesen, G. Pyka, J. Schrooten, J.P. Kruth, Micro-CT-based improvement of geometrical and mechanical controllability of selective laser melted Ti6Al4V porous structures, Materials Science and Engineering: A 528(24) (2011) 7423-7431.

[104] A.H. Maamoun, Y.F. Xue, M.A. Elbestawi, S.C. Veldhuis, Effect of Selective Laser Melting Process Parameters on the Quality of Al Alloy Parts: Powder

Characterization, Density, Surface Roughness, and Dimensional Accuracy, Materials (Basel) 11(12) (2018).

[105] L. Mullen, R.C. Stamp, W.K. Brooks, E. Jones, C.J. Sutcliffe, Selective Laser Melting: a regular unit cell approach for the manufacture of porous, titanium, bone in-growth constructs, suitable for orthopedic applications, J Biomed Mater Res B Appl Biomater 89(2) (2009) 325-334.

[106] J. Pegues, M. Roach, R. Scott Williamson, N. Shamsaei, Surface roughness effects on the fatigue strength of additively manufactured Ti-6Al-4V, International Journal of Fatigue 116 (2018) 543-552.

[107] J.W. Pegues, S. Shao, N. Shamsaei, N. Sanaei, A. Fatemi, D.H. Warner, P. Li, N. Phan, Fatigue of additive manufactured Ti-6Al-4V, Part I: The effects of powder feedstock, manufacturing, and post-process conditions on the resulting microstructure and defects, International Journal of Fatigue 132 (2020).

[108] A. Charles, A. Elkaseer, L. Thijs, V. Hagenmeyer, S. Scholz, Effect of Process Parameters on the Generated Surface Roughness of Down-Facing Surfaces in Selective Laser Melting, Applied Sciences 9(6) (2019).

[109] I. Koutiri, E. Pessard, P. Peyre, O. Amlou, T. De Terris, Influence of SLM process parameters on the surface finish, porosity rate and fatigue behavior of as-built Inconel 625 parts, Journal of Materials Processing Technology 255 (2018) 536-546.

[110] M. Elsayed, M. Ghazy, Y. Youssef, K. Essa, Optimization of SLM process parameters for Ti6Al4V medical implants, Rapid Prototyping J 25(3) (2018) 433-447.

[111] X. Han, H. Zhu, X. Nie, G. Wang, X. Zeng, Investigation on Selective Laser Melting AlSi10Mg Cellular Lattice Strut: Molten Pool Morphology, Surface Roughness and Dimensional Accuracy, Materials (Basel) 11(3) (2018).

[112] X. Cao, L.N. Carter, K. Man, V.M. Villapún, L. Giangiorgi, S.C. Cox, Improving predictability of additively manufactured Ti-6Al-4 V lattices for orthopaedic devices: A parametric and struts angle study, Materials & Design 243 (2024).

[113] M. McMillan, M. Leary, M. Brandt, Computationally efficient finite difference method for metal additive manufacturing: A reduced-order DFAM tool applied to SLM, Materials & Design 132 (2017) 226-243.

[114] G. Yang, Y. Xie, S. Zhao, L. Qin, X. Wang, B. Wu, Quality Control: Internal Defects Formation Mechanism of Selective Laser Melting Based on Laser-powder-melt Pool Interaction: A Review, Chinese Journal of Mechanical Engineering: Additive Manufacturing Frontiers 1(3) (2022).

[115] M. Seiler, A. Patschger, J. Bliedtner, Investigations of welding instabilities and weld seam formation during laser microwelding of ultrathin metal sheets, Journal of Laser Applications 28(2) (2016).

[116] S.A. Khairallah, A.T. Anderson, A. Rubenchik, W.E. King, Laser powder-bed fusion additive manufacturing: Physics of complex melt flow and formation mechanisms of pores, spatter, and denudation zones, Acta Materialia 108 (2016) 36-45.

[117] B. Zhang, Y. Li, Q. Bai, Defect Formation Mechanisms
in Selective Laser Melting: A Review, Chinese Journal of Mechanical Engineering 30(3) (2017) 515-527.

[118] C.L.A. Leung, S. Marussi, R.C. Atwood, M. Towrie, P.J. Withers, P.D. Lee, In situ X-ray imaging of defect and molten pool dynamics in laser additive manufacturing, Nat Commun 9(1) (2018) 1355.

[119] F.O. Olsen, Hybrid laser-arc welding, Elsevier, 2009.

[120] C. Yan, L. Hao, A. Hussein, D. Raymont, Evaluations of cellular lattice structures manufactured using selective laser melting, International Journal of Machine Tools and Manufacture 62 (2012) 32-38.

[121] Y. Amani, S. Dancette, P. Delroisse, A. Simar, E. Maire, Compression behavior of lattice structures produced by selective laser melting: X-ray tomography based experimental and finite element approaches, Acta Materialia 159 (2018) 395-407.

[122] Z. Dong, Y. Liu, W. Li, J. Liang, Orientation dependency for microstructure, geometric accuracy and mechanical properties of selective laser melting AlSi10Mg lattices, Journal of Alloys and Compounds 791 (2019) 490-500.

[123] D. Gu, Y.-C. Hagedorn, W. Meiners, G. Meng, R.J.S. Batista, K. Wissenbach, R. Poprawe, Densification behavior, microstructure evolution, and wear performance of selective laser melting processed commercially pure titanium, Acta Materialia 60(9) (2012) 3849-3860.

[124] B. Wysocki, P. Maj, A. Krawczyńska, K. Rożniatowski, J. Zdunek, K.J. Kurzydłowski, W. Święszkowski, Microstructure and mechanical properties investigation of CP titanium processed by selective laser melting (SLM), Journal of Materials Processing Technology 241 (2017) 13-23.

[125] W. Xu, M. Brandt, S. Sun, J. Elambasseril, Q. Liu, K. Latham, K. Xia, M. Qian, Additive manufacturing of strong and ductile Ti–6Al–4V by selective laser melting via in situ martensite decomposition, Acta Materialia 85 (2015) 74-84.

[126] R. Wauthle, B. Vrancken, B. Beynaerts, K. Jorissen, J. Schrooten, J.-P. Kruth, J. Van Humbeeck, Effects of build orientation and heat treatment on the microstructure and mechanical properties of selective laser melted Ti6Al4V lattice structures, Additive Manufacturing 5 (2015) 77-84.

[127] J. Ge, X. Yan, Y. Lei, M. Ahmed, P. O'Reilly, C. Zhang, R. Lupoi, S. Yin, A detailed analysis on the microstructure and compressive properties of selective laser melted Ti6Al4V lattice structures, Materials & Design 198 (2021).

[128] S.S. B. Torries, N. Shamsaei, S.M. Thompson, Effect of Inter-Layer Time Interval on the Mechanical Behavior of Direct Laser Deposited Ti-6Al-4V, Solid Freeform Fabrication 2016: Proceedings of the 27th Annual International Solid Freeform Fabrication Symposium - An Additive Manufacturing Conference, 2016, pp. 1272 - 1282.

[129] P. Li, D.H. Warner, J.W. Pegues, M.D. Roach, N. Shamsaei, N. Phan, Investigation of the mechanisms by which hot isostatic pressing improves the fatigue performance of powder bed fused Ti-6Al-4V, Int J Fatigue 120 (2019) 342-352.

[130] L. Xu, R. Guo, C. Bai, J. Lei, R. Yang, Effect of Hot Isostatic Pressing Conditions and Cooling Rate on Microstructure and Properties of Ti–6Al–4V Alloy from Atomized Powder, Journal of Materials Science & Technology 30(12) (2014) 1289-1295.

[131] V.M. Villapún, L.N. Carter, N. Gao, O. Addison, M.A. Webber, D.E.T. Shepherd, J.W. Andrews, M. Lowther, S. Avery, S.J. Glanvill, L.M. Grover, S. Cox, A design approach to facilitate selective attachment of bacteria and mammalian cells to additively manufactured implants, Additive Manufacturing 36 (2020).

[132] S.M. Ahmadi, R. Hedayati, Y. Li, K. Lietaert, N. Tumer, A. Fatemi, C.D. Rans, B. Pouran, H. Weinans, A.A. Zadpoor, Fatigue performance of additively manufactured meta-biomaterials: The effects of topology and material type, Acta Biomater 65 (2018) 292-304.

[133] H.S. Abdulhadi, A. Mian, Effect of strut length and orientation on elastic mechanical response of modified body-centered cubic lattice structures, Proceedings of the Institution of Mechanical Engineers, Part L: Journal of Materials: Design and Applications 233(11) (2019) 2219-2233.

[134] C. Rodrigo, S. Xu, Y. Durandet, P. Tran, D. Ruan, Mechanical response of functionally graded lattices with different density grading strategies, Thin-Walled Structures 192 (2023).

[135] P. Li, Y.E. Ma, W. Sun, X. Qian, W. Zhang, Z. Wang, Mechanical behaviors and failure modes of additive manufactured Ti6Al4V lattice structures under compressive load, Thin-Walled Structures 180 (2022).

[136] C. Li, H. Lei, Y. Liu, X. Zhang, J. Xiong, H. Zhou, D. Fang, Crushing behavior of multi-layer metal lattice panel fabricated by selective laser melting, International Journal of Mechanical Sciences 145 (2018) 389-399.

[137] M. He, Y. Li, J. Yin, Q. Sun, W. Xiong, S. Li, L. Yang, L. Hao, Compressive performance and fracture mechanism of bio-inspired heterogeneous glass sponge lattice structures manufactured by selective laser melting, Materials & Design 214 (2022).

[138] L. Bai, C. Gong, X. Chen, J. Zheng, J. Yang, K. Li, Y. Sun, Heterogeneous compressive responses of additively manufactured Ti-6Al-4V lattice structures by varying geometric parameters of cells, International Journal of Mechanical Sciences 214 (2022).

[139] Y. Liu, J. Zhang, X. Gu, Y. Zhou, Y. Yin, Q. Tan, M. Li, M.-X. Zhang, Mechanical performance of a node reinforced body-centred cubic lattice structure manufactured via selective laser melting, Scripta Materialia 189 (2020) 95-100.

[140] F. Li, J. Li, H. Kou, L. Zhou, Porous Ti6Al4V alloys with enhanced normalized fatigue strength for biomedical applications, Mater Sci Eng C Mater Biol Appl 60 (2016) 485-488.

[141] M.-W. Wu, J.-K. Chen, B.-H. Lin, P.-H. Chiang, Improved fatigue endurance ratio of additive manufactured Ti-6Al-4V lattice by hot isostatic pressing, Materials & Design 134 (2017) 163-170.

[142] A. Zargarian, M. Esfahanian, J. Kadkhodapour, S. Ziaei-Rad, D. Zamani, On the fatigue behavior of additive manufactured lattice structures, Theoretical and Applied Fracture Mechanics 100 (2019) 225-232.

[143] S. Zhao, S.J. Li, W.T. Hou, Y.L. Hao, R. Yang, R.D.K. Misra, The influence of cell morphology on the compressive fatigue behavior of Ti-6Al-4V meshes fabricated by electron beam melting, J Mech Behav Biomed Mater 59 (2016) 251-264.

[144] D. Ren, S. Li, H. Wang, W. Hou, Y. Hao, W. Jin, R. Yang, R.D.K. Misra, L.E. Murr, Fatigue behavior of Ti-6Al-4V cellular structures fabricated by additive manufacturing technique, Journal of Materials Science & Technology 35(2) (2019) 285-294.

[145] M. Alana, A. Cutolo, S. Ruiz de Galarreta, B. Van Hooreweder, Influence of relative density on quasi-static and fatigue failure of lattice structures in Ti6Al4V produced by laser powder bed fusion, Sci Rep 11(1) (2021) 19314.

[146] L. Yang, Y. Li, Y. Chen, C. Yan, B. Liu, Y. Shi, Topologically optimized lattice structures with superior fatigue performance, International Journal of Fatigue 165 (2022).

[147] S. Amin Yavari, S.M. Ahmadi, R. Wauthle, B. Pouran, J. Schrooten, H. Weinans, A.A. Zadpoor, Relationship between unit cell type and porosity and the fatigue behavior of selective laser melted meta-biomaterials, J Mech Behav Biomed Mater 43 (2015) 91-100.

[148] H.D. Nguyen, A. Pramanik, A.K. Basak, Y. Dong, C. Prakash, S. Debnath, S. Shankar, I.S. Jawahir, S. Dixit, D. Buddhi, A critical review on additive manufacturing of Ti-6Al-4V alloy: microstructure and mechanical properties, Journal of Materials Research and Technology 18 (2022) 4641-4661.

[149] D. Mahmoud, K.S. Al-Rubaie, M.A. Elbestawi, The influence of selective laser melting defects on the fatigue properties of Ti6Al4V porosity graded gyroids for bone implants, International Journal of Mechanical Sciences 193 (2021).

[150] R. Jiang, D.J. Bull, A. Evangelou, A. Harte, F. Pierron, I. Sinclair, M. Preuss, X.T. Hu, P.A.S. Reed, Strain accumulation and fatigue crack initiation at pores and carbides in a SX superalloy at room temperature, International Journal of Fatigue 114 (2018) 22-33.

[151] Z. Alomar, F. Concli, A Review of the Selective Laser Melting Lattice Structures and Their Numerical Models, Advanced Engineering Materials 22(12) (2020).

[152] P.J. Lal Lazar, J. Subramanian, M. Manickam, V.K. Selvaraj, Imperfections and computational modeling of lattice structures developed through powder bed fusion – A short review, Materials Today: Proceedings (2023).

[153] J.S. Rathore, C. Mang, C. Vienne, Y. Quinsat, C. Tournier, A Methodology for Computed Tomography-Based Non-Destructive Geometrical Evaluations of Lattice Structures by Holistic Strut Measurement Approach, Journal of Manufacturing Science and Engineering 143(5) (2021).

[154] J. Schröder, A. Evans, T. Mishurova, A. Ulbricht, M. Sprengel, I. Serrano-Munoz, T. Fritsch, A. Kromm, T. Kannengießer, G. Bruno, Diffraction-Based Residual Stress Characterization in Laser Additive Manufacturing of Metals, Metals 11(11) (2021).

[155] P. Vora, K. Mumtaz, I. Todd, N. Hopkinson, AlSi12 in-situ alloy formation and residual stress reduction using anchorless selective laser melting, Additive Manufacturing 7 (2015) 12-19.

[156] B. Vrancken, Study of residual stresses in selective laser melting, 2016.

[157] Y.T. Yao, Y. Yang, Q. Ye, S.S. Cao, X.P. Zhang, K. Zhao, Y. Jian, Effects of pore size and porosity on cytocompatibility and osteogenic differentiation of porous titanium, J Mater Sci Mater Med 32(6) (2021) 72.

[158] A. Cheng, A. Humayun, D.J. Cohen, B.D. Boyan, Z. Schwartz, Additively manufactured 3D porous Ti-6Al-4V constructs mimic trabecular bone structure and regulate osteoblast proliferation, differentiation and local factor production in a porosity and surface roughness dependent manner, Biofabrication 6(4) (2014) 045007.

[159] L.E. Murr, Metallurgy principles applied to powder bed fusion 3D printing/additive manufacturing of personalized and optimized metal and alloy biomedical implants: an overview, J. Mater. Res. Technol. 9(1) (2020) 1087–1103.

[160] R. Hedayati, M. Sadighi, M. Mohammadi-Aghdam, H. Hosseini-Toudeshky, Comparison of elastic properties of open-cell metallic biomaterials with different unit cell types, J. Biomed. Mater. Res. B Appl. Biomater. 106(1) (2018) 386-398.

[161] A. Deing, B.L. Luthringer, D. Laipple, T. Ebel, R. Willumeit, A Porous TiAl6V4 Implant Material for Medical Application, Int. J. Biomater. 2014 (2014) 8.

[162] S. Maietta, A. Gloria, G. Improta, M. Richetta, R. De Santis, M. Martorelli, A Further Analysis on Ti6Al4V Lattice Structures Manufactured by Selective Laser Melting, J. Healthc. Eng. 2019 (2019) 9.

[163] X. Wang, S. Xu, S. Zhou, W. Xu, M. Leary, P. Choong, M. Qian, M. Brandt, Y.M. Xie, Topological design and additive manufacturing of porous metals for bone scaffolds and orthopaedic implants: A review, Biomaterials 83 (2016) 127-141.

[164] J. Markhoff, J. Wieding, V. Weissmann, J. Pasold, A. Jonitz-Heincke, R. Bader, Influence of Different Three-Dimensional Open Porous Titanium Scaffold Designs on Human Osteoblasts Behavior in Static and Dynamic Cell Investigations, Materials 8(8) (2015) 5490-5507.

[165] B. Li, B.D. Hesar, Y. Zhao, L. Ding, Design and additive manufacturing of porous titanium scaffolds for optimum cell viability in bone tissue engineering, Proceedings of the Institution of Mechanical Engineers. Part B, Journal of engineering manufacture (2020) 95440542093756.

[166] S. Van Bael, Y.C. Chai, S. Truscello, M. Moesen, G. Kerckhofs, H. Van Oosterwyck, J.P. Kruth, J. Schrooten, The effect of pore geometry on the in vitro biological behavior of human periosteum-derived cells seeded on selective laser-melted Ti6Al4V bone scaffolds, Acta Biomaterialia 8(7) (2012) 2824-2834.

[167] Z. Wang, C. Wang, C. Li, Y. Qin, L. Zhong, B. Chen, Z. Li, H. Liu, F. Chang, J. Wang, Analysis of factors influencing bone ingrowth into three-dimensional printed porous metal scaffolds: A review, Journal of Alloys and Compounds 717 (2017) 271-285.

[168] N. Chantarapanich, P. Puttawibul, S. Sucharitpwatskul, P. Jeamwatthanachai, S. Inglam, K. Sitthiseripratip, Scaffold Library for Tissue Engineering: A Geometric Evaluation, Computational and Mathematical Methods in Medicine 2012 (2012) 407805.

[169] H.E. Burton, N.M. Eisenstein, B.M. Lawless, P. Jamshidi, M.A. Segarra, O. Addison, D.E.T. Shepherd, M.M. Attallah, L.M. Grover, S.C. Cox, The design of additively manufactured lattices to increase the functionality of medical implants, Mater. Sci. Eng., C 94 (2019) 901-908.

[170] L.N. Carter, O. Addison, N. Naji, P. Seres, A.H. Wilman, D.E.T. Shepherd, L.M. Grover, S.C. Cox, Reducing MRI susceptibility artefacts in implants using additively manufactured porous Ti-6Al-4V structures, Acta Biomater. 107 (2020) 338-348.

[171] H. Shipley, D. McDonnell, M. Culleton, R. Coull, R. Lupoi, G. O'Donnell, D. Trimble, Optimisation of process parameters to address fundamental challenges during selective laser melting of Ti-6Al-4V: A review, Int. J. Mach. Tools Manuf. 128 (2018) 1-20.

[172] L. Mullen, R.C. Stamp, W.K. Brooks, E. Jones, C.J. Sutcliffe, Selective Laser Melting: A Regular Unit Cell Approach for the Manufacture of Porous, Titanium, Bone In-Growth Constructs, Suitable for Orthopedic Applications, Wiley 89B (2009) 325-334.

[173] A. Koptyug, L.E. Rännar, M. Bäckström, S.F. Fager Franzén, P. Dérand, Additive Manufacturing Technology Applications Targeting Practical Surgery, Int. J. Life Sci. Med. Res. 3(1) (2013) 15-24.

[174] F. Trevisan, F. Calignano, M. Lorusso, J. Pakkanen, A. Aversa, E.P. Ambrosio, M. Lombardi, P. Fino, D. Manfredi, On the Selective Laser Melting (SLM) of the AlSi10Mg Alloy: Process, Microstructure, and Mechanical Properties, Materials 10(1) (2017) 76.

[175] B. Song, S. Dong, B. Zhang, H. Liao, C. Coddet, Effects of processing parameters on microstructure and mechanical property of selective laser melted Ti6Al4V, Mater. Des. 35 (2012) 120-125.

[176] D.S. Nguyen, H.S. Park, C.M. Lee, Optimization of selective laser melting process parameters for Ti-6Al-4V alloy manufacturing using deep learning, J. Manuf. Process 55 (2020) 230-235.

[177] A.H. Maamoun, Y.F. Xue, M.A. Elbestawi, S.C. Veldhuis, Effect of Selective Laser Melting Process Parameters on the Quality of Al Alloy Parts: Powder Characterization, Density, Surface Roughness,and Dimensional Accuracy, Materials 11(12) (2018) 2343.

[178] A. Großmann, J. Felger, T. Frölich, J. Gosmann, C. Mittelstedt, Melt pool controlled laser powder bed fusion for customised low-density lattice structures, Mater. Des. 181 (2019) 108054.

[179] C. Kusuma, S.H. Ahmed, A. Mian, R. Srinivasan, Effect of Laser Power and Scan Speed on Melt Pool Characteristics of Commercially Pure Titanium (CP-Ti), J. Mater. Eng. Perform. 26(7) (2017) 3560-3568.

[180] S.M. Yusuf, N. Gao, Influence of energy density on metallurgy and properties in metal additive manufacturing, Mater. Sci. Technol. 33(11) (2017) 1269-1289.

[181] M.H. Hong, B.K. Min, T.-Y. Kwon, The Influence of Process Parameters on the Surface Roughness of a 3D-Printed Co–Cr Dental Alloy Produced via Selective Laser Melting, Appl. Sci. 6 (2016) 401.

[182] L.Z. Wang, S. Wang, J.-J. Wu, Experimental investigation on densification behavior and surface roughness of AlSi10Mg powders produced by selective laser melting, Opt. Laser Technol. 96 (2017) 88-96.

[183] A. Khorasania, I. Gibsond, U.S. Awana, A. Ghaderi, The effect of SLM process parameters on density, hardness, tensile strength and surface quality of Ti-6Al-4V, Addit. Manuf. 25 (2019) 176-186.

[184] Q. Qin, G.X. Chen, Effects of Parameters on Surface Roughness of Metal Parts by Selective Laser Melting, Adv. Mater. Res. 834 (2013) 872-875.

[185] V.M. Villapún, L.N. Carter, N. Gao, O. Addison, M.A. Webber, D.E.T. Shepherd, J.W. Andrews, M. Lowther, S. Avery, S.J. Glanvill, L.M. Grover, S.C. Cox, A design approach to facilitate selective attachment of bacteria and T mammalian cells to additively manufactured implants, Addit. Manuf. 36 (2020) 101528.

[186] H. Salem, L.N. Carter, M.M. Attallah, H.G. Salem, Influence of processing parameters on internal porosity and types of defects formed in Ti6Al4V lattice structure fabricated by selective laser melting, Mater. Sci. Eng., A 767 (2019) 138387.

[187] C. Qiu, S. Yue, N.J.E. Adkins, M. Ward, H. Hassanin, P.D. Lee, P.J. Withers, M.M. Attallah, Influence of processing conditions on strut structure and compressive properties of cellular lattice structures fabricated by selective laser melting, Mater. Sci. Eng., A 628 (2015) 188-197.

[188] H. Gu, H. Gong, D. Pal, K. Rafi, T. Starr, B. Stucker, Influences of Energy Density on Porosity and Microstructure of Selective Laser Melted 17- 4PH Stainless Steel, Solid Freeform Fabr. Symp. 474 (2013) 474-489.

[189] C. Yan, L. Hao, A. Hussein, P. Young, D. Raymont, Advanced lightweight 316L stainless steel cellular lattice structures fabricated via selective laser melting, Mater. Des. 55 (2014) 533-541.

[190] S. Ghouse, S. Babu, R.J. Van Arkel, K. Nai, P.A. Hooper, J.R.T. Jeffers, The influence of laser parameters and scanning strategies on the mechanical properties of a stochastic porous material, Mater. Des. 131 (2017) 498-508.

[191] E. Onal, A.E. Medvedev, M.A. Leeflang, A. Molotnikov, A.A. Zadpoor, Novel microstructural features of selective laser melted lattice struts fabricated with single point exposure scanning, Addit. Manuf. 29 (2019) 100785.

[192] S.M. Ahmadi, G. Campoli, S.A. Yavari, B. Sajadia, R. Wauthle, J. Schrootend, H. Weinans, A.A. Zadpoor, Mechanical behavior of regular open-cell porous biomaterials made of diamond lattice unit cells, J. Mech. Behav. Biomed. Mater. 34 (2014) 106-115.

[193] B. Derby, Printing and Prototyping of Tissues and Scaffolds, Science 338(6109) (2012) 921-926.

[194] P. Heinl, L. Müller, C. Körner, R.F. Singer, F.A. Müller, Cellular Ti–6Al–4V structures with interconnected macro porosity for bone implants fabricated by selective electron beam melting, Acta Biomaterialia 4(5) (2008) 1536-1544.

[195] L. Nickels, Software toolkits for architected materials, lightweighting, and more, Met. Powder Rep., 2020, pp. 203-206.

[196] C.A. Schneider, W.S. Rasband, K.W. Eliceiri, NIH Image to ImageJ: 25 years of image analysis, Nat. Methods 9(7) (2012) 671-675.

[197] R. Rashida, S.H. Masooda, D. Ruana, S. Palanisamy, R.A.R. Rashid, M. Brandt, Effect of scan strategy on density and metallurgical properties of 17-4PH parts printed by Selective Laser Melting (SLM), J. Mater. Process. Technol. 249 (2017) 502-511.

[198] C. Yan, L. Hao, A. Hussein, D. Raymont, Evaluations of cellular lattice structures manufactured using selective laser melting, Int. J. Mach. Tools Manuf. 62 (2012) 32-38.

[199] T. Maconachie, M. Leary, B. Lozanovski, X. Zhang, M. Qian, O. Faruque, M. Brandt, SLM lattice structures: Properties, performance, applications and challenges, Materials & Design 183 (2019).

[200] N. Soro, H. Attar, X. Wu, M.S. Dargusch, Investigation of the structure and mechanical properties of additively manufactured Ti-6Al-4V biomedical scaffolds designed with a Schwartz primitive unit-cell, Materials Science and Engineering: A 745 (2019) 195-202.

[201] S.Y. Chunlei Qiu, Nicholas J.E. Adkins, Mark Ward, Hany Hassanin, Peter D. Lee, Philip J. Withers, Moataz M. Attallah, Influence of processing conditions on strut structure and compressive properties of cellular lattice structures fabricated by selective laser melting, Materials Science & Engineering A 628 (2015) 188-197.

[202] L.N. Carter, O. Addison, N. Naji, P. Seres, A.H. Wilman, D.E.T. Shepherd, L. Grover, S. Cox, Reducing MRI susceptibility artefacts in implants using additively manufactured porous Ti-6Al-4V structures, Acta Biomater 107 (2020) 338-348.

[203] T. Maconachie, M. Leary, B. Lozanovski, X.Z. Zhang, M. Qian, O. Faruque, M. Brandt, SLM lattice structures: Properties, performance, applications and challenges, Materials & Design 183 (2019).

[204] D. Greitemeier, C. Dalle Donne, F. Syassen, J. Eufinger, T. Melz, Effect of surface roughness on fatigue performance of additive manufactured Ti–6Al–4V, Materials Science and Technology 32(7) (2016) 629-634.

[205] Z. Wang, Z. Xiao, Y. Tse, C. Huang, W. Zhang, Optimization of processing parameters and establishment of a relationship between microstructure and mechanical properties of SLM titanium alloy, Optics & Laser Technology 112 (2019) 159-167.

[206] S.M. Ahmadi, R. Hedayati, R.K. Ashok Kumar Jain, Y. Li, S. Leeflang, A.A. Zadpoor, Effects of laser processing parameters on the mechanical properties, topology, and microstructure of additively manufactured porous metallic biomaterials: A vector-based approach, Materials & Design 134 (2017) 234-243.

[207] S. Murchio, M. Dallago, F. Zanini, S. Carmignato, G. Zappini, F. Berto, D. Maniglio, M. Benedetti, Additively manufactured Ti-6Al-4V thin struts via laser powder bed fusion: Effect of building orientation on geometrical accuracy and mechanical properties, J Mech Behav Biomed Mater 119 (2021) 104495.

[208] I. Aiza, C. Baldi, F.M. de la Vega, S. Sebastiani, N.E. Veronese, M. Yousefi, M.H. Mosallanejad, E. Maleki, M. Guagliano, L. Iuliano, A. Saboori, S. Bagherifard, Effects of build orientation and inclined features on physical, microstructural and mechanical properties of powder bed fusion additively manufactured metallic parts, Progress in Materials Science 147 (2025).

[209] G. Meyer, J. Musekamp, F. Göbel, F. Gardian, C. Mittelstedt, Manufacturability investigation of inclined AlSi10Mg lattice struts by means of selective laser melting, Manufacturing Letters 31 (2022) 101-105.

[210] S. Murchio, M. Dallago, A. Rigatti, V. Luchin, F. Berto, D. Maniglio, M. Benedetti, On the effect of the node and building orientation on the fatigue behavior of L-PBF Ti6Al4V lattice structure sub-unital elements, Material Design & Processing Communications 3(6) (2021).

[211] M. Suard, G. Martin, P. Lhuissier, R. Dendievel, F. Vignat, J.J. Blandin, F. Villeneuve, Mechanical equivalent diameter of single struts for the stiffness prediction of lattice structures produced by Electron Beam Melting, Additive Manufacturing 8 (2015) 124-131.

[212] M. Mazur, M. Leary, S. Sun, M. Vcelka, D. Shidid, M. Brandt, Deformation and failure behaviour of Ti-6Al-4V lattice structures manufactured by selective laser melting (SLM), The International Journal of Advanced Manufacturing Technology (2015).

[213] U. Hossain, S. Ghouse, K. Nai, J.R.T. Jeffers, Mechanical and morphological properties of additively manufactured SS316L and Ti6Al4V micro-struts as a function of build angle, Additive Manufacturing 46 (2021) 102050.

[214] J.T. Ho, J. Wu, H.L. Huang, M.Y. Chen, L.J. Fuh, J.T. Hsu, Trabecular bone structural parameters evaluated using dental cone-beam computed tomography: cellular synthetic bones, Biomed Eng Online 12 (2013) 115.

[215] C.A. Schneider, Rasband, W.S., Eliceiri, K.W., NIH Image to ImageJ: 25 years of image analysis, Nature Methods 9(7) (2012) 671-675.

[216] C.C. Chamis, ANALYSIS OF THE THREE-POINT-BEND TEST FOR MATERIALS WITH UNEQUAL TENSION AND COMPRESSION PROPERTIES, National Aeronautics and Space Administration, 1974, p. 33.

[217] tec-science, Bending flexural test, 2018. https://www.tec-science.com/material-science/material-testing/bending-flexural-test/.

[218] K. Man, C. Alcala, N.V. Mekhileri, K.S. Lim, L.H. Jiang, T.B.F. Woodfield, X.B. Yang, GelMA Hydrogel Reinforced with 3D Printed PEGT/PBT Scaffolds for Supporting Epigenetically-Activated Human Bone Marrow Stromal Cells for Bone Repair, J Funct Biomater 13(2) (2022).

[219] I.G. AmirMahyar Khorasania, Umar Shafique Awana, Alireza Ghaderi, The effect of SLM process parameters on density, hardness, tensile strength T and surface quality of Ti-6Al-4V, Additive Manufacturing 25 (2019) 176-186.

[220] C. Ni, Y. Shi, J. Liu, Influences of tilt angles on microstructure and mechanical properties of 316L stainless steel parts fabricated by selective laser melting (SLM), Materials Research Express 6(8) (2019).

[221] Q.C. Liu, J. Elambasseril, S.J. Sun, M. Leary, M. Brandt, P.K. Sharp, The Effect of Manufacturing Defects on the Fatigue Behaviour of Ti-6Al-4V Specimens Fabricated Using Selective Laser Melting, Advanced Materials Research 891-892 (2014) 1519-1524.

[222] P.E. Markovsky, D.G. Savvakin, O.M. Ivasishin, V.I. Bondarchuk, S.V. Prikhodko, Mechanical Behavior of Titanium-Based Layered Structures Fabricated Using Blended Elemental Powder Metallurgy, Journal of Materials Engineering and Performance 28(9) (2019) 5772-5792.

[223] C. Bellini, R. Borrelli, V. Di Cocco, S. Franchitti, F. Iacoviello, L. Sorrentino, Damage analysis of Ti6Al4V lattice structures manufactured by electron beam melting process subjected to bending load, Material Design & Processing Communications 3(6) (2021).

[224] A.Y. Al-Maharma, S.P. Patil, B. Markert, Effects of porosity on the mechanical properties of additively manufactured components: a critical review, Materials Research Express 7(12) (2020).

[225] D. Palmeri, G. Buffa, G. Pollara, L. Fratini, Sample building orientation effect on porosity and mechanical properties in Selective Laser Melting of Ti6Al4V titanium alloy, Materials Science and Engineering: A 830 (2022).

[226] S. Sneddon, Y. Xu, M. Dixon, D. Rugg, P.F. Li, D.M. Mulvihill, Sensitivity of material failure to surface roughness: A study on titanium alloys Ti64 and Ti407, Materials & Design 200 (2021).

[227] K. Man, M.Y. Brunet, S. Louth, T.E. Robinson, M. Fernandez-Rhodes, S. Williams, A.S. Federici, O.G. Davies, D.A. Hoey, S.C. Cox, Development of a Bone-Mimetic 3D Printed Ti6Al4V Scaffold to Enhance Osteoblast-Derived Extracellular Vesicles' Therapeutic Efficacy for Bone Regeneration, Front Bioeng Biotechnol 9 (2021) 757220.

[228] I. Holland, J. Logan, J. Shi, C. McCormick, D. Liu, W. Shu, 3D biofabrication for tubular tissue engineering, Biodes Manuf 1(2) (2018) 89-100.

[229] S.C. Cox, P. Jamshidi, N.M. Eisenstein, M.A. Webber, H. Burton, R.J.A. Moakes, O. Addison, M. Attallah, D.E.T. Shepherd, L.M. Grover, Surface Finish has a Critical Influence on Biofilm Formation and Mammalian Cell Attachment to Additively Manufactured Prosthetics, ACS Biomater Sci Eng 3(8) (2017) 1616-1626.

[230] Y. Hou, W. Xie, L. Yu, L.C. Camacho, C. Nie, M. Zhang, R. Haag, Q. Wei, Surface Roughness Gradients Reveal Topography-Specific Mechanosensitive Responses in Human Mesenchymal Stem Cells, Small 16(10) (2020) e1905422.

[231] S. Stewart, A. Darwood, S. Masouros, C. Higgins, A. Ramasamy, Mechanotransduction in osteogenesis, Bone Joint Res 9(1) (2020) 1-14.

[232] F. Distefano, S. Pasta, G. Epasto, Titanium Lattice Structures Produced via Additive Manufacturing for a Bone Scaffold: A Review, J Funct Biomater 14(3) (2023).

[233] G. Osterhoff, E.F. Morgan, S.J. Shefelbine, L. Karim, L.M. McNamara, P. Augat, Bone mechanical properties and changes with osteoporosis, Injury 47 Suppl 2(Suppl 2) (2016) S11-20.

[234] N. Xue, X. Ding, R. Huang, R. Jiang, H. Huang, X. Pan, W. Min, J. Chen, J.A. Duan, P. Liu, Y. Wang, Bone Tissue Engineering in the Treatment of Bone Defects, Pharmaceuticals (Basel) 15(7) (2022).

[235] R. De Biasi, S. Murchio, E. Sbettega, S. Carmignato, V. Luchin, M. Benedetti, Efficient optimization framework for L-PBF fatigue enhanced Ti6Al4V lattice component, Materials & Design 230 (2023).

[236] X. Cao, L.N. Carter, V.M. Villapún, F. Cantaboni, G. De Sio, M. Lowther, S.E.T. Louth, L. Grover, P. Ginestra, S.C. Cox, Optimisation of single contour strategy in selective laser melting of Ti-6Al-4V lattices, Rapid Prototyping J (2022).

[237] Z. Zheng, X. Jin, Y. Bai, Y. Yang, C. Ni, W.F. Lu, H. Wang, Microstructure and anisotropic mechanical properties of selective laser melted Ti6Al4V alloy under different scanning strategies, Materials Science and Engineering: A 831 (2022).

[238] R. Vrána, J. Jaroš, D. Koutný, J. Nosek, T. Zikmund, J. Kaiser, D. Paloušek, Contour laser strategy and its benefits for lattice structure manufacturing by selective laser melting technology, Journal of Manufacturing Processes 74 (2022) 640-657.

[239] S. Kechagias, R.N. Oosterbeek, M.J. Munford, S. Ghouse, J.R.T. Jeffers, Controlling the mechanical behaviour of stochastic lattice structures: The key role of nodal connectivity, Additive Manufacturing 54 (2022).

[240] C. Pauzon, T. Mishurova, M. Fischer, J. Ahlström, T. Fritsch, G. Bruno, E. Hryha, Impact of contour scanning and helium-rich process gas on performances of Alloy 718 lattices produced by laser powder bed fusion, Materials & Design 215 (2022).

[241] K. Karami, A. Blok, L. Weber, S.M. Ahmadi, R. Petrov, K. Nikolic, E.V. Borisov, S. Leeflang, C. Ayas, A.A. Zadpoor, M. Mehdipour, E. Reinton, V.A. Popovich, Continuous and pulsed selective laser melting of Ti6Al4V lattice structures: Effect of post-processing on microstructural anisotropy and fatigue behaviour, Additive Manufacturing 36 (2020).

[242] A.E.M. E. Onal, M.A. Leeflang, A. Molotnikov, A.A. Zadpoor, Novel microstructural features of selective laser melted lattice struts fabricated with single point exposure scanning, Additive Manufacturing 29 (2019).

[243] F.H. Boi Q, Shi YS, Wei QS, RETRACTED ARTICLE: Comparison of two scan strategies applied to the selective laser melting. , ICCASM 2010 - 2010 International Conference on Computer Application and System Modeling, Proceedings, 2010, pp. V5685–V5689.

[244] P. Köhnen, M. Létang, M. Voshage, J.H. Schleifenbaum, C. Haase, Understanding the process-microstructure correlations for tailoring the mechanical properties of L-PBF produced austenitic advanced high strength steel, Additive Manufacturing 30 (2019).

[245] Y.M. Arisoy, L.E. Criales, T. Ozel, B. Lane, S. Moylan, A. Donmez, Influence of scan strategy and process parameters on microstructure and its optimization in additively manufactured nickel alloy 625 via laser powder bed fusion, Int J Adv Manuf Technol 90(5-8) (2017).

[246] B. AlMangour, D. Grzesiak, J.-M. Yang, Scanning strategies for texture and anisotropy tailoring during selective laser melting of TiC/316L stainless steel nanocomposites, Journal of Alloys and Compounds 728 (2017) 424-435.

[247] P. Promoppatum, S.-C. Yao, Influence of scanning length and energy input on residual stress reduction in metal additive manufacturing: Numerical and experimental studies, Journal of Manufacturing Processes 49 (2020) 247-259.

[248] C.Y. Liu, J.D. Tong, M.G. Jiang, Z.W. Chen, G. Xu, H.B. Liao, P. Wang, X.Y. Wang, M. Xu, C.S. Lao, Effect of scanning strategy on microstructure and mechanical properties of selective laser melted reduced activation ferritic/martensitic steel, Materials Science and Engineering: A 766 (2019).

[249] P. Wang, F. Yang, J. Zhao, Compression Behaviors and Mechanical Properties of Modified Face-Centered Cubic Lattice Structures under Quasi-Static and High-Speed Loading, Materials (Basel) 15(5) (2022).

[250] X. Cao, S. Duan, J. Liang, W. Wen, D. Fang, Mechanical properties of an improved 3D-printed rhombic dodecahedron stainless steel lattice structure of variable cross section, International Journal of Mechanical Sciences 145 (2018) 53-63.

[251] B. Van Hooreweder, Y. Apers, K. Lietaert, J.P. Kruth, Improving the fatigue performance of porous metallic biomaterials produced by Selective Laser Melting, Acta Biomater 47 (2017) 193-202.

[252] M.-W. Wu, J.-K. Chen, P.-H. Chiang, P.-M. Chang, M.-K. Tsai, Compression Property, Deformation Behavior, and Fracture Mechanism of Additive-Manufactured Ti-6Al-4V Cellular Solid with a New Cuboctahedron Structure, Metallurgical and Materials Transactions A 51(12) (2020) 6517-6527.

[253] L. Wan, Z. Xia, Y. Song, X. Zhang, F. Liu, G. Fu, S. Shi, Parameter optimization of selective laser melting fabricated titanium alloy using skin-core and triple contour scanning strategy, Journal of Laser Applications 32(4) (2020).

[254] S. Keaveney, A. Shmeliov, V. Nicolosi, D.P. Dowling, Investigation of process by-products during the Selective Laser Melting of Ti6AL4V powder, Additive Manufacturing 36 (2020).

[255] P.L.C. Renishaw, InfiniAM spectral-energy input and melt pool emissions monitoring for AM systems, Data Sheet., 2018.

[256] B. Feng, C. Wang, Q. Zhang, Y. Ren, L. Cui, Q. Yang, S. Hao, Effect of laser hatch spacing on the pore defects, phase transformation and properties of selective laser melting fabricated NiTi shape memory alloys, Materials Science and Engineering: A 840 (2022).

[257] Y. Lu, S. Wu, Y. Gan, T. Huang, C. Yang, L. Junjie, J. Lin, Study on the microstructure, mechanical property and residual stress of SLM Inconel-718 alloy manufactured by differing island scanning strategy, Optics & Laser Technology 75 (2015) 197-206.

[258] J.J. Babu, M. Mehrpouya, T.C. Pijper, G. Willemsen, T. Vaneker, An Experimental Study of Downfacing Surfaces in Selective Laser Melting, Advanced Engineering Materials 24(8) (2022).

[259] S. Ghouse, S. Babu, R.J. Van Arkel, K. Nai, P.A. Hooper, J.R.T. Jeffers, The influence of laser parameters and scanning strategies on the mechanical properties of a stochastic porous material, Materials & Design 131 (2017) 498-508.

[260] W. Liu, C. Chen, S. Shuai, R. Zhao, L. Liu, X. Wang, T. Hu, W. Xuan, C. Li, J. Yu, J. Wang, Z. Ren, Study of pore defect and mechanical properties in selective laser melted Ti6Al4V alloy based on X-ray computed tomography, Materials Science and Engineering: A 797 (2020).

[261] C. Li, J.F. Liu, X.Y. Fang, Y.B. Guo, Efficient predictive model of part distortion and residual stress in selective laser melting, Additive Manufacturing 17 (2017) 157-168.

[262] L. Riva, P.S. Ginestra, E. Ceretti, Mechanical characterization and properties of laser-based powder bed–fused lattice structures: a review, The International Journal of Advanced Manufacturing Technology 113(3-4) (2021) 649-671.

[263] M. Silva, E.F. Shepherd, W.O. Jackson, F.J. Dorey, T.P. Schmalzried, Average patient walking activity approaches 2 million cycles per year: pedometers under-record walking activity, J Arthroplasty 17(6) (2002) 693-7.

[264] H. Huang, L. Wang, Y. Fan, Metallic meta-biomaterials: A critical review of fatigue behaviors, Journal of Science: Advanced Materials and Devices 8(3) (2023).

[265] L. Bai, J. Zhang, Y. Xiong, X. Chen, Y. Sun, C. Gong, H. Pu, X. Wu, J. Luo, Influence of unit cell pose on the mechanical properties of Ti6Al4V lattice structures manufactured by selective laser melting, Additive Manufacturing 34 (2020).

[266] A. Pérez-Sánchez, A. Yánez, A. Cuadrado, O. Martel, N. Nuño, Fatigue behaviour and equivalent diameter of single Ti-6Al-4V struts fabricated by Electron Bean Melting orientated to porous lattice structures, Materials & Design 155 (2018) 106-115.

[267] M. Dallago, S. Raghavendra, V. Luchin, G. Zappini, D. Pasini, M. Benedetti, The role of node fillet, unit-cell size and strut orientation on the fatigue strength of Ti-6Al-4V lattice materials additively manufactured via laser powder bed fusion, International Journal of Fatigue 142 (2021).

[268] V. Weißmann, R. Bader, H. Hansmann, N. Laufer, Influence of the structural orientation on the mechanical properties of selective laser melted Ti6Al4V open-porous scaffolds, Materials & Design 95 (2016) 188-197.

[269] A. Cuadrado, A. Yánez, O. Martel, S. Deviaene, D. Monopoli, Influence of load orientation and of types of loads on the mechanical properties of porous Ti6Al4V biomaterials, Materials & Design 135 (2017) 309-318.

[270] A. Lerebours, P. Vigneron, S. Bouvier, A. Rassineux, M. Bigerelle, C. Egles, Additive manufacturing process creates local surface roughness modifications leading to variation in cell adhesion on multifaceted TiAl6V4 samples, Bioprinting 16 (2019).

[271] L. Yang, C. Yan, W. Cao, Z. Liu, B. Song, S. Wen, C. Zhang, Y. Shi, S. Yang, Compression–compression fatigue behaviour of gyroid-type triply periodic minimal surface porous structures fabricated by selective laser melting, Acta Materialia 181 (2019) 49-66.

[272] K. Man, H. Joukhdar, X.D. Manz, M.Y. Brunet, L.H. Jiang, J. Rnjak-Kovacina, X.B. Yang, Bone tissue engineering using 3D silk scaffolds and human dental pulp stromal cells epigenetic reprogrammed with the selective histone deacetylase inhibitor MI192, Cell Tissue Res 388(3) (2022) 565-581.

[273] K. Man, N. Mekhileri, K. Lim, L.H. Jiang, T. Woodfield, X.B. Yang, MI192 induced epigenetic reprogramming enhances the therapeutic efficacy of human bone marrows stromal cells for bone regeneration, Bone (2021) 116138.

[274] K. Man, I.A. Barroso, M.Y. Brunet, B. Peacock, A.S. Federici, D.A. Hoey, S.C. Cox, Controlled Release of Epigenetically-Enhanced Extracellular Vesicles from a GelMA/Nanoclay Composite Hydrogel to Promote Bone Repair, Int J Mol Sci 23(2) (2022).

[275] K. Man, M.Y. Brunet, R. Lees, B. Peacock, S.C. Cox, Epigenetic Reprogramming via Synergistic Hypomethylation and Hypoxia Enhances the Therapeutic Efficacy of Mesenchymal Stem Cell Extracellular Vesicles for Bone Repair, Int J Mol Sci 24(8) (2023).

[276] F. Cantaboni, D. Battini, K.Z. Hauber, P.S. Ginestra, M. Tocci, A. Avanzini, E. Ceretti, A. Pola, Mechanical and microstructural characterization of Ti6Al4V lattice structures with and without solid shell manufactured via electron beam powder bed fusion, The International Journal of Advanced Manufacturing Technology 131(3-4) (2024) 1289-1301.

[277] S. Alipour, S. Nour, S.M. Attari, M. Mohajeri, S. Kianersi, F. Taromian, M. Khalkhali, G.E. Aninwene, 2nd, L. Tayebi, A review on in vitro/in vivo response of additively manufactured Ti-6Al-4V alloy, J Mater Chem B 10(46) (2022) 9479-9534.

[278] A. Cutolo, B. Engelen, W. Desmet, B. Van Hooreweder, Mechanical properties of diamond lattice Ti-6Al-4V structures produced by laser powder bed fusion: On the effect of the load direction, J Mech Behav Biomed Mater 104 (2020) 103656.

[279] U. Hossain, S. Ghouse, K. Nai, J.R.T. Jeffers, Mechanical and morphological properties of additively manufactured SS316L and Ti6Al4V micro-struts as a function of build angle, Addit Manuf 46 (2021) None.

[280] G. Kang, Ratchetting: Recent progresses in phenomenon observation, constitutive modeling and application, International Journal of Fatigue 30(8) (2008) 1448-1472.

[281] R. Molaei, A. Fatemi, N. Sanaei, J. Pegues, N. Shamsaei, S. Shao, P. Li, D.H. Warner, N. Phan, Fatigue of additive manufactured Ti-6Al-4V, Part II: The relationship

between microstructure, material cyclic properties, and component performance, International Journal of Fatigue 132 (2020).

[282] H. Mughrabi, Dislocation wall and cell structures and long-range internal stresses in deformed metal crystals, Acta Metallurgica 31(9) (1983) 1367-1379.

[283] M.D. Sangid, T. Ezaz, H. Sehitoglu, I.M. Robertson, Energy of slip transmission and nucleation at grain boundaries, Acta Materialia 59(1) (2011) 283-296.

[284] S.J. Li, L.E. Murr, X.Y. Cheng, Z.B. Zhang, Y.L. Hao, R. Yang, F. Medina, R.B. Wicker, Compression fatigue behavior of Ti–6Al–4V mesh arrays fabricated by electron beam melting, Acta Materialia 60(3) (2012) 793-802.

[285] C. Chen, Y. Hao, X. Bai, J. Ni, S.-M. Chung, F. Liu, I.-S. Lee, 3D printed porous Ti6Al4V cage: Effects of additive angle on surface properties and biocompatibility; bone ingrowth in Beagle tibia model, Materials & Design 175 (2019).

APPENDIX A

MATLAB PROGRAMMING

A.1 Whole-profile R_a calculation via image analysis

```
function s_profile = CT_Ra(file_prefix, s_layer, e_layer, threshold,
m_angle)
%Function to measure surface profile of individual lattice struts from
%reconstructed CT data (*.bmp)

%File prefix = filename before the 4 digit slice number
%s_layer/e_layer = start and end layer numbers
%threshold = greyscale threshold value (70?)

%%
%Use moving average to find strut centre in each image

%set moving avergae (+-) range
a_range = 20;

%define array for X/Y strut centres
s_cen = zeros(e_layer - s_layer + 1, 2);

%Define array for surface profile
s_profile = zeros(e_layer - s_layer + 1,1);

%calculate X/Y strut centre for each slice individually
for i = 1 : (e_layer - s_layer + 1)
    l_name = num2str(s_layer + i -1);
    while (length(l_name) < 4)
        l_name = ['0' l_name];
    end
    f_name = [file_prefix l_name '.bmp'];
    c_image = imread(f_name);
    im_size = size (c_image);
    count = 0;
    x_sum = 0;
    y_sum = 0;
    for j = 1 : im_size(1)
        for k = 1 : im_size(2)
            if (c_image(j,k)>threshold)
                count = count + 1;
```

```
                x_sum = x_sum + j;
                y_sum = y_sum + k;
            end
        end
    end
    s_cen (i,1) = round(x_sum/count);
    s_cen (i,2) = round(y_sum/count);
end

s_cen_av = zeros(e_layer - s_layer + 1, 2);
for i = 1 : (e_layer - s_layer + 1)
    lb = i - a_range;
    ub = i + a_range;
    if (lb < 1)
        lb = 1;
    end
    if (ub > length(s_cen_av))
        ub = length(s_cen_av);
    end
    s_cen_av (i, 1) = round(mean (s_cen (lb:ub, 1)));
    s_cen_av (i, 2) = round(mean (s_cen (lb:ub, 2)));
end

%%
% Measure distance in pixels from strut centre to outermost solid
along a
% specified angle

x_step = sind(m_angle);
y_step = cosd(m_angle);
if (abs(x_step)>abs(y_step))
    y_step = y_step/abs(x_step);
    if x_step > 0
        x_step = 1;
    else
        x_step = -1;
    end
else
     x_step = x_step/abs(y_step);
    if y_step > 0
        y_step = 1;
    else
        y_step = -1;
    end
end

%For each image, look along vector for last threshold pixel
for i = 1 : (e_layer - s_layer + 1)
    l_name = num2str(s_layer + i -1);
    while (length(l_name) < 4)
        l_name = ['0' l_name];
    end
    f_name = [file_prefix l_name '.bmp'];
    c_image = imread(f_name);
    im_size = size (c_image);
    inbounds = true;
    count = 0;
```

```
    c_x = 0;
    c_y = 0;
    t_x = 0;
    t_y = 0;
    while (inbounds)
        c_x = s_cen_av (i,1) + round(count*x_step);
        c_y = s_cen_av (i,2) - round(count*y_step);
        if ((c_x<1)||(c_y<1)||(c_x>im_size(1))||(c_y>im_size(2)))
            inbounds = false;
        else
            if (c_image (c_x, c_y) > threshold)
                t_x = c_x;
                t_y = c_y;
            end
            %Left in to show the direction of profile
            c_image (c_x, c_y) = 200;
            count = count + 1;
        end
    end
    s_profile (i) = sqrt((s_cen_av (i,1)-t_x)^2 + (s_cen_av (i,2)-
t_y)^2);

end

 s_profile (i) = sqrt((s_cen_av (i,1)-t_x)^2 + (s_cen_av (i,2)-
t_y)^2);
    filtered = rmoutliers (s_profile) %Filter outliers
    count = size(filtered);
    number = count(1);
    pixel_size = 3.78992;
    p_m = filtered(:, 1) * pixel_size; %profile in micron
    m_line = mean(p_m); %find mean value of the whole profile
    Ra = sum(abs(p_m - m_line))/number; %Ra calculation
end

%Displays final slice showing direction profile taken!
figure
imshow(c_image)

%simple plot
figure
plot (p_m);
yline(m_line);
end
```

A.2 Lattice design parameter map

```
load('data_angles.mat')

x=[0:5:180];

alpha=atan(1/sqrt(2));
gamma=abs(atan2(sin(alpha)*sin(x*pi/180+pi/2),sqrt(cos(alpha)^2+(sin(a
lpha)*cos(x*pi/180+pi/2)).^2))*180/pi);
```

```
for i=1:length(x)
    minq(i)=sqrt((angle2T(i,1)-45)^2+(angle2T(i,2)-45)^2);
    minq2(i)=sqrt((angle2T(i,1)-45)^2+(angle2T(i,2)-45)^2+2*(gamma(i)-
45)^2);
end

plot(x,angle2T(:,1),'r')
hold on
plot(x,angle2T(:,2),'b')
plot(x,minq,'k')
%plot(x,gamma,'m');

xlabel('Angle of rotation (°)')
ylabel('Strut angle (°)')
legend('\alpha','\alpha"','\surd(\alpha-45°)^2+(\alpha"-45°)^2')

figure
plot(x,angle2T(:,1),'r')
hold on
plot(x,angle2T(:,2),'b')
plot(x,gamma,'m');
plot(x,minq2,'k')
topcolor = [1 0 0];    % red
bottomcolor = [0 1 0]; % green
p = addgradient(gca, topcolor,bottomcolor);  % Red-green gradient to
bottom plot
set(p,'FaceAlpha',.3)  % Make transparent
xlabel('Angle of rotation (°)')
ylabel('Strut angle (°)')
%legend('\alpha','\alpha"','\gamma','\surd((\alpha-45°)^2+(\alpha"-
45°)^2+(\gamma-45°)^2)')

L=1:20;
a=sqrt(2)*5;

alphan=atan(L./a)*180/pi;
devalpha=2*abs(alphan-45)

figure
plot(L,alphan,'r');
hold on
plot(L,devalpha,'k')
xlabel('Unit cell height (mm)')
ylabel('Deviation from 45 deg (°)')
%legend('\alpha','2*abs(\alpha-45°)')
topcolor = [1 0 0];    % red
bottomcolor = [0 1 0]; % green
p = addgradient(gca, topcolor,bottomcolor);  % Red-green gradient to
bottom plot
set(p,'FaceAlpha',.3)  % Make transparent
```

A.3 MPR plot

```
function  plot_mp_slice(layer, x, y, x_size, y_size)
%Plot sinlge slice mp data

%%
%Import Data from file
filename = ['Packet data for layer ' num2str(layer) ', laser 4.txt'];
layer_data = Import_mp_data(filename);

%% Remove all but Region of Interest (at the moment simple rectangle)
count = 0;
for i = 1:length(layer_data)
    if (layer_data (i,2) < x)||(layer_data (i,2) >
(x+x_size))||(layer_data (i,3) < y)||(layer_data (i,3) > (y+y_size))
        count = count + 1;
    end
end

roi_data = zeros (length(layer_data)-count,4);
count = 1;

for i = 1:length(layer_data)
    if not((layer_data (i,2) < x)||(layer_data (i,2) >
(x+x_size))||(layer_data (i,3) < y)||(layer_data (i,3) > (y+y_size)))
        roi_data (count,:) = layer_data(i,:);
        count = count + 1;
    end
end
clear layer_data;

%% Plot ROI Data
figure
X = roi_data(:,2);
Y = roi_data(:,3);
Z = roi_data(:,4);
stem3(X, Y, Z, "-k", "MarkerEdgeColor", "none");
hold on;
scatter3(X, Y, Z,150, Z,  "filled");
colorbar
hold on;
axis tight
title('MP Data')
hold off;
```

A.4 Fatigue results

A.4.1 Cycle to strain

```
close all
clear
clc

data3 = importdata('control_1_2.76kn.txt');
strain3 = abs(data3.data(:,2))/20;
cycle3 = data3.data(:,4);
groups3 = findgroups(cycle3);  % Create groups based on X values
strain3_max = splitapply(@max, strain3, groups3);  % Calculate maximum
Y for each group
strain3_min = splitapply(@min, strain3, groups3);  % Calculate minimum
Y for each group
difference3 = strain3_max - strain3_min;  % Calculate the difference
data4 = importdata('control_1_3.68kn.txt');
strain4 = abs(data4.data(:,2))/20;
cycle4 = data4.data(:,4);
groups4 = findgroups(cycle4);  % Create groups based on X values
strain4_max = splitapply(@max, strain4, groups4);  % Calculate maximum
Y for each group
strain4_min = splitapply(@min, strain4, groups4);  % Calculate minimum
Y for each group
difference4 = strain4_max - strain4_min;  % Calculate the difference
data5 = importdata('control_2_4.61kn.txt');
cycle5 = data5.data(:,4);
strain5 = abs(data5.data(:,2))/20;
groups5 = findgroups(cycle5);  % Create groups based on X values
strain5_max = splitapply(@max, strain5, groups5);  % Calculate maximum
Y for each group
strain5_min = splitapply(@min, strain5, groups5);  % Calculate minimum
Y for each group
difference5 = strain5_max - strain5_min;  % Calculate the difference
data6 = importdata('control_1_5.53kn.txt');
cycle6 = data6.data(:,4);
strain6 = abs(data6.data(:,2))/20;
groups6 = findgroups(cycle6);  % Create groups based on X values
strain6_max = splitapply(@max, strain6, groups6);  % Calculate maximum
Y for each group
strain6_min = splitapply(@min, strain6, groups6);  % Calculate minimum
Y for each group
difference6 = strain6_max - strain6_min;  % Calculate the difference
data7 = importdata('control_1_6.45kn.txt');
cycle7 = data7.data(:,4);
strain7 = abs(data7.data(:,2))/20;
groups7 = findgroups(cycle7);  % Create groups based on X values
strain7_max = splitapply(@max, strain7, groups7);  % Calculate maximum
Y for each group
strain7_min = splitapply(@min, strain7, groups7);  % Calculate minimum
Y for each group
difference7 = strain7_max - strain7_min;  % Calculate the difference
```

```
figure

plot(unique(cycle3),difference3)

hold on

plot(unique(cycle4),difference4)

hold on

plot(unique(cycle5),difference5);

hold on

plot(unique(cycle6),difference6)

hold on

plot(unique(cycle7),difference7)
hold off
```

A.4.2 Strain to stress

```
close all
clear
clc

data = importdata('control_1_4.61kn.txt');
strain = abs(data.data(:,2))/20;
stress = abs(data.data(:,3))/176.625;
cycle = data.data(:,4);
s_cycle = find(cycle==203);
s_strain = strain(s_cycle);
s_stress = stress(s_cycle);

figure
plot(s_strain,s_stress)
hold on
s_cycle_2 = find(cycle==503);
s_strain_2 = strain(s_cycle_2);
s_stress_2 = stress(s_cycle_2);
plot(s_strain_2,s_stress_2)
hold on
s_cycle_3 = find(cycle==1013);
s_strain_3 = strain(s_cycle_3);
s_stress_3 = stress(s_cycle_3);
plot(s_strain_3,s_stress_3)
hold on
s_cycle_4 = find(cycle==2498);
s_strain_4 = strain(s_cycle_4);
s_stress_4 = stress(s_cycle_4);
plot(s_strain_4,s_stress_4);
hold on
s_cycle_5 = find(cycle==5003);
```

```
s_strain_5 = strain(s_cycle_5);
s_stress_5 = stress(s_cycle_5);
plot(s_strain_5,s_stress_5);
hold on
s_cycle_6 = find(cycle==7508);
s_strain_6 = strain(s_cycle_6);
s_stress_6 = stress(s_cycle_6);
plot(s_strain_6,s_stress_6);
hold on
s_cycle_7 = find(cycle==10013);
s_strain_7 = strain(s_cycle_7);
s_stress_7 = stress(s_cycle_7);
plot(s_strain_7,s_stress_7);
hold on
s_cycle_8 = find(cycle==12008);
s_strain_8 = strain(s_cycle_8);
s_stress_8 = stress(s_cycle_8);
plot(s_strain_8,s_stress_8);
hold on
s_cycle_9 = find(cycle==13013);
s_strain_9 = strain(s_cycle_9);
s_stress_9 = stress(s_cycle_9);
plot(s_strain_9,s_stress_9)
```

APPENDIX B

RENISHAW 500 OPERATION

B.1 Valiadation between 500M and 500S

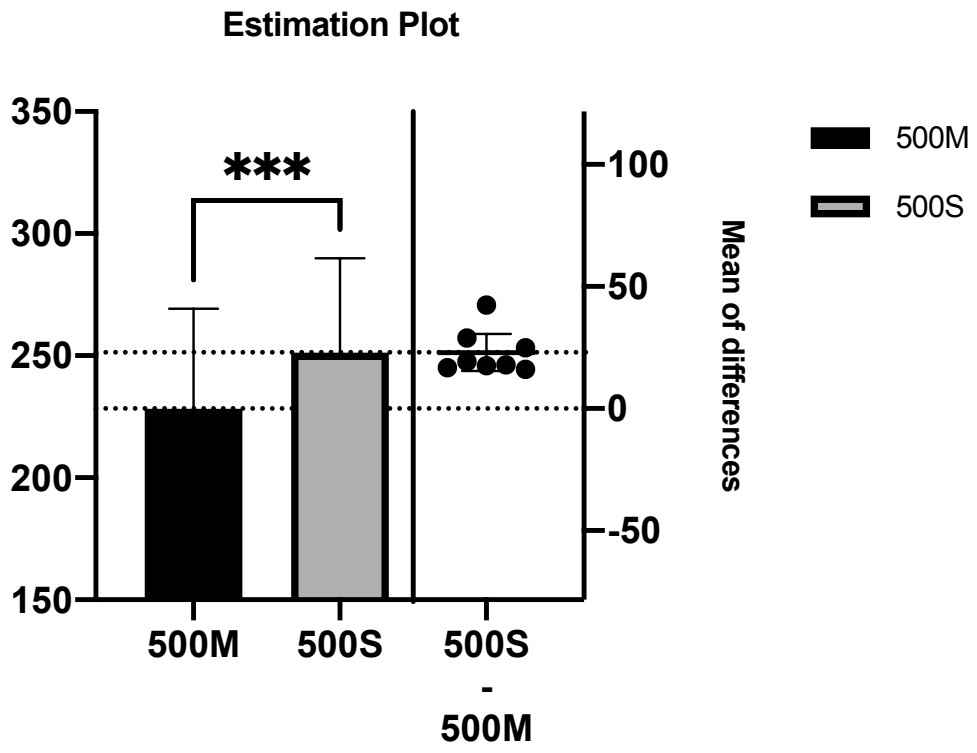

B.2 Parameter setting interface and Build Plate

B.2.1 Parameter setting interface

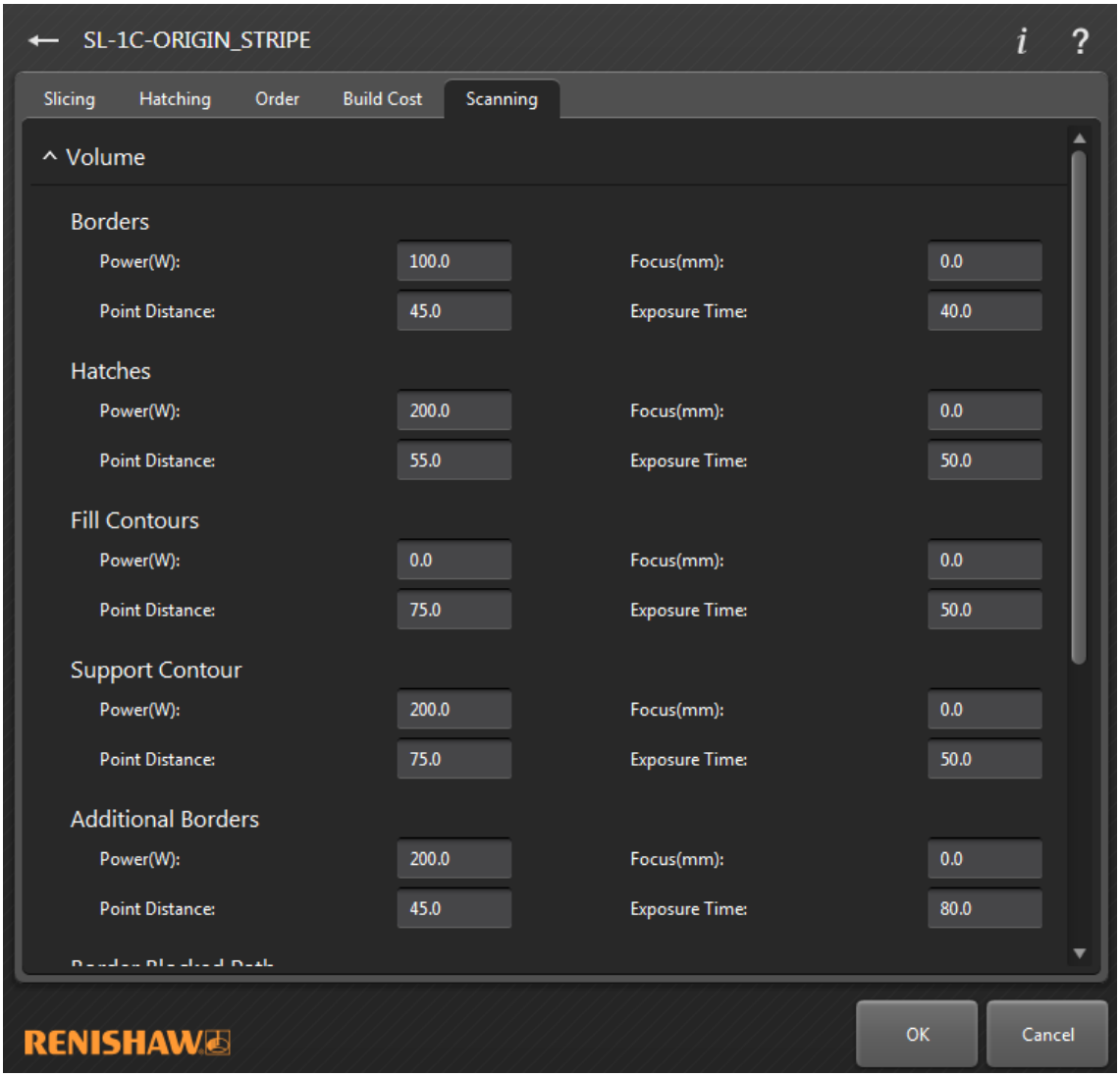

B.2.2 Build Plate gas flow direction and coordinate system

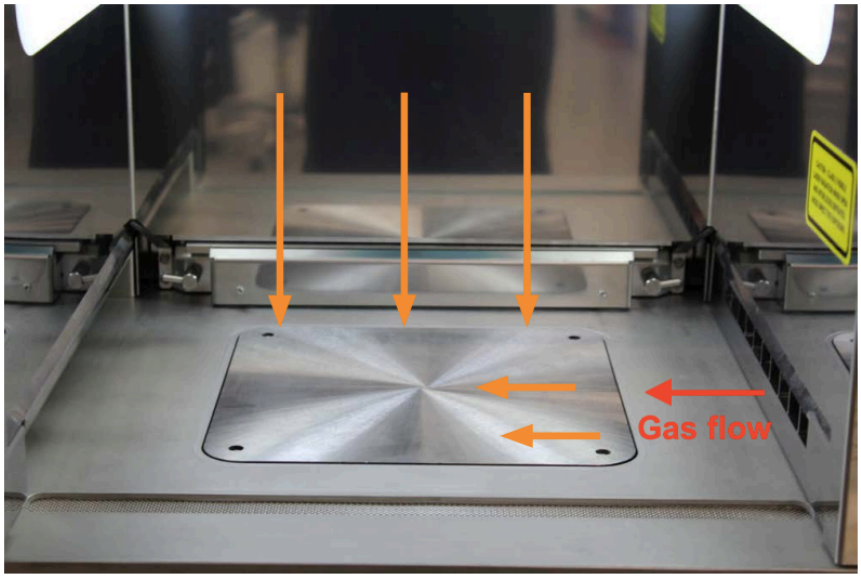

Gas circuit marked as orange arrow, which directing the gas flow across the build plate from right to left. Adapted from Renishaw website -- *RenAM 500 series additive manufacturing system.*

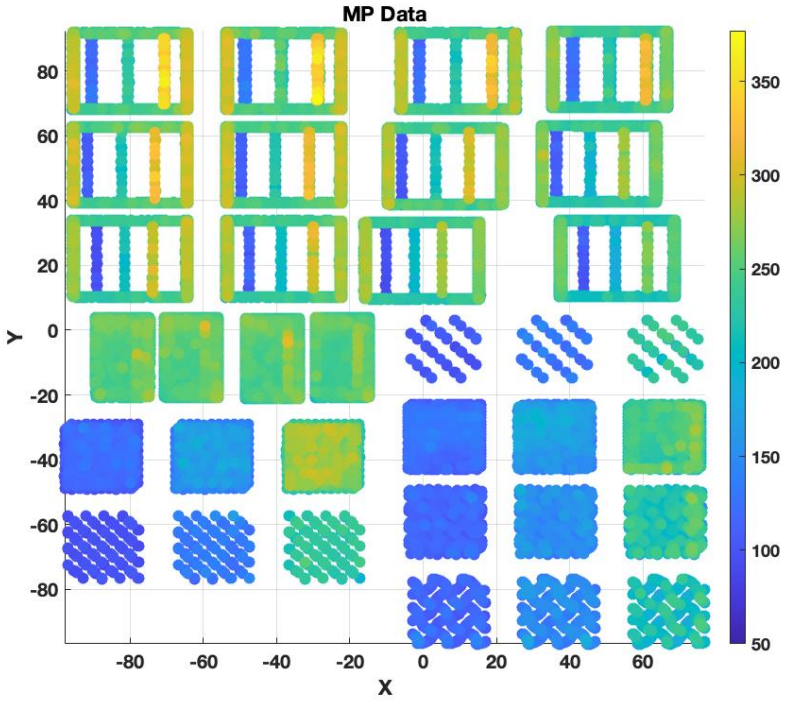

MATLAB processed data showing the full coordinate of build plate adapted for locating the MPR data collected from the RenAM 500 AMPM system. Colours in the coordinate representing MPR in different parts.

B.3 Rotation Strategy

This figure shows the rotation and tilting sequence of the samples, where 1) the SO45 and SOUO45 follows the step one rotating 45˚ across z-axis in the coordinate of build substrate, and then tilt 45˚ along the y-axis; 2) The UO45 lattice was obtained by the default BCC titled solely along y-axis. The marked place represents the front of the build substrate.